5-1978

Neutron Diffraction Analysis of the Structure of Rod Photoreceptor Membranes in intact Retinas

Mark Jay Yeager
Yale University.

NEUTRON DIFFRACTION ANALYSIS OF THE STRUCTURE OF ROD PHOTORECEPTOR MEMBRANES IN INTACT RETINAS

A DISSERTATION

PRESENTED TO THE FACULTY OF THE GRADUATE SCHOOL

OF

YALE UNIVERSITY

IN CANDIDACY FOR THE DEGREE OF

DOCTOR OF PHILOSOPHY

BY

MARK YEAGER

MAY 1978

ABSTRACT

NEUTRON DIFFRACTION ANALYSIS OF THE STRUCTURE OF ROD PHOTORECEPTOR MEMBRANES IN INTACT RETINAS

Mark Yeager

Yale University, 1973

The technique of neutron diffraction is complementary to that of x-ray diffraction because the neutron scattering amplitudes of hydrogen and deuterium are very different. The neutron scattering density of water can be manipulated over a large range by simply changing the D_2O-H_2O content of the Ringer's solution. Consequently, several different images of the membrane can be obtained. Furthermore, the contrast between the protein, lipid, and aqueous components of membrane systems is greater with neutron diffraction than with x-ray diffraction. Isomorphous D_2O-H_2O exchange can also be used to assign phases and place Fourier syntheses on an absolute scale, thereby simplifying the molecular interpretation.

Neutron diffraction data have been collected from samples containing 10 dark-adapted Rana catesbiana bullfrog retinas in 100, 80, 60, 40, and 30% D_2O Ringer's solution using a step-scanning Soller-slit diffractometer. Diffraction was also recorded from retinas equilibrated in D_2O solutions with varying osmolarity. The rotationally symmetric disorientation of the rods was characterized by persistence-with-tilt, slit-height reduction, and rocking-curve experiments. Structure factor amplitudes were obtained using semi-automated curve-fitting procedures, and phases were obtained by interpreting the D_2O-H_2O and osmotic Patterson

maps. In D_2O Ringer's solution the first four structure factors are -353±25, 246±19, 434±13, and 383±19. Neutron scattering density profiles were calculated on an absolute scale to 75 Å resolution using the first four structure factors.

Neutron diffraction experiments on intact retinas confirm by an independent approach the x-ray diffraction studies which suggest that the lipid bilayer is a major structural motif of the rod outer segment disc membrane. Neutron Fourier syntheses in different mixtures of D_2O and H_2O indicate that the intradisc and extradisc spaces are predominantly aqueous, consistent with the increase in the intradisc and extradisc volumes as the Ringer's solution is made more hypotonic. In isotonic Ringer's solution, the thicknesses of the intradisc and extradisc spaces are about 36 Å and 160 Å, respectively, and the center-to-center separation between the 50 Å thick lipid bilayers is 88 Å. The neutron scattering density in the center of the membrane ($0.45 \pm 0.20 \times 10^{-14}$ cm/Å^3) is greater than that of pure hydrocarbon (-0.02×10^{-14} cm/Å^3), indicating that the volume fraction of protein in the membrane interior is 0.23 ± 0.10. Neutron scattering density profiles in D_2O Ringer's solution are strikingly asymmetric with a lower scattering density on the extradisc side of the disc membrane. Models that orient rhodopsin asymmetrically on the cytoplasmic face of the disc membrane extending into the extradisc aqueous space are in close agreement with the observed asymmetry. However, rhodopsin cannot entirely account for the observed asymmetry, suggesting that other hydrogenated material resides in the extradisc region.

ACKNOWLEDGMENTS

Grateful acknowledgment is made to my principal advisors Drs. Lubert Stryer and Benno Schoenborn, as well as Drs. Donald Engelman and Peter Moore, for illuminating discussions and for their encouragement and assistance during the course of this research. I also thank Drs. Richard Henderson, Rich Mathies, Allan Oseroff, Jordan Pober, Bob Renthal, Joel Shaper, Will Veatch and David Wise for their advice and help during this work.

I thank Ms. Helen Saibil, Dr. Marc Chabre, and Dr. David Worcester for communicating their results before publication, and Dr. Allan Oseroff for helpful criticisms of the text of this dissertation. I am indebted to Mr. Gerald Johnson and Mr. Ed Caruso for expert technical assistance and Ms. Sharen Enson for invaluable assistance in data processing and manuscript preparation. I also thank Dr. Joseph Corless and Dr. Paul Liebman for helpful discussions regarding the chemical composition of rod outer segments. I am grateful to the National Eye Institute, the National Science Foundation, the U.S. Atomic Energy Commission, the U.S. Energy Research and Development Administration, and the Medical Scientist Training Program for their support of this work.

I also thank Benno and Kay Schoenborn for their kind hospitality during my experiments at Brookhaven National Laboratory.

Most of all, I wish to express my appreciation to my family and Ms. Bonnie Whitsel for their support and encouragement, especially during the lulls in productivity.

TABLE OF CONTENTS

LIST OF TABLES

LIST OF FIGURES

Figure | Page

CHAPTER I

INTRODUCTION

Visual excitation originates with the absorption of light by rhodopsin, the photoreceptor protein in the rod cells of the retina. Rhodopsin is an intrinsic membrane protein composed of an apoprotein, opsin, and an 11-*cis* retinal chromophore. The absorption of a single photon can excite a rod cell (Hecht, Shlaer and Pirenne, 1942). Wald (1968) showed that the photoisomerization of 11-*cis* retinal to the all-*trans* configuration is a critical early event in visual excitation. However, the subsequent cascade of structural events leading to the hyperpolarization of the plasma membrane of the rod cell (Tomita, 1970; Hagins, 1972) is not yet known. Understanding the molecular basis of visual excitation requires a detailed knowledge of the architecture of rod photoreceptor membranes and of rhodopsin. More generally, structural studies on rod cell membranes may help elucidate some of the principles underlying the organization of other biological membranes.

Electron and light microscopy (Sidman, 1957; Nilsson, 1965; Dowling, 1967; Bownds and Brodie, 1975) have shown that frog rod outer segments are cylindrical with a diameter of $\sim 6\mu$ and a length of $\sim 50\mu$ (Figure 1). Rod outer segments are aligned approximately parallel to one another in the retina and contain a periodic stack of about 1,500 discs. Along the long axis of the rod, the 300 Å repeating unit contains two densely staining disc membranes with a narrow intradisc space and a wider extradisc space (Figure 2). The periodic stacking of the disc membranes and the parallel alignment of the rod outer segments in the retina makes the

Figure 1. Scanning electron micrograph of rod photoreceptor cells in the retina of the frog Rana catesbiana. (From Bownds and Brodie, 1975).)

Figure 2. Electron micrograph of a rod outer segment, showing the periodically stacked disc membranes. (From Dowling, 1967).

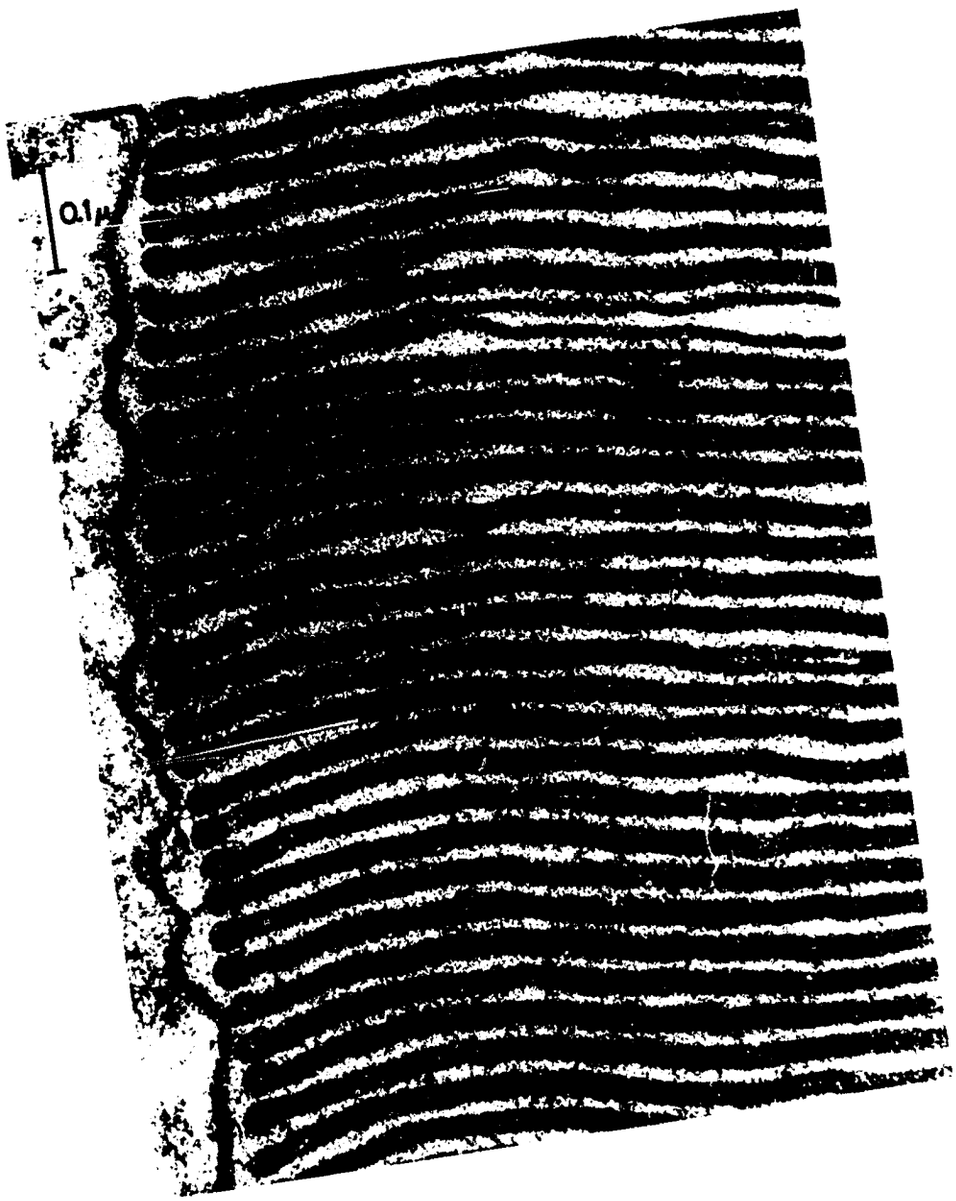

system act like a one dimensional crystal, allowing investigation of rod structure by diffraction methods in intact retinas. However, because the rods are neither perfectly parallel nor the discs stacked with perfect regularity, the limiting resolution of such a diffraction study is about 30 Å. Although it is not feasible to determine the structure to atomic resolution, information can be obtained about the distribution of molecular components - protein, lipid, and water - along the long axis of the rod outer segment.

X-ray diffraction analysis has provided the most compelling evidence that a major portion of the lipids in the disc membrane are arranged in a bilayer (Blaurock and Wilkins, 1969; Gras and Worthington, 1969; Corless, 1972; Blaurock and Wilkins, 1972; Chabre, 1975). However, the location of rhodopsin in the membrane and the structural changes that occur after light absorption have not been clearly defined. Although the diffraction patterns recorded at several laboratories are quite similar, the interpretations have been strikingly divergent: models have been proposed that localize rhodopsin on the intradisc side (Worthington, 1973; Worthington, 1974), on both sides (Blaurock, 1972; Wilkins, 1972; Vanderkooi and Sundaralingam, 1970), and partly on the extradisc side of the disc membrane (Corless, 1972; Chabre, 1975). In fact, a pure lipid bilayer model with no protein (Figure 3b) is quite similar to the experimental x-ray scattering density profile of Blaurock and Wilkins (1972) (continuous curve in Figure 3a). There are no landmarks in their experimental electron density profile that can be readily attributed to protein.

This dissertation reports the first use of neutron scattering to investigate the structure of rod photoreceptor membranes in intact retinas. The neutron diffraction pattern in D_2O Ringer's solution extends to

Figure 3. Electron density profiles of rod outer segment disc membranes at 30 Å resolution. a. (————) Experimental Fourier synthesis calculated from the data of Blaurock and Wilkins (1972). The experimental structure factors for orders 1 to 10 are 56.8, -9.80, 34.7, 59.3, -47.0, -143, -143, -69.1, 69.1, and 49.5, respectively (Webb, 1972). (••••••••••) Experimental Fourier synthesis calculated with a phase of -1 for the first reflection. b. Fourier synthesis calculated from a pure lipid bilayer model of the disc membrane. The calculated structure factors for orders 0 to 10 are 2848, 38.8, -7.96, 18.7, 64.3, 13.0, -116, -169, -74.5, 54.9, and 81.0, respectively. The Fourier syntheses have been scaled to the same vertical peak-to-trough distance. The bilayer model was identical to that shown in Figure 5 except that 3 Å troughs with x-ray scattering density of 4.62×10^{-14} $cm/Å^3$ were placed in the center of the lipid bilayers. These troughs correspond to localized terminal methyl groups of the hydrocarbon chains. The model in Figure 5 with a constant x-ray scattering density in the lipid hydrocarbon region also resembles the experimental Fourier synthesis (continuous curve in a.) quite closely. However, the phase of reflection 3 is negative for the model in Figure 5 and the amplitudes of orders 2 and 3 are reversed, compared with the experimental amplitudes. When the model Fourier syntheses are scaled to the same peak-to-trough distance, the effect of the low density troughs is to shift the scattering density of the aqeous regions to a higher level relative to the lipid hydrocarbon regions.

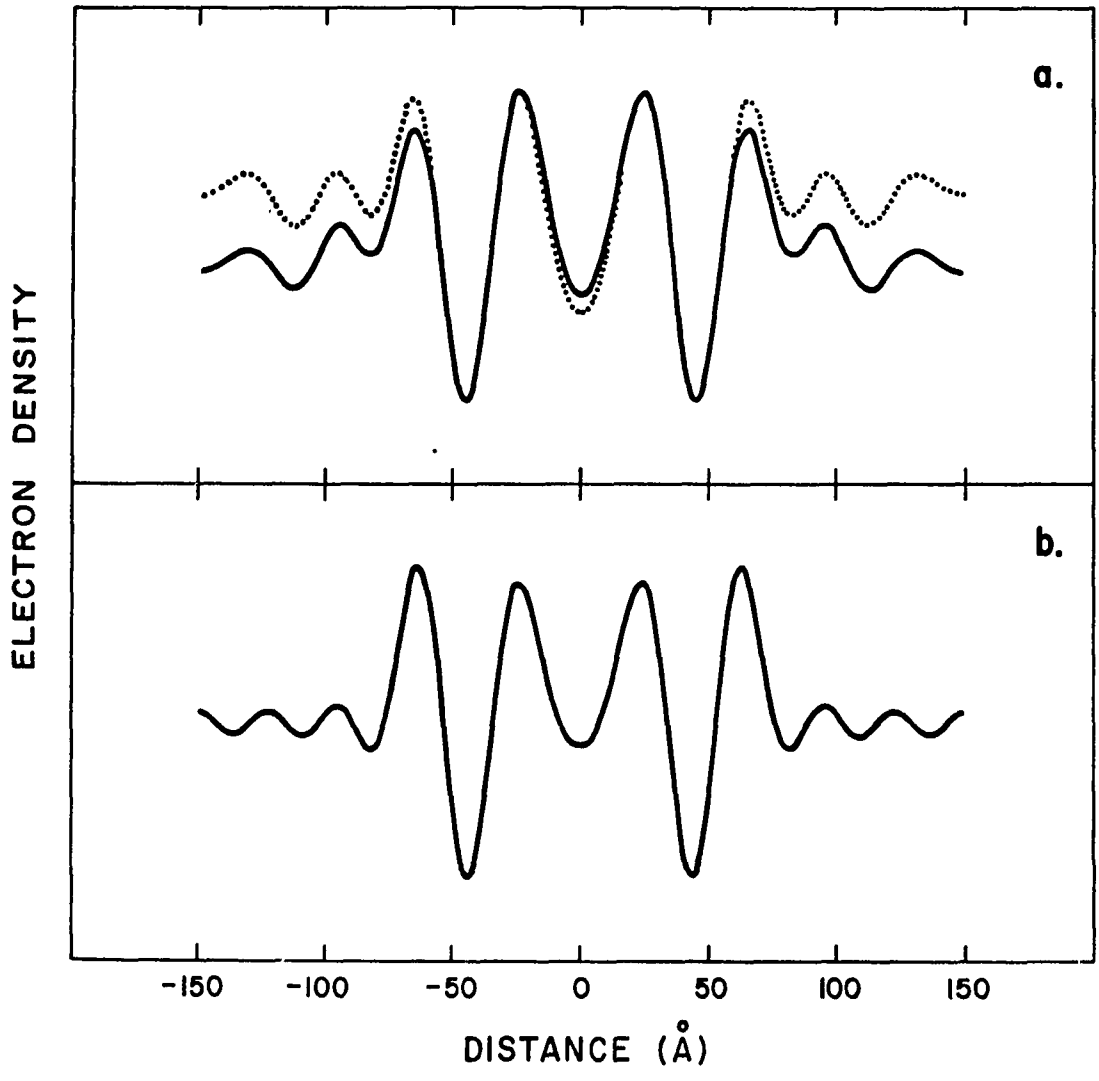

33 Å resolution. Phases for the first 4 reflections were determined by D_2O-H_2O exchange and by osmotic shrinking and swelling. It is important to stress that the analysis of the neutron diffraction data is entirely independent of the x-ray studies. Although the resolution of the neutron Fourier syntheses is only 75 Å, their high contrast allows conclusions to be drawn that complement and extend the x-ray results. Models having a substantial amount of rhodopsin on the cytoplasmic face of the disc membrane protruding into the extradisc aqueous space are most compatible with the neutron Fourier syntheses. The neutron results also suggest that the extradisc aqueous space contains an appreciable amount of hydrogenated material. The existence of such material may account for the stabilization of the regular, parallel arrangements of discs in the outer segment. Summaries and an abstract of this work have been published (Yeager, Schoenborn, Engelman, Moore, and Stryer, 1974; Yeager, 1975a, b).

CHAPTER II

STRATEGY FOR NEUTRON DIFFRACTION ANALYSIS OF BIOLOGICAL MEMBRANES AND COMPARISON WITH X-RAY DIFFRACTION

Neutron diffraction is a powerful technique for investigating biological membranes (for a review, see Schoenborn, 1976), as exemplified by neutron diffraction studies of myelin (Kirschner and Caspar, 1972; Kirschner, 1974; Kirschner, Casper, Schoenborn and Nunes, 1976) and of model membrane systems (Zaccai, Blasie and Schoenborn, 1975; Worcester and Franks, 1976; Schoenborn, 1976; Worcester, 1976). The unique advantage of neutron diffraction for the elucidation of biological structure is the large difference in scattering length between hydrogen (-3.72×10^{-13}cm) and deuterium (6.67×10^{-13}cm) (Bacon, 1962). This difference can be exploited to enhance the contrast between different constituents of biological membrane systems. The absolute scattering densities of membrane components in x-ray and neutron diffraction experiments are compared in Figure 4. The scattering density, ρ, of a molecular component is given by

$$\rho = \frac{\sum_{i=1}^{n} a_i b_i}{V} \qquad (1)$$

where a_i is the number of ith nuclei in the component, b_i is the scattering length of the ith nucleus and V is the molecular volume (Schoenborn

and Nunes, 1972). The neutron scattering densities of H_2O and D_2O are $-.561 \times 10^{-14}$ and 6.35×10^{-14} cm/$\AA^3$, respectively. The neutron scattering density of water, ρ_w, is therefore given by

$$\rho_w = -.561 \times 10^{-14} + 6.91 \times 10^{-14} \beta \qquad (2)$$

where β is the volume fraction of D_2O. The neutron scattering density of rhodopsin, ρ_p, will depend on the D_2O concentration since those hydrogens not covalently bonded to carbon are potentially exchangeable.

$$\rho_p = 1.9 \times 10^{-14} + 1.27 \times 10^{-14} \beta\gamma \qquad (3)$$

where γ is the fraction of potentially exchangeable hydrogens. Tritium-exchange measurements (Downer and Englander, 1975) have shown that γ is greater than 0.5.

The overall enhancement in contrast, indicated by the length of the vertical bars in Figure 4, clearly favors the neutron diffraction experiment conducted in heavy water, D_2O. Of particular value is the enhanced contrast between the membrane molecular components obtained by using neutron diffraction rather than x-ray diffraction. For instance, the contrast between D_2O and lipid hydrocarbon in neutron diffraction is 8-fold greater than the water-hydrocarbon contrast with x-rays. Another powerful technique is contrast-matching of particular molecular species. Since the densities of the membrane components are intermediate between those of H_2O and D_2O, the appropriate D_2O concentration can be chosen to match the scattering density of the solvent to that of one of the components. For example, the volume percent D_2O at which the neutron scattering density of water matches the scattering density of rhodopsin can be found by setting ρ_w equal to ρ_p and solving for β. The calculated contrast-match point of rhodopsin is 43.5% D_2O assuming $\gamma = 1$, so that the scattering from that

Figure 4. Comparison of absolute scattering amplitude densities and the contrast between membrane molecular components with x-ray and with neutron diffraction. The neutron scattering density of the lipid headgroup and that of rhodopsin are greater in D_2O than in H_2O (upper and lower bound of each range, respectively) because of exchangeability of hydrogens not covalently bonded to carbon. Electron densities were converted to scattering amplitude densities by using the scattering amplitude per electron, 0.28×10^{-12} cm. Neutron scattering densities were calculated from equation (1) using the scattering lengths of -3.74×10^{-13}, 6.67×10^{-13}, 6.65×10^{-13}, 9.40×10^{-13}, 5.80×10^{-13}, and 5.10×10^{-13} cm for H,D,C,N,O, and P, respectively (Bacon, 1962; Schoenborn and Nunes, 1972). The atomic composition for the average rod outer segment lipid was calculated from published chemical analyses (Daemen, 1973), and molecular volumes were calculated from Traube volumes of the atomic nuclei (Traube, 1899). The molecular volume of rhodopsin (47,000 $\mathring{A}^3$) was calculated from its amino acid composition (Robinson, Gordon-Walker, and Bownds, 1972; Heitzmann, 1972) and the partial specific volumes of amino acid residues (Cohn and Edsall, 1943).

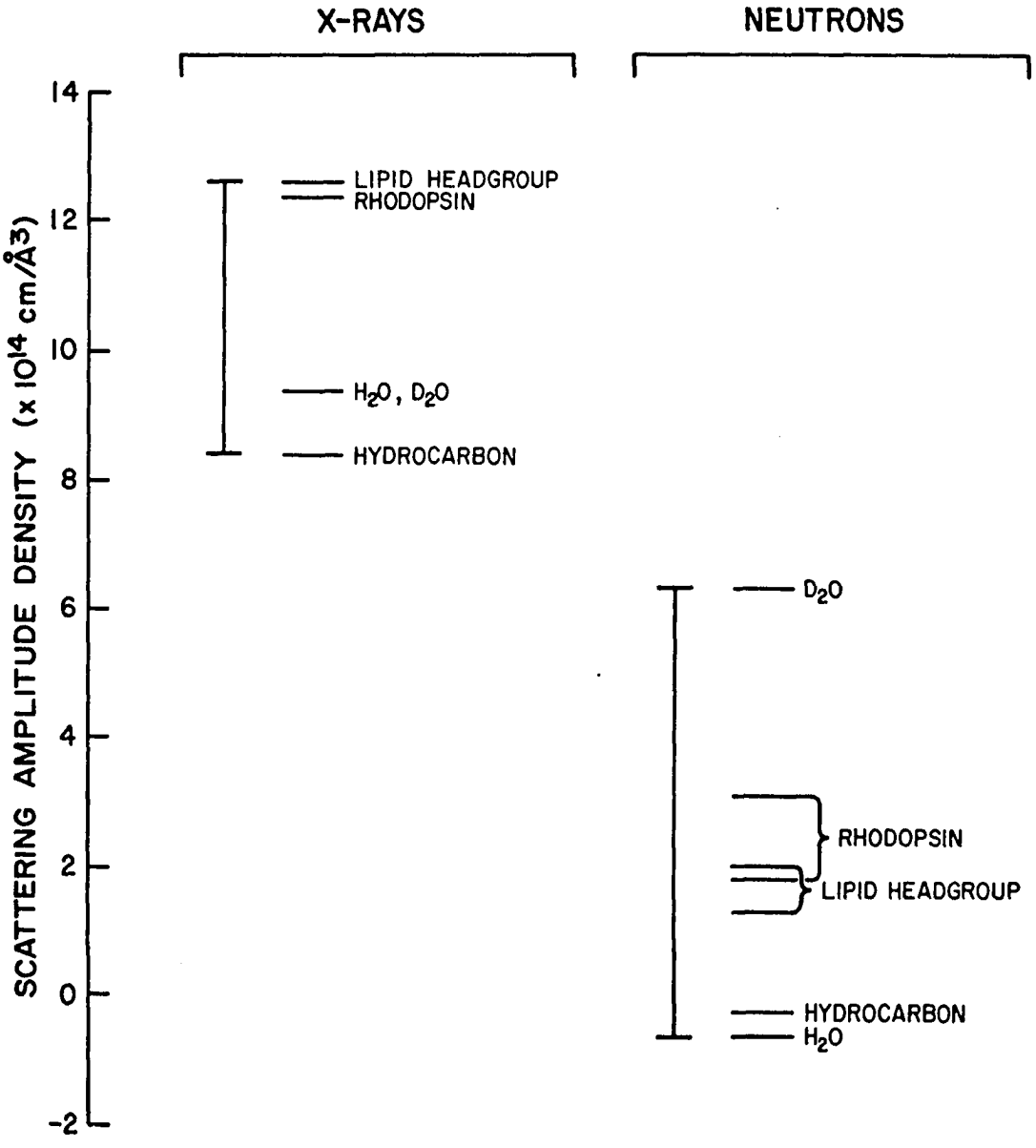

9).

part of rhodospin residing in water vanishes at this D_2O concentration.

An alternative way of conveying the essence of the neutron diffraction method is depicted in Figure 5, where a lipid bilayer model for the disc membrane is shown schematically, followed by the electron density image and the neutron scattering density profiles of this model in D_2O and H_2O. Since the geometrical nature of both x-ray and coherent neutron scattering is the same (Bacon, 1962; Schoenborn and Nunes, 1972; James, 1965), the structure factors for the x-ray and neutron scattering density profiles can be calculated by Fourier transformation of their respective centrosymmetric step function models:

$$\vec{F}(h) = 2\int_0^{\frac{d}{2}} \rho(x)\cos\left(\frac{2\pi hx}{d}\right)dx \qquad (4)$$

where $\vec{F}(h)$ is the structure factor for order h; $\rho(x)$ is the scattering density at a real space distance x; and d is the unit-cell repeat spacing (James, 1965; Levine, 1973). The profiles in Figure 5 represent the images of the membrane at 30 Å resolution calculated by including the first eleven structure factors from equation 4 in the Fourier transformation

$$\rho(x) = \frac{F(0)}{d} + \frac{2}{d}\sum_{h=1}^{n} \vec{F}(h)\cos\left(\frac{2\pi hx}{d}\right) \qquad (5)$$

where n = 10 and d = 300 Å.

In the x-ray diffraction profile, the greatest contrast arises between the electron-dense phosphate headgroups and the electron-deficient hydrocarbon domains of the lipid bilayers. Since the electron density of rhodopsin is almost the same as that of the lipid headgroups, rhodopsin cannot be detected in a low resolution x-ray map if the molecule resides in this region. This problem, compounded by the low contrast

Figure 5. X-ray and neutron scattering density profiles for a lipid bilayer model of the disc membrane. Step function profiles for the one-dimensional projections of the lipid bilayer model were obtained from the scattering densities in Figure 4. The images of the membrane with x-rays (• • • • •) and neutrons are quite different. The neutron scattering density profile in D_2O (———) is quite different from that in H_2O (------). Thus, several images of the membrane can be obtained by changing the D_2O/H_2O ratio in the Ringer's solution and using neutron radiation. The structure factors for orders 0 to 10, respectively, are as follows: x-rays (2871, 52.5, -14.1, -2.35, 44.9, 10.7, -99.4, -147, -64.1, 45.4, and 59.1); neutrons-D_2O (1348, -323, 127, 351, 228, 16.1, -41.2, 16.2, 27.4, -30.8, and -60.4); neutrons-H_2O (-50.1, 66.5, -23.4, -49.8, -13.3, 2.13, -35.0, -62.5, -30.1, 22.9, and 32.6).

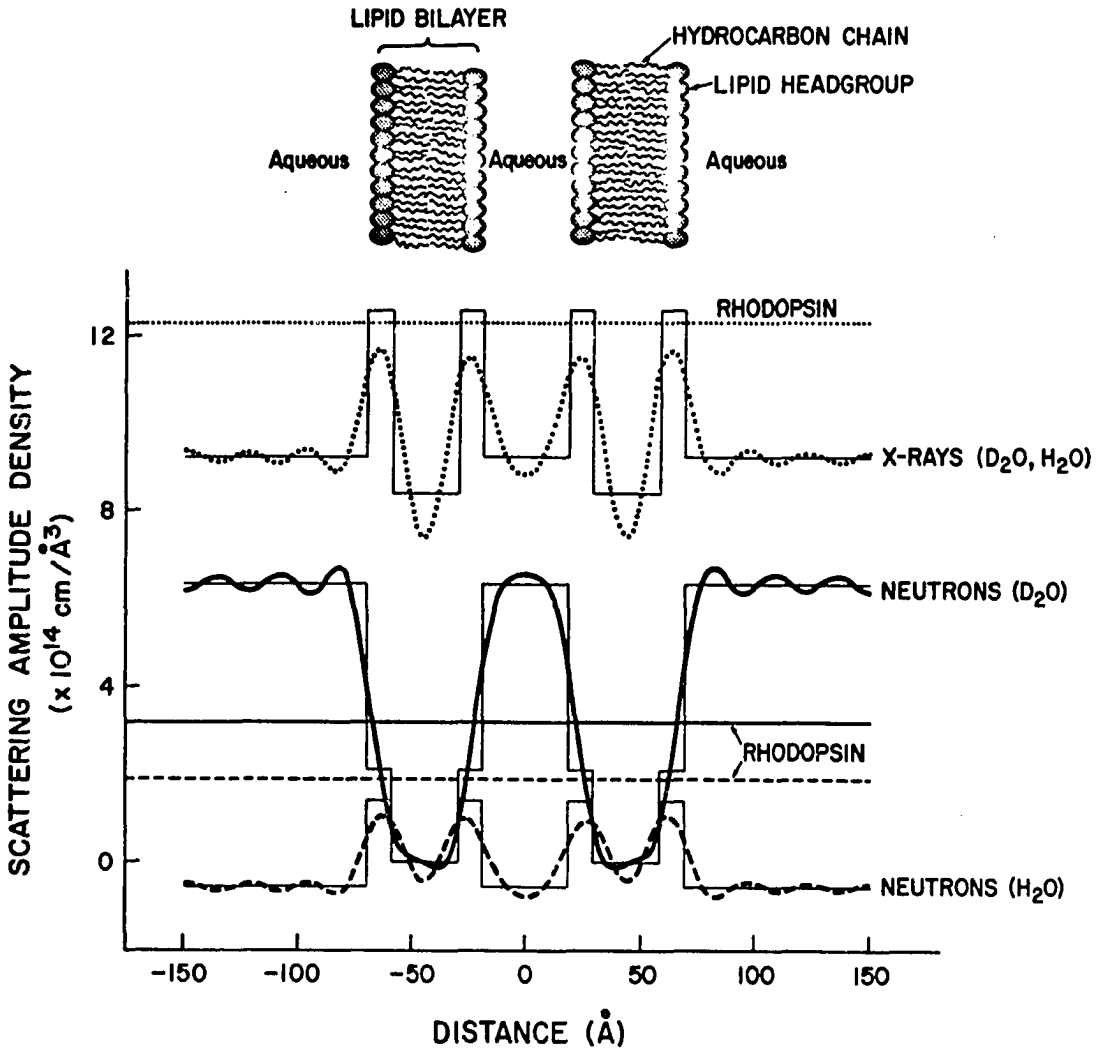

between structural components in x-ray experiments, may partly account for the controversy among x-ray workers regarding the location of rhodopsin in the disc membrane. In D_2O, the contrast between rhodopsin and the phospholipid headgroups is more than four times higher for neutron diffraction than for x-ray diffraction.

Not only is the contrast between the aqueous and hydrocarbon domains enhanced by conducting the experiment with neutron radiation in D_2O, but the scattering density in the aqueous regions can be changed up to twelve-fold by simply altering the H_2O-D_2O ratio of the Ringer's solution. Many different images of the membrane can be obtained in this way. Although the electron density of water can be increased up to 20% by adding salts or sugars in an x-ray experiment, the resulting structure is not necessarily isomorphous with the native one. Worthington (1973) has suggested that the thickness of the disc membrane changes in glycerol.

The molecular interpretation of neutron Fourier syntheses is markedly facilitated by placing the density profiles from experiments in different D_2O-H_2O mixtures on an absolute scale. This can also be done with x-ray diffraction, but the x-ray scattering density can only be altered over a much smaller range. Also, the absolute density scale determined in an x-ray experiment may not be as reliable as one determined by neutron diffraction because the series termination error for membrane systems is likely to be greater with x-rays. This increased error is indicated in Figure 5 by the greater deviation of the dotted x-ray profile from its step-function model compared to the neutron profile in D_2O relative to its step-function model. This greater truncation error is due to the larger fluctuations of electron density inside

the lipid bilayer as seen with x-rays. It is interesting to note that the lipid headgroups are not well resolved in the neutron scattering density profile in D_2O but are clearly discernible in H_2O. Also, the neutron and x-ray diffraction images of the membrane in H_2O are qualitatively similar at low resolution, although the absolute scattering densities are different.

The contrast enhancement achieved by using neutron radiation with H_2O-D_2O exchange is analogous to the staining procedures used by electron microscopists to enhance the contrast in their specimens. It should be emphasized that the neutron method employing H_2O-D_2O exchange is an innocuous staining procedure. Isomorphous H_2O-D_2O exchange can also be used to assign phases and place neutron Fourier syntheses on an absolute scale.

CHAPTER III

METHODS

(a) Dissection and Mounting of Retinas for Neutron Diffraction

Rana catesbiana bullfrogs were obtained from the Connecticut Valley Biological Supply Co. (Southampton, Mass.) or from the Mogul-Ed Biological Supply Co. (Oshkosh, Wis.). Tetracycline (250 mg daily) was administered orally to frogs that exhibited "red-leg" disease (Gibbs, 1963; Nace, Culley, Emmons, Gibbs, Hutchison and McKinney, 1974). Frogs were kept at room temperature in cages that provided both an aqueous and a dry environment. Bullfrogs were used because the dissected retinas were quite large, $\sim$1.5 cm in diameter.

The Ringer's solution contained 115 mM NaCl, 2.0 mM KCl, 2.0 mM $CaCl_2$, 20 mM dextrose, 10 mM trizma base, 1.0% (w/v) streptomycin sulfate and 1.0% (w/v) penicillin-G. The pH or pD of the Ringer's solution was titrated to 7.35 $\pm$ 0.5 at 5°C using HCl or DCl (Thompson-Packard). For experiments in different D_2O-H_2O mixtures, a solution with the desired volume fraction of D_2O was prepared by mixing the approriate volumes of H_2O and D_2O Ringer's. Hypertonic Ringer's solution was prepared by adding sucrose to isotonic D_2O Ringer's (w/v), and hypotonic Ringer's solutions were prepared by mixing isotonic D_2O Ringer's with pure D_2O (v/v). All operations with D_2O were carried out as rapidly as possible to minimize exchange with atmospheric H_2O.

Several dissection procedures were tested to minimize the dissection time without damaging the tissue. The statement made by Huxley

and Brown (1967) regarding the variability of performance of different muscles is pertinent here: "We found it worthwhile to be exceptionally careful and painstaking during the dissection, and an extra hour here was time well spent. The responsible factors are not easy to identify or assess, and general experience was probably the main one."

A dozen eyes were dissected for each neutron scattering experiment, and the specimen preparation was carried out in five stages: decapitation, enucleation, removal of retinas and pigment epithelium, equilibration, and mounting of retinas in the specimen cell. Frogs were dark-adapted for at least 6 hrs, and the dissections were performed under dim red light with wavelengths > 640 nm using Corning CS-2-64 filters. The surgical instruments and sample holders were sterilized before each dissection.

Frogs were sacrificed using a Harvard Apparatus (Mills, Mass.) small animal decapitator, and the heads were wrapped in aluminum foil and stored in ice while the dissection for each head was carried out. The eye cups were enucleated by hemisecting the eyeball in a single cut with a razor blade, tangential to the head of the frog and posterior to the ora serrata. The musculature and optic nerve were cut using a Bard-Parker scalpel with a #15 surgical blade, and the eye cups were transferred to a Petri dish filled with Ringer's solution. The eye cups were maneuvered by holding the sclera with rat-tooth micro-dissecting forceps (Roboz Surgical Instrument Co.). With the use of Dumont #5 forceps, the retina and its attached pigment epithelium were peeled away from the sclera, and then the pigment epithelium was teased away from the retina as a single sheet. Diffraction patterns from specimens with and without the pigment epithelium were indistinguishable. Decapitation,

enucleation, and removal of the retinas and pigment epithelium required about 75 minutes for 12 eyes. The Petri dish was placed on ice, and the retinas were allowed to equilibrate for about 30 minutes. To examine the effect of light, retinas were bleached in white light during equilibration.

For the experiments in D_2O Ringer's solution of varying osmolarity, the retinas were draped over aluminum slats 4.13 x 0.79 x 0.064 cm, which were then mounted on two parallel rods in an aluminum specimen cell (6.4 x 5.7 x 1.27 cm) (Figure 6). When the aluminum slats were clamped together, the space between adjacent slats was 1.2 mm. This space allowed the photoreceptor layers of apposed retinas to just touch one another. The incident neutron beam was attenuated 60% by passing through D_2O samples with a thickness of 9.5 mm. Sample cells with a path length of 3.2 mm were used for the experiments in different mixtures of D_2O and H_2O because of the increased beam attenuation from incoherent scattering of hydrogen. The retinas were therefore bisected before being draped over the thinner aluminum slats. The retinas were cut on a thin layer of Bioloid paraffin embedding compound spread on the bottom of the Petri dish. The mounting of the retinas in the specimen cell required about 30 minutes. The specimen cell was attached to a water jacket maintained at 5°C (Figure 6). Luer-Lok fittings attached to the specimen cell allowed continuous cycling of oxygenated Ringer's solution by peristaltic pumping at a flow rate of about 1.5 ml/hr.

No evidence of specimen deterioration due to the use of aluminum was detected. Aluminum was used because it is opaque to light and transparent to neutrons.

Figure 6. The sample holder and scanning apparatus allowed for a number of degrees of freedom in the orientation of the rods with respect to the incident beam. The sample holder was mounted on a water jacket which could be rotated to obtain the equatorial and meridional diffraction, and the axis on which the jacket was mounted could be rotated to change the angle, ω. The 4.1 cm double-headed horizontal arrow on the face of the water jacket indicates the direction of the rod outer segments and is parallel to the scanning axis 2θ. The meridional Bragg diffraction was collected with the sample in this orientation ($\chi = 0°$). The equatorial scattering was observed with the sample rotated to $\chi = 90°$ so that the retinal rods were perpendicular to the 2θ axis (double-headed arrow vertical). The face of the sample holder has been removed to show the parallel array of 10 aluminum bars over which the retinas were draped.

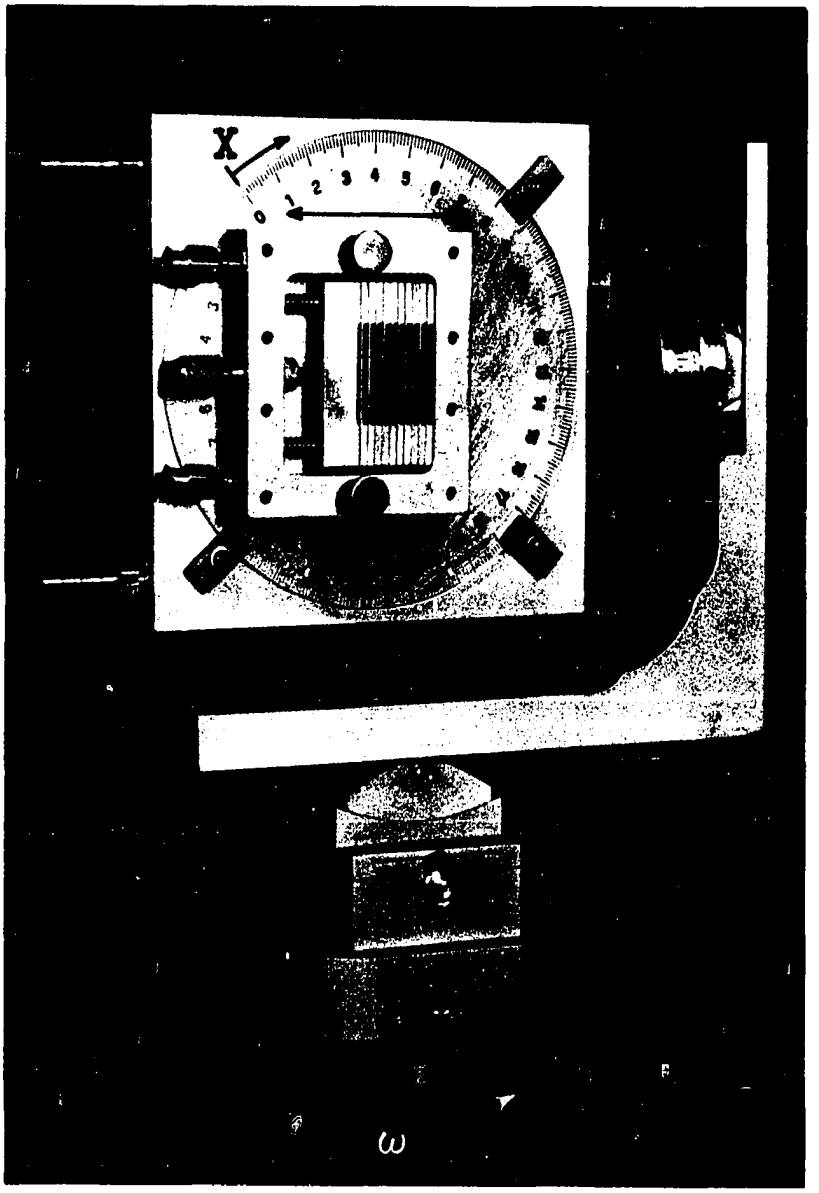

(b) Neutron Diffraction Methods

Neutrons were generated by fission of U^{235} at the High Flux Beam Reactor at Brookhaven National Laboratory (Figure 7). The D_2O-moderated and beryllium-filtered neutron beam passed down a 6-meter nickel-plated beam pipe, and the beam flux was measured by a monitor. Neutron diffraction data were collected on a paired Soller slit, step-scanning diffractometer (Figure 8) (Nunes, 1973; Moore, Engelman and Schoenborn, 1974; Soller, 1924). Soller slit collimators were placed before and after the specimen. The dimensions of the spaces between Soller slits were 1.9 x 0.24 cm. The Soller slit vanes were 71 cm long and the aperture measured 1.9 x 1.9 cm. A pyrolytic graphite monochromator was used to select a wavelength band at 4.19 Å ($\Delta\lambda/\lambda$ = 0.025) from the scattered neutrons, which were Bragg-reflected into a ^3He detector. The size and mosaic spread of the graphite crystal allowed detection of all neutrons that passed through the detecting Soller slits. The horizontal beam divergence was 9', and the vertical beam divergence ($\sim$0.4° at the sample) was defined by the beam pipe rather than by the apertures and heights of the Soller slit collimators. The wavelength was calibrated by θ:2θ scans of the 002 reflection from a pyrolytic graphite crystal placed in the sample position.

The meridional Bragg diffraction was recorded at ω = 0° and χ = 0° with the planes of the retinas perpendicular to the 2θ axis of the detector, so that the retinal rods were parallel with the 2θ axis (Figures 6, 8 and 9). The equatorial diffraction was obtained by rotating the sample to χ = 90° so that the rods were perpendicular to the 2θ axis. Persistence-with-tilt experiments were done by tilting the sample to values of ω and scanning 2θ. Rocking curves were recorded with the

Figure 7. Experimental floor of the High Flux Beam Reactor at Brookhaven National Laboratory. The shielding of the reactor core is located in the top left portion of the picture. The Soller slit diffractometer shown schematically in Figure 8 is located in the bottom right, and the beam pipe passes from the reactor core to the diffractometer. The two-dimensional position-sensitive detector used to collect the data in Figures 10(d) and 37 is located in the top center of the picture.

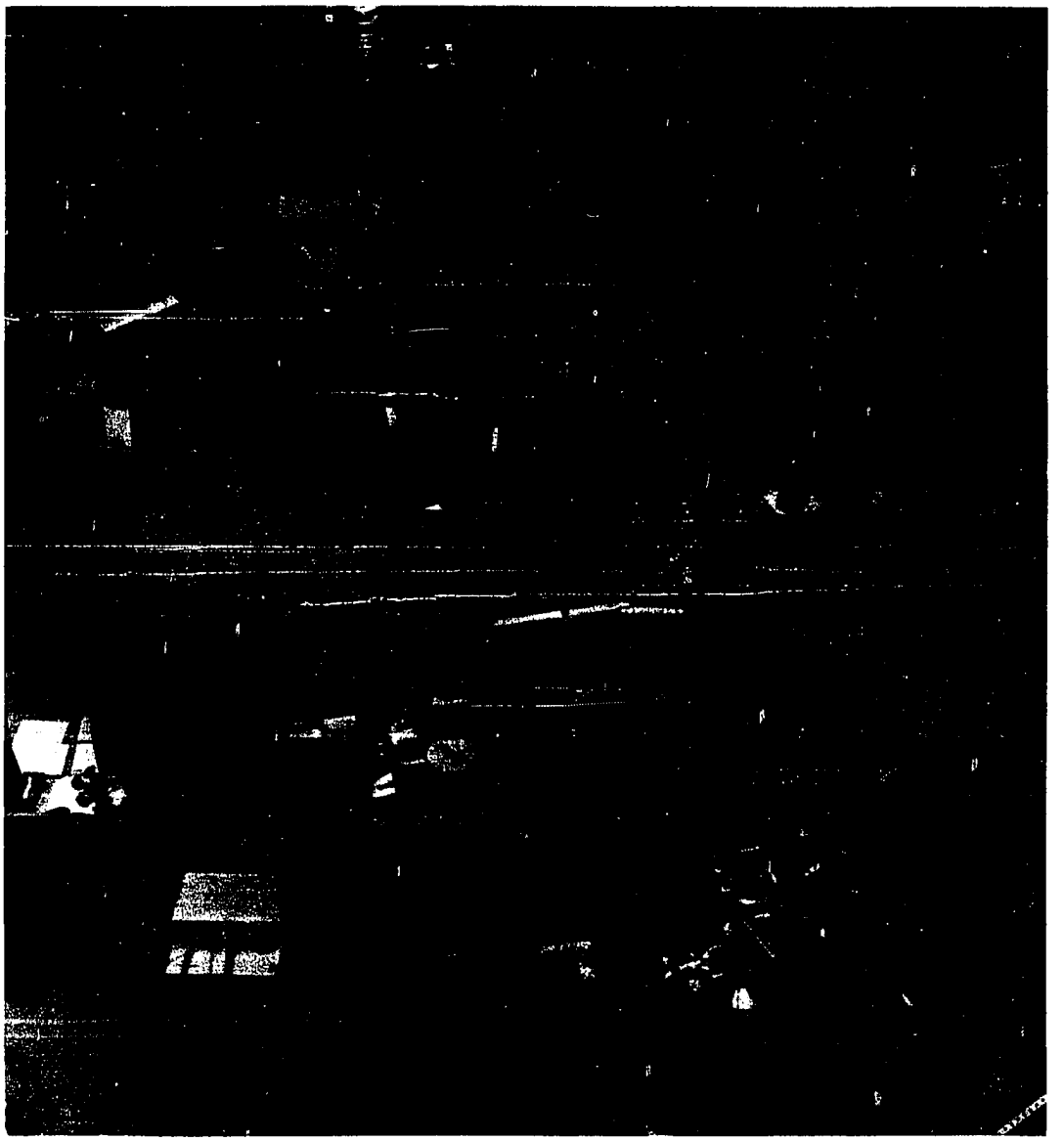

Figure 8. Diagram showing a top view of the Soller slit step-scanning diffractometer at the High Flux Beam Reactor at Brookhaven National Laboratory, [λ = 4.19 Å, $\Delta\lambda/\lambda$ = 0.025, flux $\sim 10^6$ neutrons/cm^2-sec].

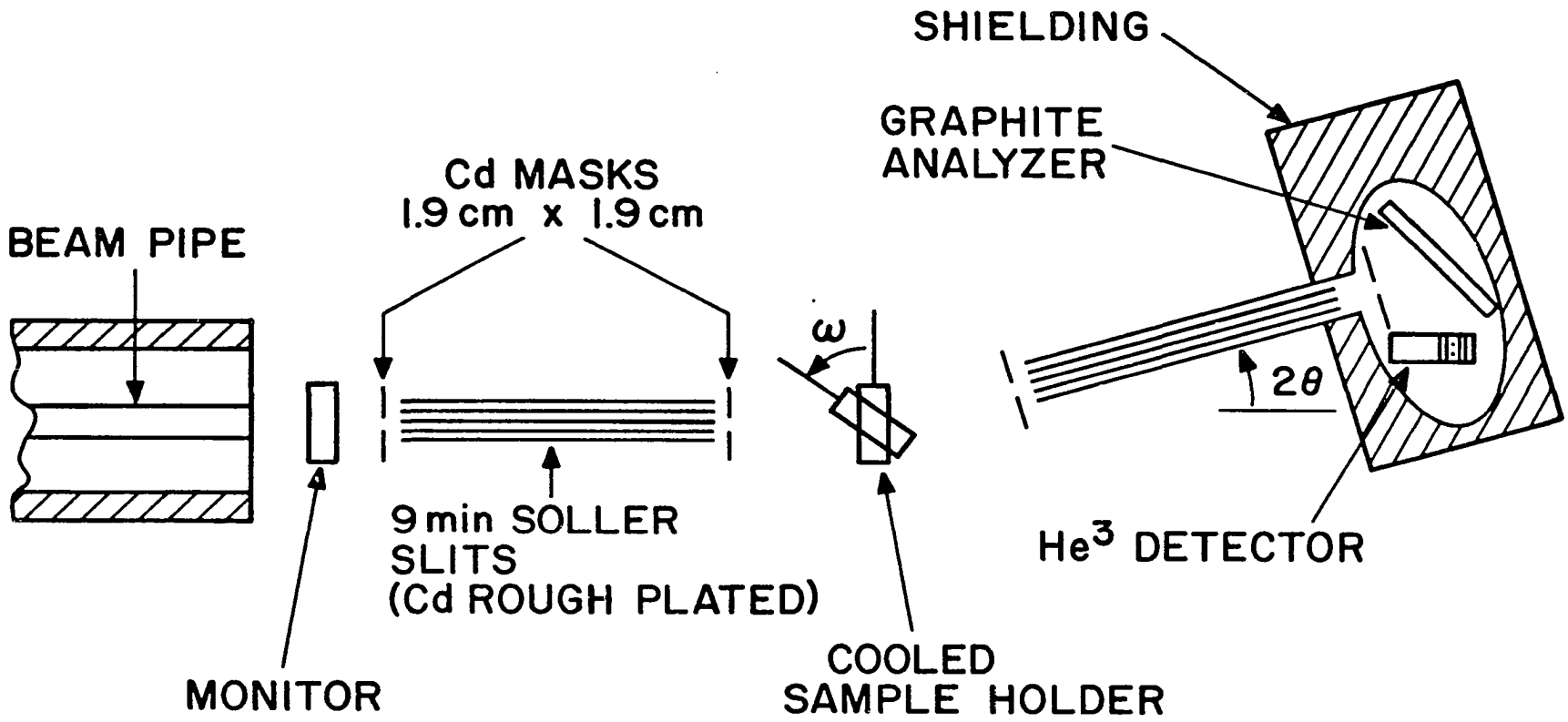

Figure 9. Schematic diagram showing the geometry of the rod outer segments with respect to the incident neutron beam. The meridional diffraction was observed with the sample oriented as shown at $\omega = 0°$ and $\chi = 0°$. The equatorial diffraction was observed with the sample rotated to $\chi = 90°$. Rocking curves were measured by rotating the rods in ω at a fixed 2θ for reflection h. The arcs drawn through the tips of the rods trace out a surface of disorientation. The rotationally symmetric disorientation of the rods causes the reflections in reciprocal space to be spread out into caps of spheres with radii and arc lengths proportional to h.

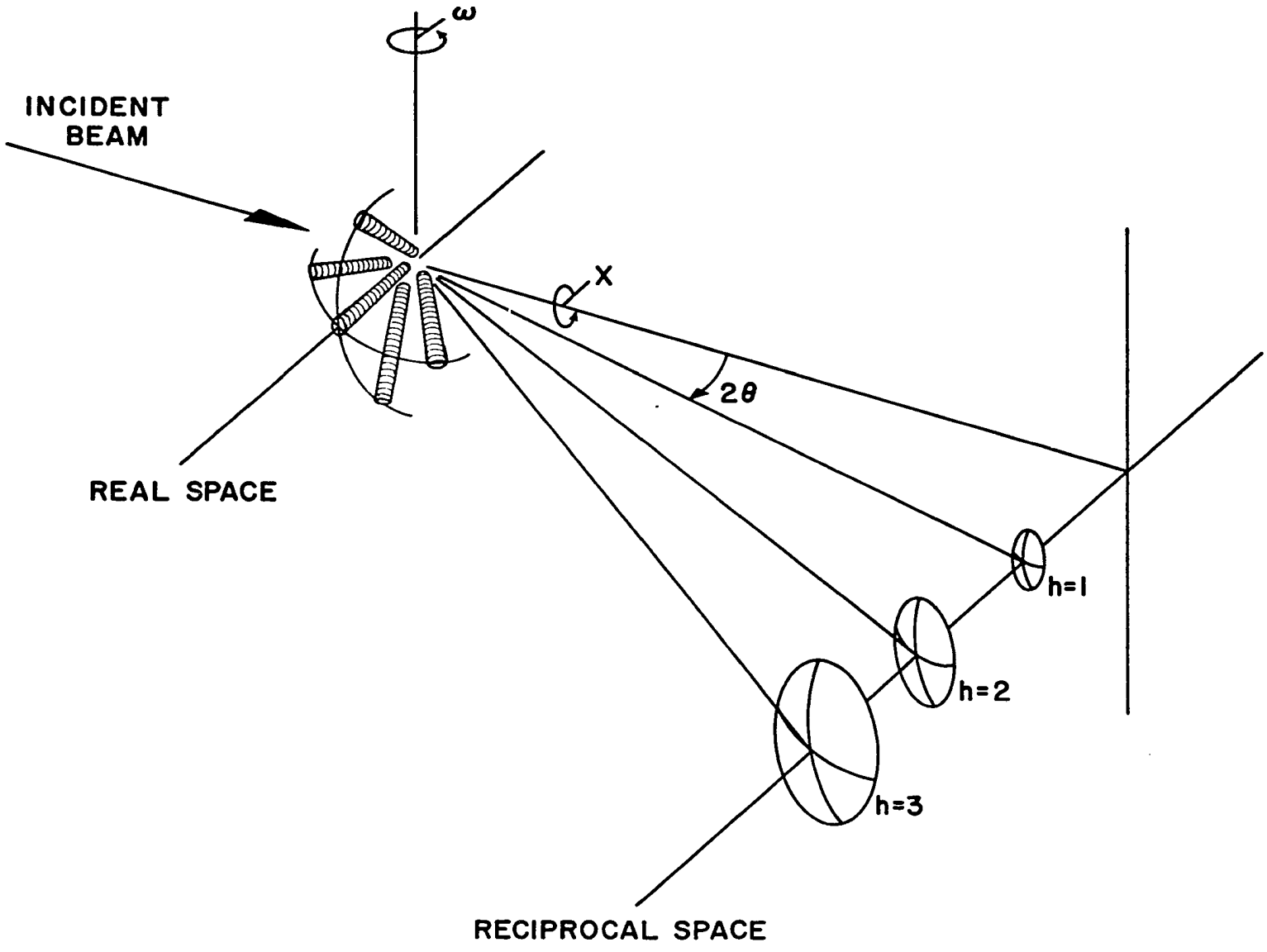

detector set at a fixed 2θ, and the angle of the rods with respect to the incident beam was changed by rotating the sample axis in ω.

The meridional and equatorial diffraction patterns were recorded from 2θ = 0.24 to 7.20° in increments of 0.08°. The Scientific Data Systems computer which controlled the diffractometer was programmed to collect a specified number of monitor counts at each scattering angle (10^6 monitor counts/$\sim$110 sec). In 100 and 80% D_2O Ringer's solution the region from 0.24 to 2.80° was scanned for $\sim$35 min ($\sim$1 min/angle), and the region from 2.80 to 7.20° was scanned for $\sim$2.5 hrs ($\sim$2.5 min/angle). In 60 and 40% D_2O Ringer's the diffraction pattern was scanned for $\sim$3.5 hrs ($\sim$2.5 min/angle) and $\sim$5 hrs in 30% D_2O. In 20 and 0% D_2O no signal could be detected when scanning for $\sim$7 hrs ($\sim$5 min/angle). Eighty-two days of beam time were used in 9 periods from May 1973 to February 1975.

CHAPTER IV

RESULTS AND DATA ANALYSIS

(a) Integrity of Rod Structure

The two principal obstacles in neutron diffraction work with biological tissue are the finite stability of the samples and the low flux of the neutron beam. Specimen holders were designed to accommodate a parallel array of ten dissected retinas to provide a sufficient number of rods in the neutron beam for diffraction to be observed. Our initial experiments (Figure 10a) showed diffraction with a 300 Å period, but the signal was very weak, and the Bragg peaks deteriorated and disappeared in a few hours. Improvements in the design of the specimen holder and in the dissection technique led to a stronger signal (Figure 10b), but the diffraction pattern still deteriorated with time. Several means were used to improve the stability of the diffraction: the dissections were carried out as rapidly as possible without compromising sample orientation; the retinas were maintained at 5°C; and oxygenated Ringer's solution containing antibiotics and glucose was continuously flowed through the sample cell. The diffraction patterns were thereby stabilized for several hours, which allowed the summation of repetitive scans of the pattern (Figure 10c). A striking improvement in the diffraction patterns was achieved by using a two-dimensional position sensitive detector (Alberi, Fischer, Radeka, Rogers, and Schoenborn, 1975) and only a pair of retinas (Figure 10d). This 8-hour diffraction pattern shows 9 orders of a 300 Å period and contains structural information to a

Figure 10. Neutron diffraction patterns from ∿10 Rana catesbiana frog retinas equilibrated in D_2O Ringer's solution. Patterns (a), (b), and (c) show successive enhancement of Bragg diffraction achieved by improvements in dissection technique, specimen stability, and sample-cell design. These patterns were obtained using a step-scanning Soller slit diffractometer (Figure 8). Pattern (d) was obtained with only two retinas in the beam; a two-dimensional positive-sensitive detector with slit collimation was used [λ = 2.37 Å, $\Delta\lambda/\lambda$ = 0.02, flux ∿10^7 neutrons/cm^2-sec].

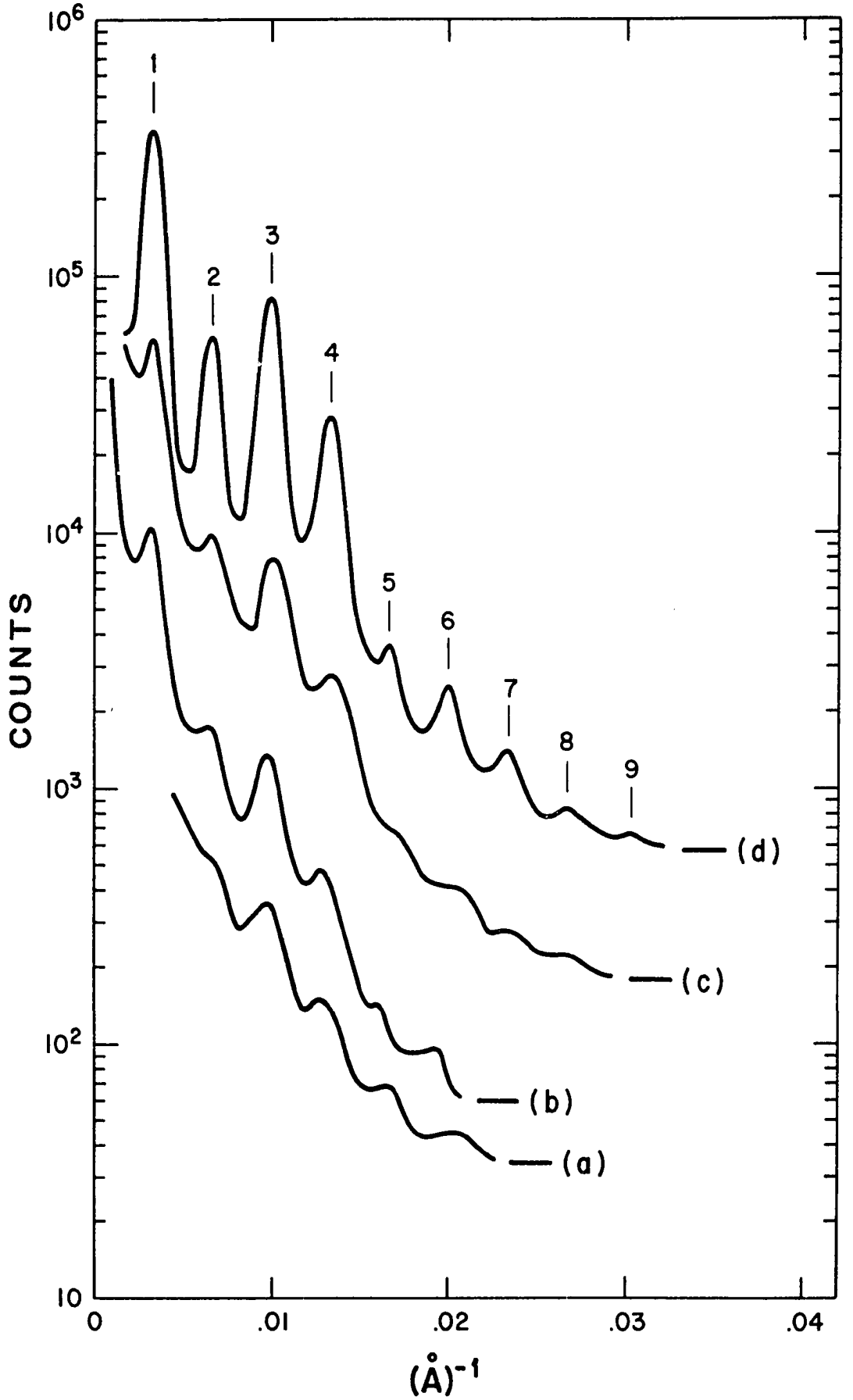

resolution comparable with that of x-ray experiments.

The birefringence of rod outer segments was used to monitor the specimen integrity. The edgefold preparations (Denton, 1954) displayed little or no birefringence from samples whose Bragg diffraction had deteriorated. Rod outer segment birefringence after the neutron diffraction experiments was routinely strong, as shown in Figure 11. Also, neutrons do not bleach rhodopsin because the retinas were pink and detergent-solubilized rhodopsin displayed almost no change in absorbance at 498 nm after neutron irradiation.

Neutron diffraction experiments conducted in D_2O Ringer's of varying osmolarity not only strengthened the validity of the reflection phase assignments but also served as a second test of structural integrity. The neutron diffraction patterns in Figure 12 were recorded from dark-adapted retinas equilibrated in 2% sucrose (w/v), isotonic, 0.8 diluted, and 0.6 diluted D_2O Ringer's solutions. Diffraction patterns recorded from bleached retinas equilibrated in D_2O Ringer's solution were quite similar to the dark patterns. The osmotic sensitivity of the rod outer segments is clearly shown in Figure 13 in which the dark patterns recorded in 0.8 diluted Ringer's solution and 2% sucrose Ringer's solution are superimposed. The reflections shift to lower scattering angles and the repeat spacing between discs increases as the hypotonicity of the Ringer's increases, consistent with electron microscopic (Dowling, 1967; DeRobertis and Lasansky, 1961; Brierley, Fleischman, Hughes, Hunter and McConnell, 1968; Clark and Branton, 1968; Cohen, 1971; Heller, Ostwald and Bok, 1971; Korenbrot, Brown, and Cone, 1973) and x-ray diffraction experiments (Blaurock and Wilkins, 1972; Blaurock, 1972; Corless, 1972; Chabre and Cavaggioni, 1975). Although the reflections recorded in 0.4

Figure 11. Photomicrograph showing strongly birefringent rods in an edgefold preparation. The horizontal bright line is where the retina has been folded. The top field shows free-floating birefringent rods, broken off from the surface of the retina. The lower field of the photomicrograph shows the plane of the retina.

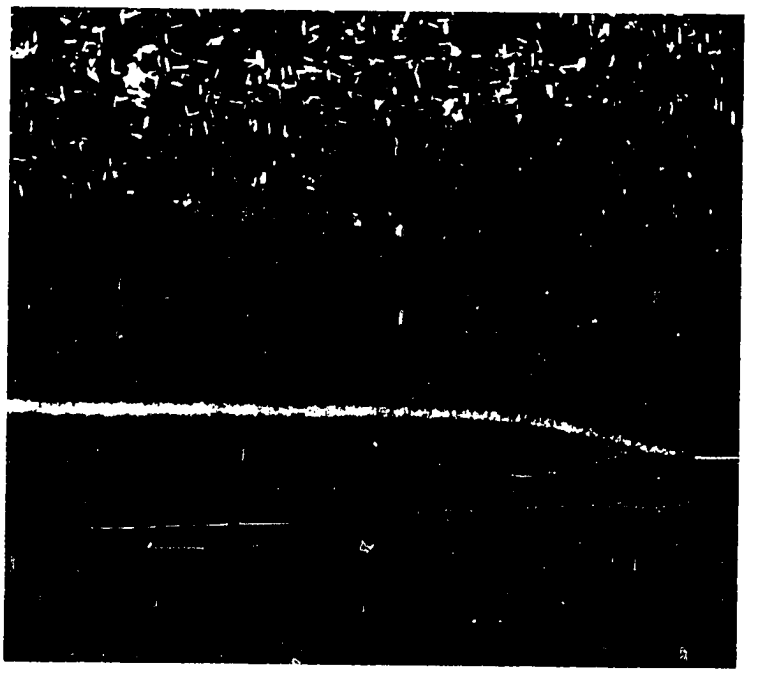

Figure 12. Neutron diffraction patterns of intact retinas equilibrated in D_2O Ringer's solution of varying osmolarity. (a) 2% sucrose Ringer's solution, d = 294 Å; (b) isotonic Ringer's solution, d = 298 Å; (c) 0.8 diluted Ringer's solution, d = 308 Å; (d) 0.6 diluted Ringer's solution, d = 328 Å. The height of the data bars here and in succeeding figures represent ± 1 standard deviation, assuming Poisson counting statistics. Continuous curves through the data bars are the sums of polynomial fits to the background scattering (••••••) and Gaussian peaks fitted to the background-subtracted reflections.

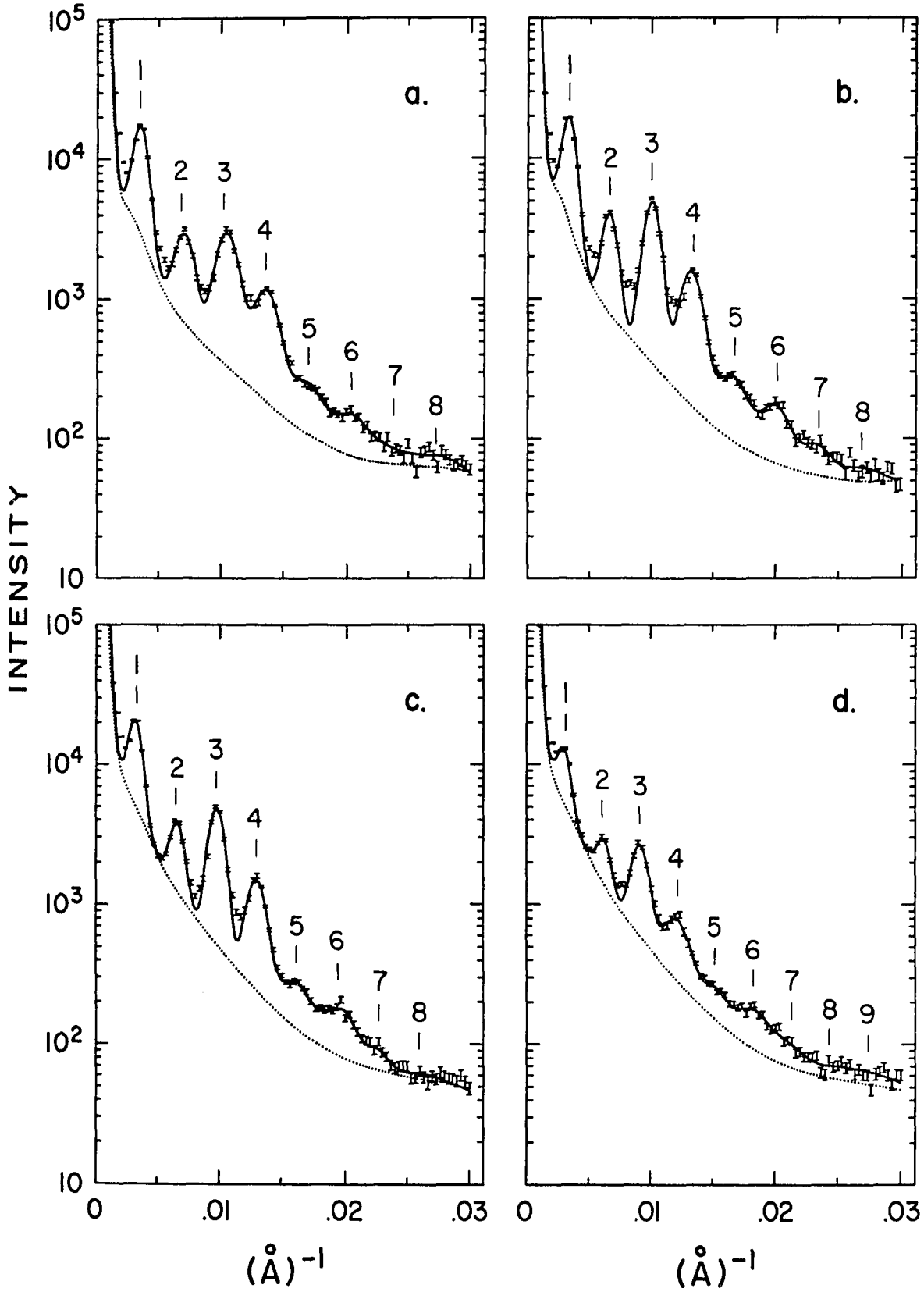

Figure 13. The reflections in 2% sucrose Ringer's solution with a spacing of 294 Å (primed) are shifted to higher reciprocal spacings compared with the reflections in 0.8 diluted Ringer's solution with a repeat spacing of 308 Å.

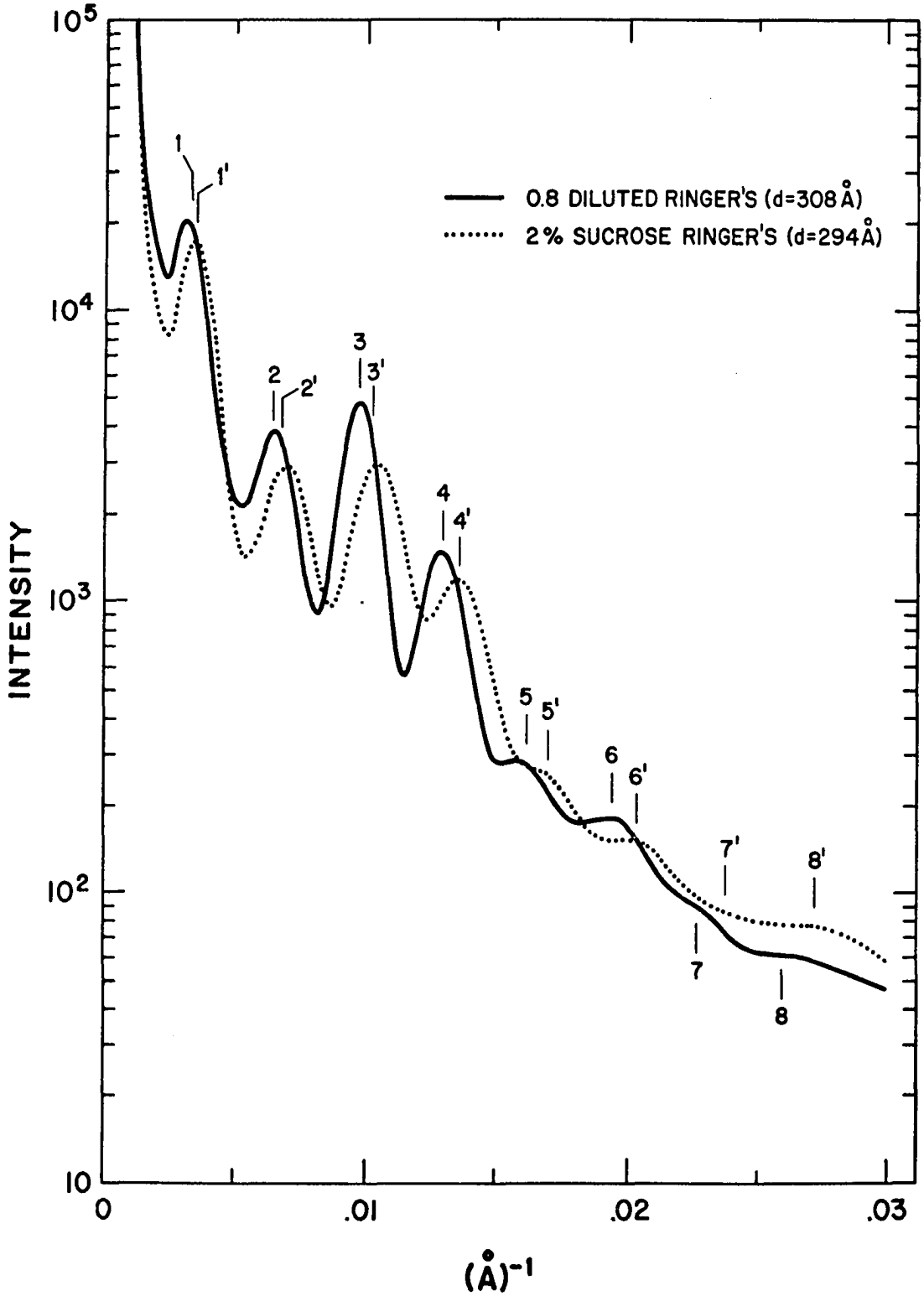

diluted Ringer's solution were broadened, they could be indexed to a unique period of 375 Å. However, in 4% sucrose Ringer's solution two repeat spacings of 285 Å and 230 Å were detectable. Two repeat spacings in hypertonic sucrose solutions have also been observed by x-ray diffraction (Chabre and Cavaggioni, 1975).

The most compelling evidence for specimen integrity in D_2O Ringer's solution was that x-ray diffraction patterns in this medium (Figure 14) were indistinguishable from those recorded in H_2O Ringer's solution. If the structures in H_2O and D_2O are isomorphous, then the two patterns should be identical, since H_2O and D_2O have the same electron density (see Figure 4).

(b) Neutron Diffraction Patterns in D_2O-H_2O Mixtures

Neutron diffraction patterns from retinas equilibrated in 100, 80, 60, 40 and 30% D_2O Ringer's solution (Figure 15) exhibit meridional Bragg reflections with a period of 295 $\pm$ 5 Å. The smooth curves through the Bragg peaks are the sums of the diffuse equatorial scattering (dotted curves) and Gaussian peaks fitted to the meridional scattering after subtraction of the equatorial scattering. The effect of D_2O concentration on the diffraction patterns is clearly seen by superimposing the curves obtained in 100 and 60% D_2O (Figure 16). The difference between the Bragg peaks and the equatorial scattering is directly related to the coherent intensity of the reflections. The decrease in the coherent intensity of the reflections as the Ringer's solution is made richer in H_2O suggests that the contrast within the structure diminishes as the H_2O concentration increases.

(c) Systematic Errors

In addition to statistical errors which limit the precision of the

Figure 14. Line-focus x-ray diffraction pattern of a strip of intact Rana catesbiana frog retina equilibrated in D_2O Ringer's solution. This x-ray pattern is indistinguishable from those recorded in H_2O Ringer's solution (Blaurock and Wilkins, 1969; Gras and Worthington, 1969; Corless, 1972; Chabre and Cavaggioni, 1973).

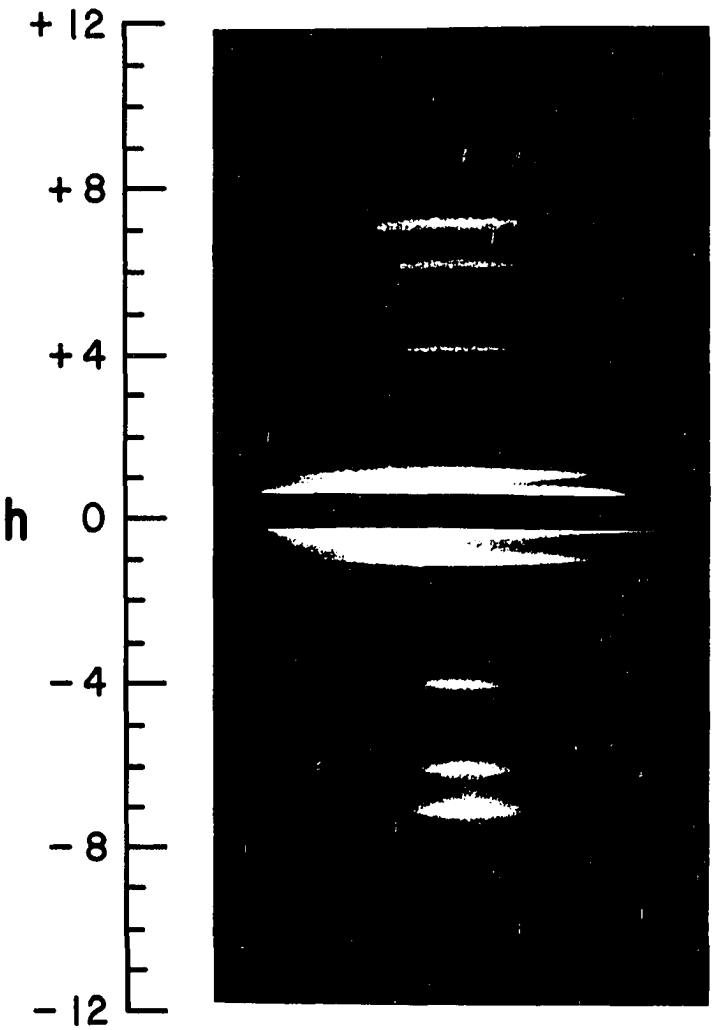

Figure 15. Meridional neutron diffraction patterns of intact retinas in 100, 80, 60, 40, and 30% D_2O Ringer's solution. Continuous curves through the data bars are the sums of polynomial fits to the background scattering (·····) and Gaussian peaks fitted to the background-subtracted reflections.

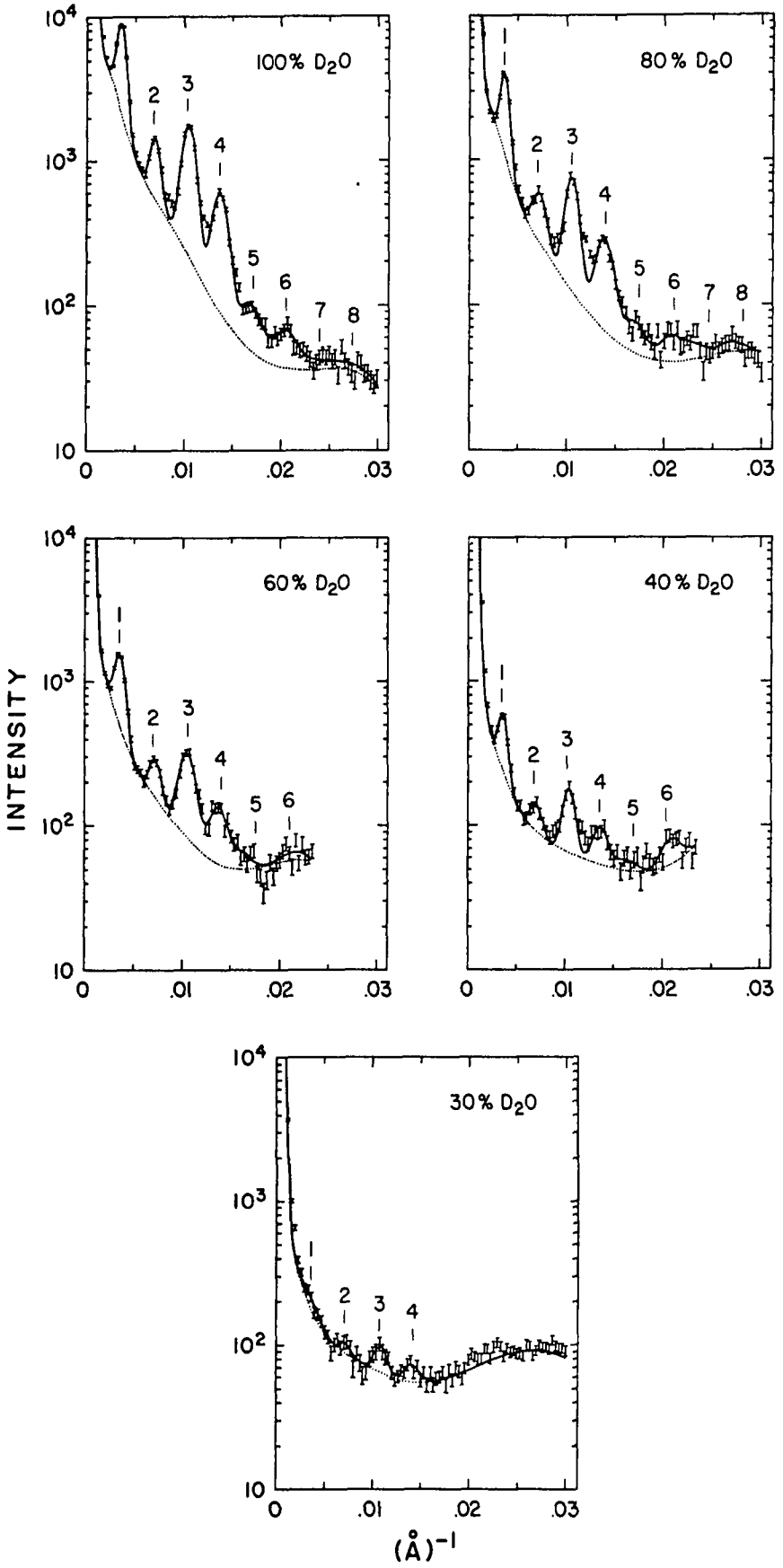

Figure 16. The coherent intensity of the reflections in 60% D_2O Ringer's solution is reduced compared with the reflection intensities in 100% D_2O Ringer's solution.

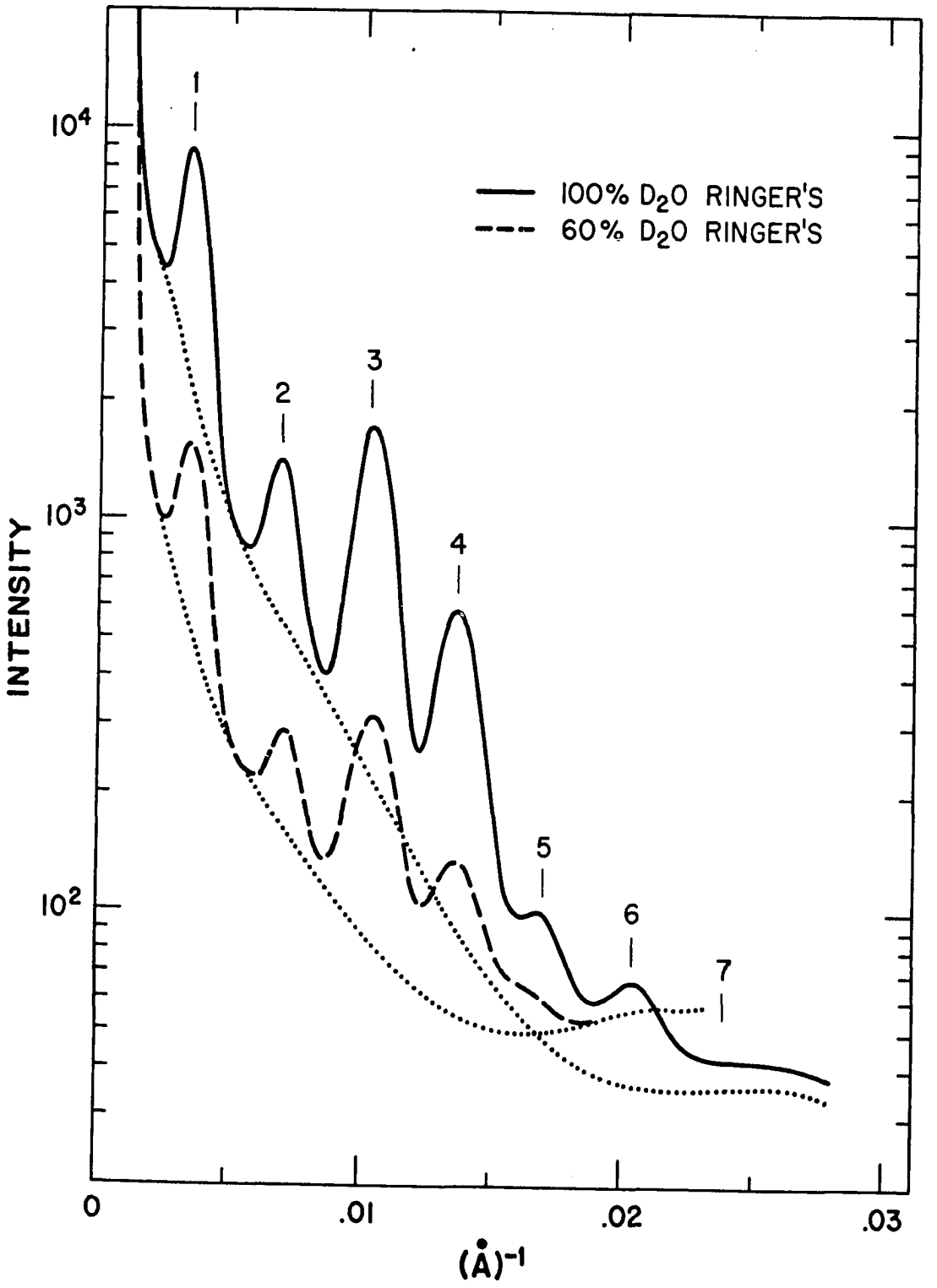

observed diffraction, several sources of systematic error hinder the measurement of the integrated intensity of a reflection. These include absorption, extinction, polarization, disorder, simultaneous reflections, chromatic and geometrical aberrations, background and the Lorentz factor. The reader is referred to Arndt and Willis (1966) for an excellent discussion of technical considerations in x-ray and neutron diffraction.

Absorption effects arise because the path length of the beam through the sample is dependent on the scattering angle. At higher scattering angles the path length increases, and the scattered radiation is exponentially reduced. Absorption effects can be significant in x-ray diffraction and are due principally to the photoelectric effect. For neutrons, absorption by nuclear capture is usally negligible except for nuclei such as cadmium, boron, gadolinium and other rare earths (Bacon, 1962). The highest scattering angle considered in the structural analysis including 8 reflections [Chapter VI(d)] was 7.2°. At such low angles the variation in path length of the diffracted rays passing through the sample is very small. Therefore, absorption corrections were not necessary. Incoherent neutron scattering from hydrogen manifests itself in the same way as true absorption, causing attenuation in the scattered intensity. This attenuation was corrected for by normalizing the scattering profiles to the intensity of the direct beam transmitted through the samples. This normalization is much simpler in neutron diffraction studies than in x-ray studies because the intensity of the incident beam can be easily monitored.

Extinction is the attenuation of the incident beam as a result of Bragg diffraction. This attenuation can result from multiple internal reflections in the crystal (primary extinction) or from the reduction of

the intensity of the incident beam impinging on a crystal plane due to Bragg diffraction from preceding planes (secondary extinction) (Woolfson, 1970; Buerger, 1960). The strongest reflections are most reduced in intensity by extinction because they scatter a greater amount of energy from the incident beam than do weaker reflections.

A novel approach used by Caspar and Phillips (1976) for detecting primary extinction in neutron diffraction from myelin membranes is to change the D_2O/H_2O ratio in the Ringer's solution in order to manipulate the contrast in the structure. At low resolution, the internal contrast within the membrane regions does not change, so that one would predict a linear dependence of the structure factors on the percent D_2O. Primary extinction effects would appear as a reduction in the intensity of a strong reflection as the contrast increases, causing nonlinearity in the plot of F versus percent D_2O. This approach has been applied to neutron diffraction from intact retinas (Figure 24). The linearity of the structure factor of the strong first order versus percent D_2O indicates that there is little or no primary extinction in this system.

By varying the thickness of the specimens, secondary extinction due to multiply scattered neutrons from different rods was shown to be negligible. Diffraction patterns recorded from samples equilibrated in isotonic D_2O Ringer's solution in which the path of the beam through the retinas was $\sim$8mm (Figure 12b) and $\sim$2.5 mm (Figure 15) were indistinguishable.

Primary and secondary extinction cause a wavelength dependence of the relative values of the observed intensities for different reflections (Arndt and Willis, 1966). The close resemblance of the diffraction patterns recorded with 2.37 Å neutrons (Figure 10d) and 4.19 Å neutrons

(Figures 12 and 15) also indicates that extinction effects in this system are negligible.

The polarization factor in x-ray diffraction has a value close to unity in low-angle studies and is usually neglected. There is no polarization effect associated with the nuclear scattering amplitude in neutron diffraction.

Disorder can be due to variation of the unit cell repeat spacing (lattice disorder) or variation of the structure within the unit cell (substitution disorder). Methods for treating disorder in one-dimensional crystals have been described by Cain (1974) and by Hosemann and Bagchi (1962). Schwartz, Cain, Dratz, and Blasie (1975) have carried out a detailed analysis of disorder from x-ray studies of retinal rods. In the analysis of my neutron scattering data, lattice disorder was corrected for by fitting Gaussian peaks of variable width to the Bragg reflections.

Simultaneous reflections are recorded when the Bragg reflecting condition is satisfied by more than one family of crystal planes. Simultaneous reflections would not be expected to be recorded from diffraction by one-dimensional crystals, but, if the mosaic spread is large enough, or if there is a slight variation in d spacing, then reflections h - 1 and h + 1 could contribute to the scattering observed for reflection h. The Gaussian-fitting procedure corrected for overlap from nearest-neighbor reflections.

Chromatic and geometrical aberrations due to using a diffractometer with finite apertures and a beam of finite bandwidth have been discussed by Schmatz, Springer, Schelten and Ibel (1974) and by Moore (1976). If the Soller slits caused substantial smearing, then the resolution of the

minima between the Bragg peaks would improve as the height of the Soller slits is reduced. Since the resolution of the reflections does not change as the height of the Soller slits is reduced (Yeager,1976b), slit smearing effects must be quite small. Chromatic aberrations were also small since the bandwidth of the neutron beam was small ($\Delta\lambda/\lambda$ = 0.025).

The instrumental angular resolution can be estimated from (Nunes, 1973)

$$\Delta 2\theta = [\ \Delta_o{}^2 + (\frac{\Delta\lambda}{\lambda} \cdot 2\theta)^2]^{\frac{1}{2}} \qquad (6)$$

where Δ_o is the width of the direct beam and the scattering angle 2θ is less than $\sim 30°$. For the highest scattering angle measured, 7.2°, a direct beam width of 0.24° (FWHM) and $\Delta\lambda/\lambda$ = 0.025, the angular smearing $\Delta 2\theta$, is 0.3°. The angular smearing in 2θ was corrected for by fitting Gaussian peaks of variable width to the Bragg reflections.

The major sources of systematic error in these experiments which required scrutiny were background scattering and the Lorentz and disorientation corrections.

(d) Background Subtraction and Determination of Reflection Intensities

In x-ray diffraction, background scattering has several sources: white radiation, thermal diffuse scattering, incoherent scattering, detector background and parasitic scattering from the sample, the collimators and air. In neutron diffraction, detector background, parasitic scattering and especially incoherent scattering from hydrogen contribute to the background. Given that the observed diffraction pattern contains background scattering, what are the options available for determining the coherent intensity of the Bragg reflections? Certainly if one has several hundred independent reflections with a high signal-to-noise ratio, fairly simple techniques can be used to extract the areas of the Bragg

peaks. One procedure is to select points on either side of a reflection and perform a linear interpolation to define the background level. The coherent intensity of a reflection is then obtained by straightforward subtraction of the background (Schoenborn, 1969). In low-angle diffraction, manual background subtraction is often employed where only a few reflections are recorded. Semi-automated curve fitting procedures were used because of the convenience in analyzing a large number of diffraction patterns and the ease in carrying out a statistical analysis of the data. Since only a few reflections were recorded in each pattern, the influence of each reflection on the Fourier synthesis escalates, and automated procedures provided the most objective approach for determining the reflection intensities.

The background in some previous low-angle studies was determined by fitting a line or smooth curve between the minima around a Bragg reflection (Caspar and Kirschner, 1971; Kirschner, 1971; Worthington and McIntosh; 1974). This approach is valid if the minima between reflections are well-defined plateaus, which indicates that adjacent reflections are resolved. The regions between reflections in the neutron diffraction patterns from retinas were not plateaus, which suggests that adjacent reflections were not completely resolved. Therefore, an experimental approach was used to ascertain the background underlying the Bragg peaks.

(i) Determination of Background Scattering

Special care was taken to obtain the best estimate of the background scattering since the entire retina was exposed to the beam. The best estimate of the background was obtained by rotating the retinas 90° in angle χ from the Bragg reflecting position to obtain the equatorial scattering (see Figures 6 and 9). The diffuse intensity centered at 1/55 $\mathring{A}^{-1}$

in equatorial x-ray diffraction patterns has been interpreted as diffraction between rhodopsin molecules in the plane of the disc membrane (Blasie, Dewey, Blaurock and Worthington, 1965; Blasie, Worthington and Dewey, 1969; Blasie and Worthington, 1969; Blasie, 1972). The equatorial neutron diffraction patterns in Figure 17 are quite featureless compared with the Bragg diffraction (Figure 15) and do not display peaks of intensity centered at 1/55 $\mathring{A}^{-1}$. However, changes are seen in the patterns as the D_2O concentrations is varied (Figure 18). As the D_2O concentration decreases, the scattering at reciprocal space distances $>0.016\ \mathring{A}^{-1}$ increases because of incoherent scattering from hydrogen. The scattering at distances $<0.016\ \mathring{A}^{-1}$ is much greater than that observed with only buffer in the sample cell, and this diffuse scattering probably arises from those constituents of the retina not periodically organized to give Bragg diffraction. The scattering at distances $<0.016\ \mathring{A}^{-1}$ decreases as the D_2O concentration decreases, which suggests that structures causing this diffuse scattering (e.g., protein, lipid and carbohydrate) are being contrast-matched as the D_2O concentration decreases. This diffuse scattering probably arises from nonperiodic constituents of the retina, and so it should be spatially isotropic. The equatorial scattering can thus be used to ascertain the background scattering underlying the meridional Bragg reflections. This approach for obtaining the background would be inapplicable in situations where there is oriented equatorial scattering from the structure. In such situations the scattering between the meridional and equatorial reflections, for instance at 45°, could be used to obtain the background. Use of the equatorial scattering as the background for the meridional scattering is certainly a valid approach for treating that portion of the background contributed by the

Figure 17. Intact retinas were rotated 90° in angle χ from the Bragg reflecting position to obtain the equatorial scattering. The smooth curves drawn through the data bars are polynomial regression fits, which are superimposed in Figure 18.

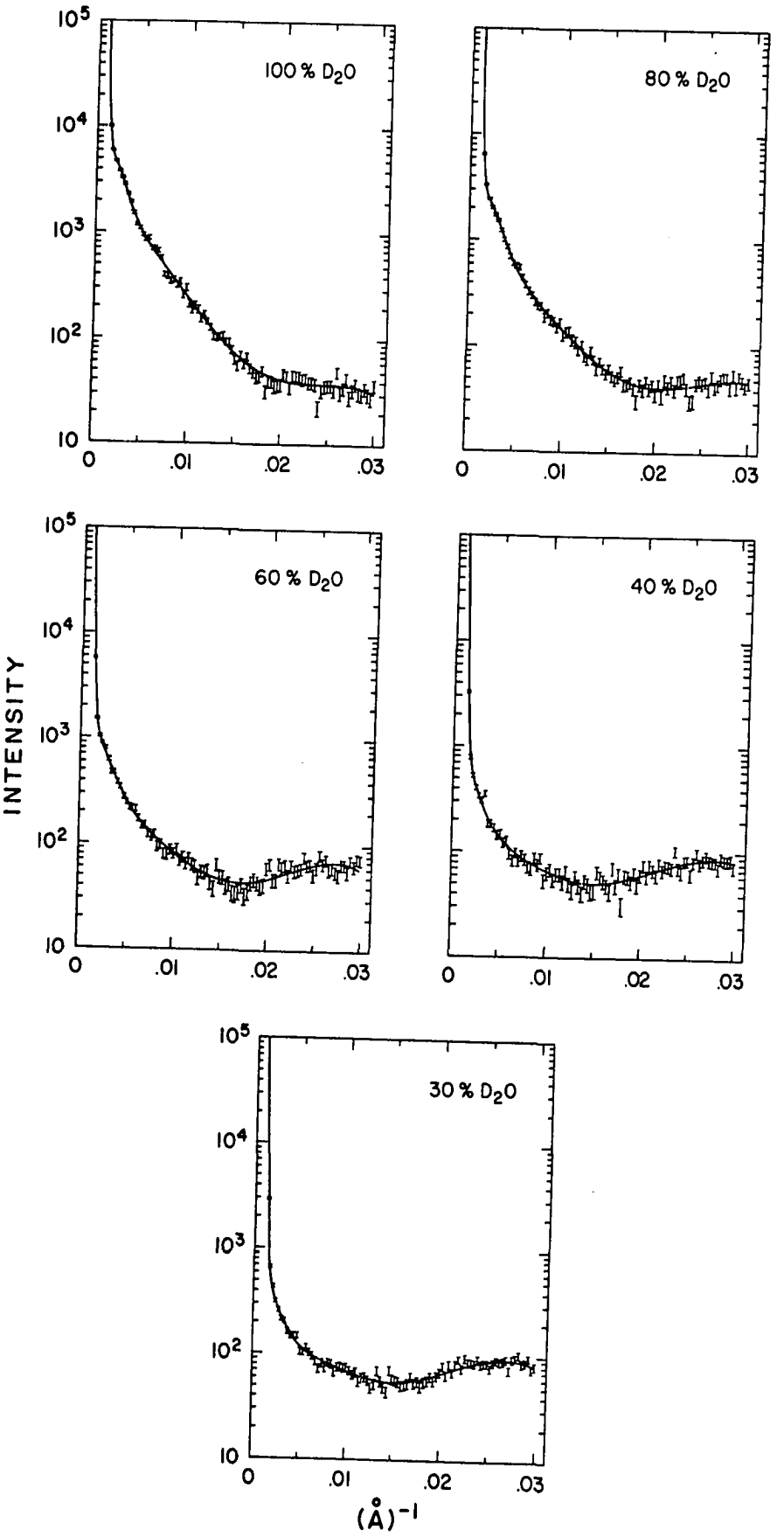

Figure 18. Polynomial regression fits to the equatorial scattering observed from neutron diffraction of intact retinas in different D_2O-H_2O mixtures. The fit to the instrumental background scattering with an empty sample cell in place is shown for comparison.

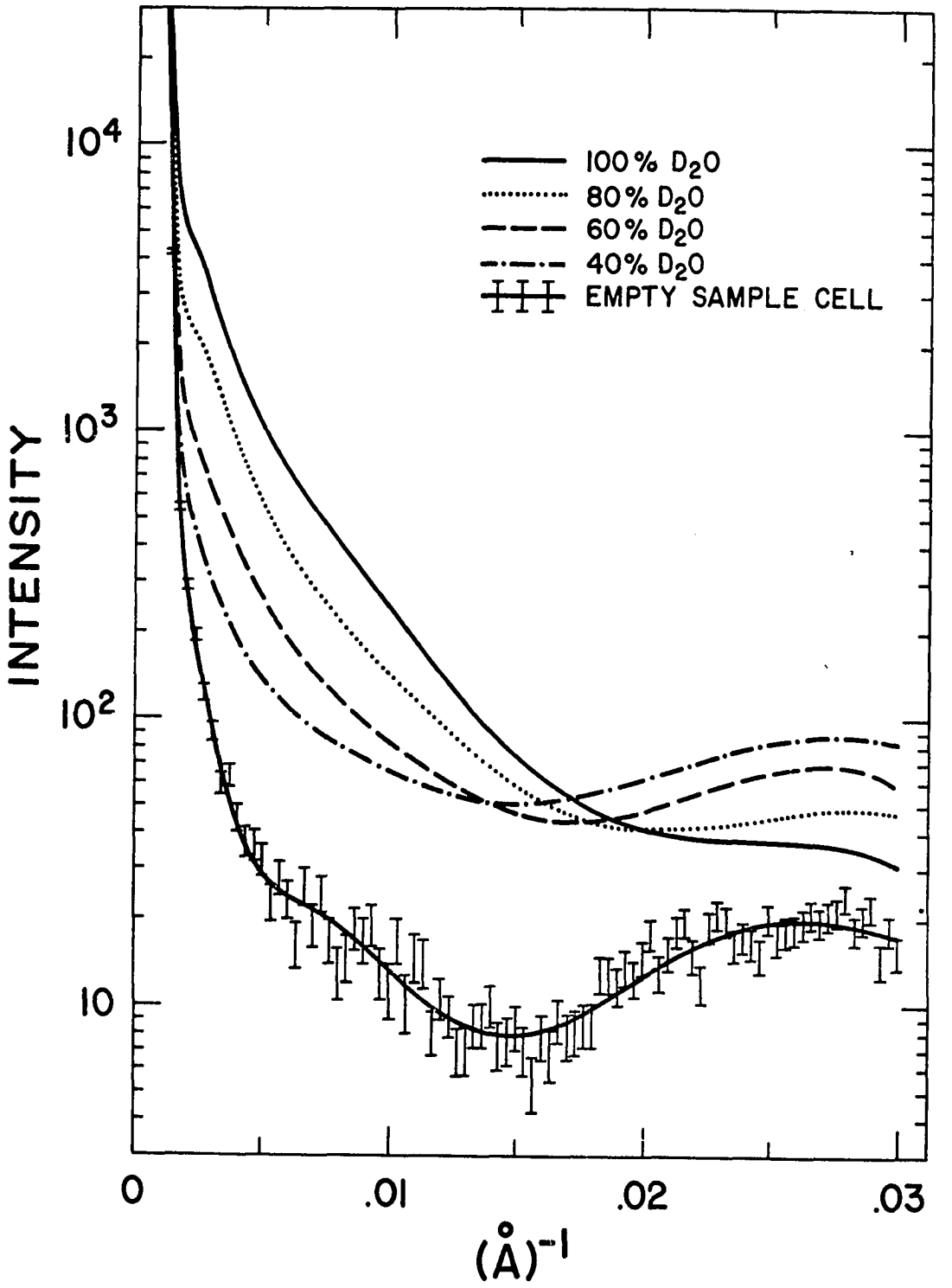

incoherent scattering from hydrogen, since this diffraction is isotropic.

A variety of functions were tested for fitting smooth curves to the background data. The most successful procedure was to fit polynomial functions to the data by multiple linear regression analysis (Bevington, 1969).

$$y(x) = \sum_{i=0}^{l} a_i x^i \qquad (7)$$

where a_i is the ith polynomial coefficient. To avoid severe "ringing" in the fits, unweighted y values were regressed as the logarithm of the equatorial intensity, and x was the logarithm of the scattering angle 2θ. The use of log I and log (2θ) values in the polynomial fit was necessary because the intensities spanned almost four orders of magnitude. The degree of the power series, l, was selected which minimized χ^2, and ninth-order polynomials usually gave optimum fits. Minimum reduced-χ^2 values <0.03 were typical, and the fits to the equatorial data in Figure 17 are indeed excellent. The reproducibility of the background profiles at each D_2O concentration from different samples was also quite good.

(ii) Subtraction of Background

The scattering angle, 2θ, used in the polynomial fit was then converted to reciprocal space units, $s = 2 \sin \theta/\lambda$. The polynomial fit and the meridional Bragg diffraction were scaled to constant monitor counts and were normalized to constant beam flux by dividing by the intensity of the direct beam transmitted through the sample. The background-subtracted intensity, I(s), is then given by

$$I(s) = \frac{M(s)}{c_M b_M} - \frac{E(s)}{c_E b_E} \qquad (8)$$

where M(s) and E(s) are the meridional and equatorial intensities,

respectively. The c values are the total monitor counts collected with the sample in the meridional and equatorial orientations. The b values are the intensities at $2\theta = 0°$ of Gaussian peaks fitted to direct beam scans with the sample in the meridional and equatorial orientations. The b values did vary slightly because the retinas were mounted on parallel aluminum bars which were perpendicular and parallel to the scanning axis of the diffractometer in the meridional and equatorial geometries, respectively (Figure 6). The position of Gaussian peaks fitted to the direct beam scans was used to correct for a slight amount of angular backlash ($\sim$0.02°) in the scanning axis, and the continuous polynomial fit was used for background subtraction since the meridional data were not collected at exactly the same angular setting as the equatorial data. The value of E(s) was therefore given by equation (7). The data bars in Figure 19 show a backround-subtracted profile for an experiment in D_2O Ringer's solution.

(iii) Determination of Bragg Peak Areas and the Repeat Spacing

The algorithm for grid-search least-squares fit of Gaussian functions to the background-subtracted reflections can be described by considering three reflections. Peak height, angular position of the peak and the half-width of the reflections were specified initially by inspection of the background-subtracted data points. Since the diffracted intensity between reflections was not zero (Figure 19a), the contributions from nearest-neighbor reflections had to be considered in refining the parameters for reflection h. Three standard deviations of data around the peak maximum of reflection h were considered in the refinement. Nine parameters defined the initial fit to the profile, which was obtained by summation of the Gaussian peaks for reflections h - 1, h and h + 1

Figure 19. Background-subtracted neutron diffraction patterns for data collected in D_2O Ringer's solution. (a) The smooth curve through the data bars are the sums of Gaussian peaks fitted to the Bragg reflections. (b) Gaussian peaks were fitted to the background-subtracted reflections using an iterative grid-search algorithm. The horizontal lines indicate ± 1, ± 2 and ± 3 standard deviations for each Gaussian. The full widths at $e^{-\frac{1}{2}}$ height (± 1 standard deviation) increase in proceeding from lower to higher angle reflections.

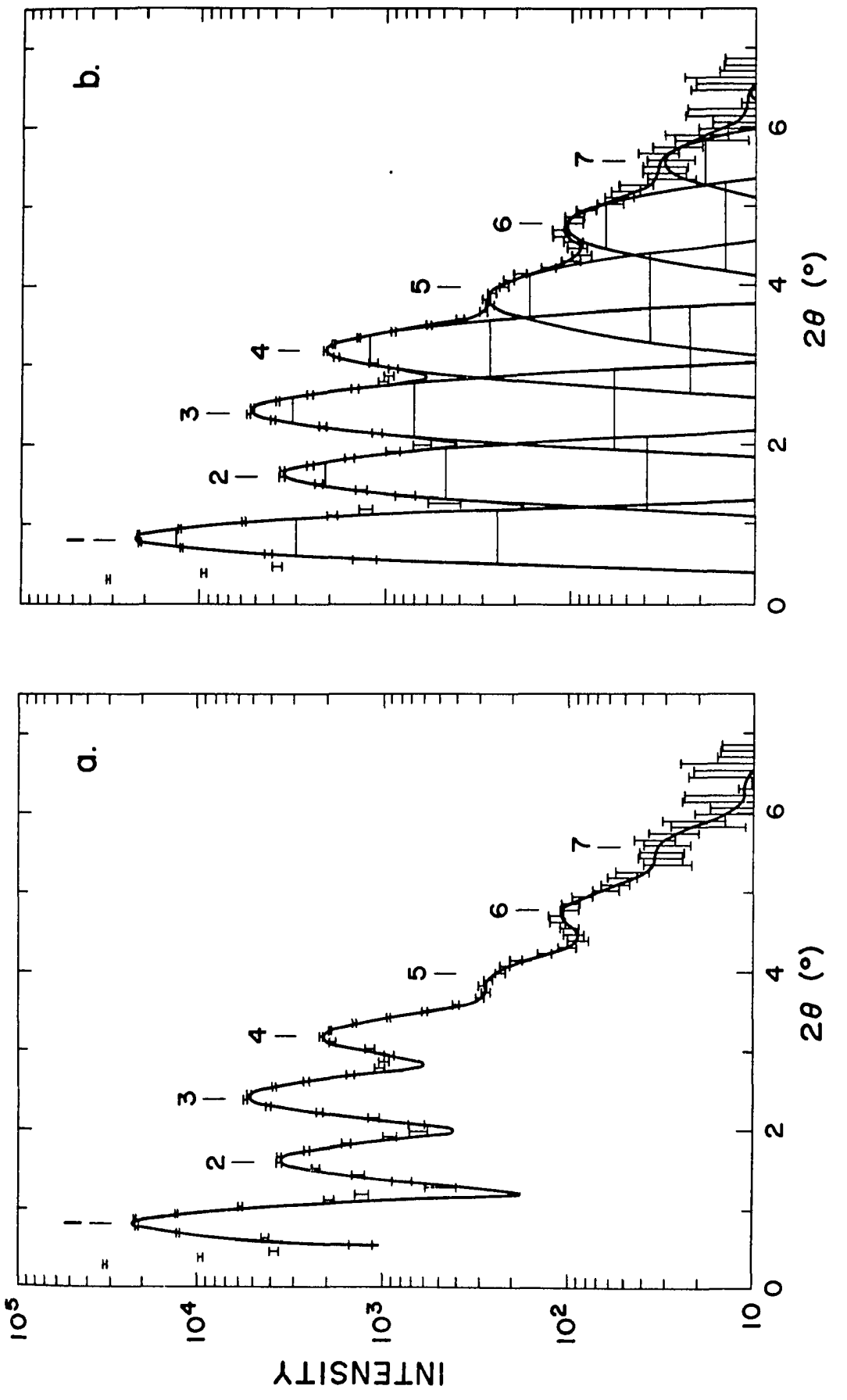

over the range of $\pm$ 3 standard deviations. A raw χ^2 was calculated between the experimental data and the sum of the three Gaussians in the region of $\pm$ three standard deviations around reflection h. The six parameters for reflections h - 1 and h + 1 were held constant while the three parameters for reflection h were successively refined. The refinement of each parameter for reflection h was continued until χ^2 changed by <0.1%. Then, the parameters for reflection h + 1 were refined with the parameters for reflections h and h + 2 kept constant. In this way all the reflections were refined by considering reflection triplets, except for the first and last orders. For the first reflection, only the overlap from the second order was considered in the refinement, and the fitting was begun at the minimum between the zero order and the first order. For the last reflection, n, only overlap from reflection n - 1 was considered, and the last point considered in the refinement was three standard deviations after the peak maximum of reflection n. One complete cycle of refinement was concluded when all reflection parameters had been refined. About five cycles were required to optimize the fit.

By using this curve fitting procedure the background-subtracted data could be described as the sum of the Gaussian reflections:

$$G(2\theta) = \sum_{h=1}^{n} A_h e^{-\frac{1}{2} z_h^2} \qquad (9)$$

where $G(2\theta)$ is the fit at angle 2θ, $z_h = (2\theta - B_h)/C_h$, and A_h, B_h and C_h are the maximum, position and half-width at $e^{-1/2}$ height for the Gaussian fit to reflection h. The progress of the refinement for all reflections was monitored by calculating χ^2 between the background-subtracted data given by equation 8 and the sum of the Gaussian reflections

given by equation 9. Refinement cycling was continued until χ^2 changed by <1%. The smooth curve in Figure 19a is the sum of the Gaussians described by equation 9; the agreement between the fitted curve and the data is quite good. Individual Gaussian peaks fitted to the background-subtracted data in Figure 19a are shown in Figure 19b. The full widths at $e^{-\frac{1}{2}}$ height for the Gaussians fitted to reflections 1 to 8 are 0.23, 0.31, 0.34, 0.36, 0.56, 0.56, 0.59 and 0.64 degrees, respectively. The full width at $e^{-\frac{1}{2}}$ height of the direct beam was 0.22°. The increase in reflection width in proceeding from lower to higher scattering angles is due to lattice disorder (variation in the spacing between discs) and the finite bandwidth of the neutron beam ($\Delta\lambda/\lambda$ = 0.025). After the Gaussian parameters were determined, the relative area of each reflection was simply obtained from the product, $A_h \cdot C_h$.

The error in the peak positions of the Gaussians was much greater for the higher orders than for the lower orders. Therefore, the repeat spacing, d, was calculated from the variance-weighted mean of the Gaussian positions:

$$d = \frac{\sum_{h=1}^{n} \frac{(h\lambda)/2 \cdot \sin(\frac{B_h}{2})}{\sigma_{B_h}^2}}{\sum_{h=1}^{n} \frac{1}{\sigma_{B_h}^2}} \qquad (10)$$

where $\sigma_{B_h}^2$ is the variance in the position of the Gaussian for reflection h. The positions for the Gaussians could have been grouped together as one parameter, the repeat spacing. However, the diffraction patterns were obtained using a step-scanning diffractometer, and so different reflections were not recorded simultaneously. The positions of the Gaussians

were threfore refined as separate parameters, and the reproducibility of the repeat spacing calculated from each reflection served as a convenient test of specimen integrity.

(iv) Error Analysis

Errors were propagated by assuming Poisson counting statistics in the observed meridional and equatorial data. Therefore, one standard deviation of the intensity observed at each scattering angle is given by the square root of the observed number of counts. The same error propagation procedure was used in treating the background, in fitting Gaussian functions to reflections and in determining the Lorentz and disorientation corrections [Chapter IV(e)]. According to standard procedures of error analysis described by Bevington (1969), σ_y, the standard deviation of a quantity y, is approximated by

$$\sigma_y^2 = \sigma_u^2 \left(\frac{\partial y}{\partial u}\right)^2 + \sigma_v^2 \left(\frac{\partial y}{\partial v}\right)^2 \qquad (11)$$

where u and v are the parameters of y. The assumption of equation (11) is that the fluctuations in the parameters, u and v, are uncorrelated. To obtain the variances of the parameters, σ_u^2 and σ_v^2, a function $y(x_i)$ is fitted to N data points (x_i, y_i). The goodness of fit is given by χ^2.

$$\chi^2 = \sum_{i=1}^{N} \left\{ \frac{1}{\sigma_i^2} \left[y_i - y(x_i)\right]^2 \right\} \qquad (12)$$

where σ_i is the standard deviation of the observed value y_i. The fitting procedure involves varying the values of the parameters of $y(x_i)$ to minimize the value of χ^2.

In fitting a Gaussian function to a reflection, a hypersurface is defined by the values of χ^2 as a function of the fitting parameters: the

maximum, the position and the half-width at $e^{-\frac{1}{2}}$ height of the Gaussian. In a grid-search least-squares fit, the three parameters describing the Gaussian are successively incremented until the minimum of the χ^2 hypersurface is located. Since the standard deviations of the data points, σ_i, were quite variable, the data were weighted by their variances in the least-squares fits. For fitting Gaussian functions to reflections, a parabolic interpolation of the χ^2 hypersurface was made, since there is no analytical form for the standard deviations of the parameters in nonlinear least-squares fits.

(v) Evaluation of Background-Subtraction and Fitting of Gaussian Peaks

A necessary condition for the success of the background subtraction and Gaussian fits is that the sum of the polynomial background (dotted profile in Figure 20) and the Gaussian peaks (Figure 19b) should be a good fit to the observed meridional diffraction. The good fit of the observed data to the smooth curve in Figure 20 suggests that the fitting procedure is reliable. Of a total of 39 independent experiments, 66% of the fitted data values fell within $\pm$ 1 standard deviation of the experimental values (total number of data points = 2683). Since this percentage is close to the theoretical value of 68%, the data processing procedure is statistically valid. The data analysis procedure was most useful in experiments where it would have been difficult to determine reflection intensities reliably and objectively by inspection. Although the data obtained in 30% D_2O are quite noisy (Figure 15), the pattern does contain information. The reflection intensities were objectively determined by using the data analysis procedure, and the propagated errors could be used to assess the precision of the intensities.

Figure 20. Neutron diffraction pattern from intact retinas equilibrated in D_2O Ringer's solution. The continuous curve is the sum of the polynomial regression fit to the background data (••••) and the Gaussian peaks (Figure 19b) fitted to the background-subtracted reflections. 60% of the fitted data values fall within ±1 standard deviation of the experimental values.

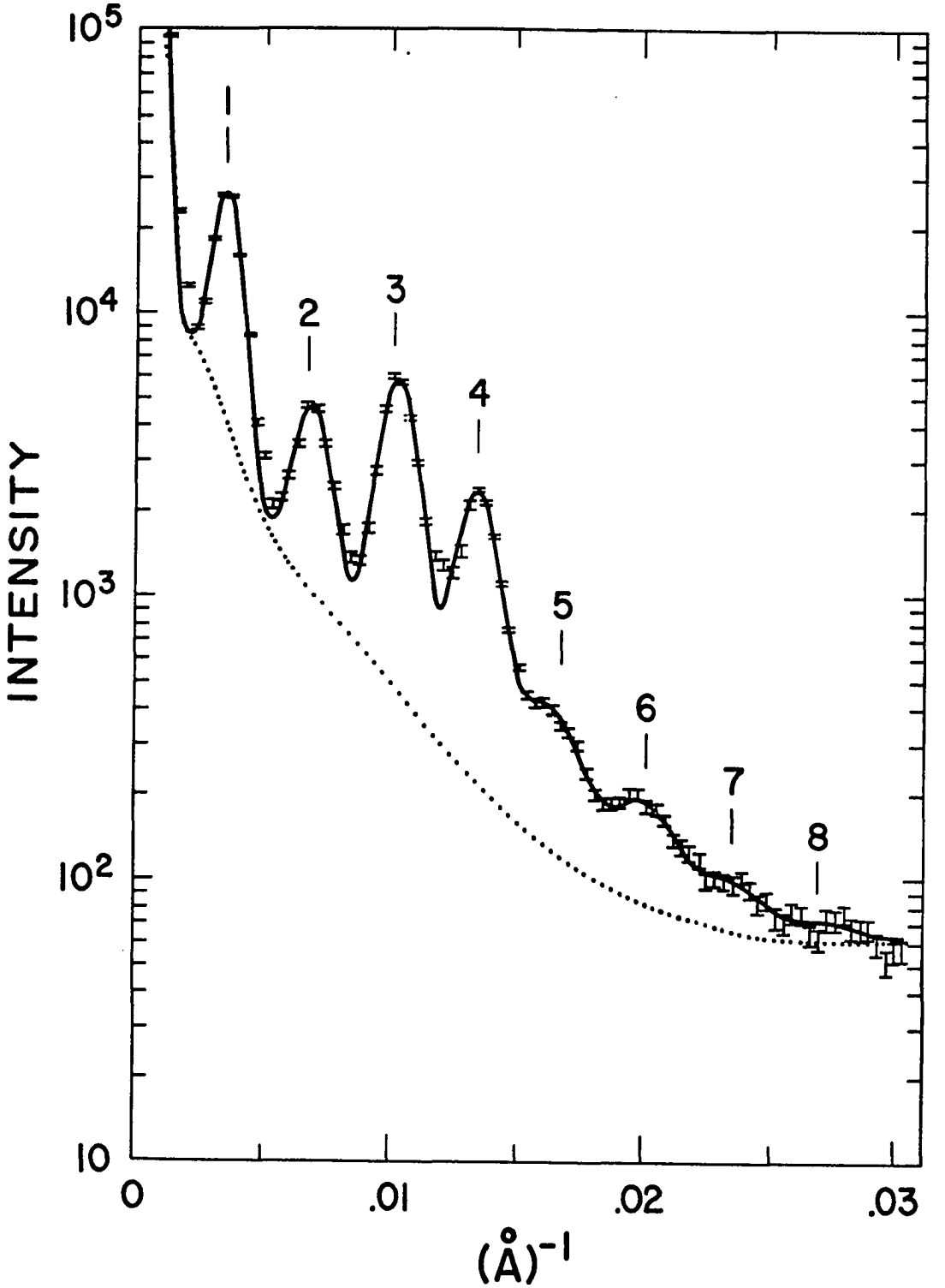

Procedures similar to those presented here have been used for analyzing diffraction data from other systems. The background scattering from x-ray diffraction of tobacco mosaic virus has been carefully examined and treated using semi-automated procedures (Barrett, Barrington Leigh, Holmes, Leverman, Mandelkow, von Sengbusch and Klug, 1971; Holmes, Stubbs, Mandelkow and Gallwitz, 1975). The consideration of overlap from nearest-neighbor reflections in fitting Gaussian peaks to smeared reflections was used for reducing x-ray diffraction patterns of DNA (Langridge, Wilson, Hooper, Wilkins and Hamilton, 1960). Worthington and McIntosh (1974) have presented the theoretical basis for the validity of this approach. The reader is referred to Diamond, (1969); Blessing, Coppens and Becker (1972); Ford (1974); Lehmann and Larsen (1974); Krieger, Chambers, Christoph, Stroud and Trus (1974) and Lehmann (1975) for methods used in single-crystal diffraction for treating background scattering and reflection profile fitting. Overlap of reflections is prevalent in low-angle studies because many of the structures examined are para-crystalline. If the overlap between reflections becomes too severe, either because of disorder in the structure or chromatic smearing, the Gaussians fitted to the data become increasingly less reliable because the diffraction approaches the continuous molecular transform rather than the sampled transform giving Bragg reflections.

(e) Determination of the Lorentz and Disorientation Corrections

The integrated intensity, I_{int}, of reflection h is given by (James, 1965; Warren, 1969; Arndt and Willis, 1966; Buerger, 1960)

$$I_{int}(h) = K\, L(h)\, P(h)\, |\vec{F}(h)|^2 \qquad (13)$$

where K is a proportionality constant and the polarization factor P equals

one at low angles and in neutron diffraction. The Lorentz factor, L, is a geometric correction which takes into account the fact that different reflections spend different amounts of time intersecting the Ewald sphere to satisfy the Bragg reflecting condition. In the rotating crystal method the rate of rotation of a zero-level equatorial reciprocal lattice point is inversely proportional to the reciprocal space distance between the origin in reciprocal space and the point of intersection of the reflection with the Ewald sphere. The reciprocal of the Lorentz factor, L^{-1}, in such an experiment is

$$L^{-1}(h) = \sin 2\theta \cong h \qquad (14)$$

and so L^{-1} is approximated by h at low angles. Therefore, the observed intensities must be multiplied by sin 2θ to make them proportional to the squares of the structure factors in equation (13).

Rotating crystal geometry is equivalent to that of fiber diffraction in which a parallel bundle of fibers is held stationary and the fibers have random rotational orientations about their long axes (James, 1965; Warren, 1969; Vainshtein, 1966). The reciprocal lattice points are spread out into circles with radii proportional to the distance between the fiber axis and the intersection of the reflection with the Ewald sphere. Since a greater fraction of the intensity is recorded for reflections at a smaller radius than for those at a greater radius, the Lorentz factor given by equation (14) will apply to the equatorial reflections on the zero layer line. A further disorientation correction D(h) is necessary if the fibers are not exactly parallel to one another but exhibit disorientation about the fiber axis (Franklin and Gosling, 1953; Arnott, 1965). Elegant treatments of the Lorentz and disorientation corrections in fiber diffraction have been published (Cella, Lee, and Hughes, 1970;

Deas, 1952; Holmes and Barrington Leigh, 1974; Stubbs, 1974).

Retinal rod outer segments have random rotational orientations about their long axes, and the discs are rotationally symmetric. The reciprocal Lorentz factor given by equation (14) will therefore apply to the meridional reflections from rods, and the structure factor amplitude $|\vec{F}(h)|$ is

$$|\vec{F}(h)| = \sqrt{h\ D(h)\ I(h)} \qquad (15)$$

where $L^{-1}(h) = h$ and $I(h)$ is the background-subtracted intensity of reflection h integrated over angle 2θ as described in Chapter IV (d). The disorientation correction $D(h)$ was determined by mapping the intensity distribution of the meridional reflections in reciprocal space. Three types of experiments were conducted: persistence-with-tilt experiments, slit-height reduction experiments, and rocking curve analysis.

Persistence-with tilt: Bear and Bolduan reported experiments in the early 1950's for assessing whether a diffracting sample is disoriented about its fiber axis (Bear and Bolduan, 1950; Bolduan and Bear, 1950; Bolduan and Bear, 1951). The sample is tilted with respect to the incident beam. If there is no disorientation, then the diffraction orders shift to higher angle, corresponding to an apparent decrease in repeat spacing. This method is designated the persistence-with tilt technique since samples with substantial disorientation about the fiber axis exhibit reflections whose intensities persist over appreciable tilts and are not shifted (Figure 21). A persistence-with-tilt experiment for the meridional diffraction observed from neutron scattering of retinas equilibrated in D_2O Ringer's solution is shown in Figure 22. The

Figure 21. The persistence-with-tilt experiment can be described by considering schematic diagrams of Bragg reflections from a sample of rods with random rotational orientations. Lines designated E intersect the Ewald plane which is perpendicular to the page. (a) The rods are exactly parallel so that the reflections have the shape of discs; in cross-section, these reflection discs are lines. The reflections observed with the sample perpendicular to the incident beam (0° tilt) shift to higher angles when the sample is tilted (dotted lines), giving an apparent decrease in the real space repeat spacing. (b) The rods are disoriented so that the reflections are spread out into caps of spheres; in cross-section, these reflection caps are arcs of circles with radii proportional to h. The reflections persist over appreciable tilt angles and are not shifted to higher angles; therefore, the repeat spacing does not change as the rods are tilted.

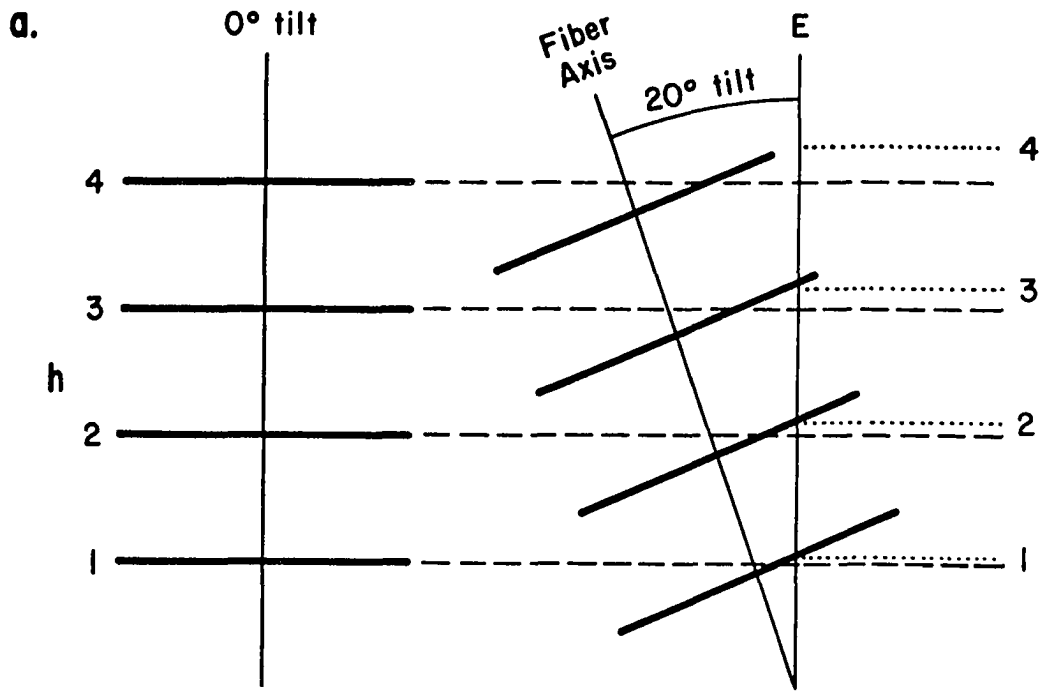

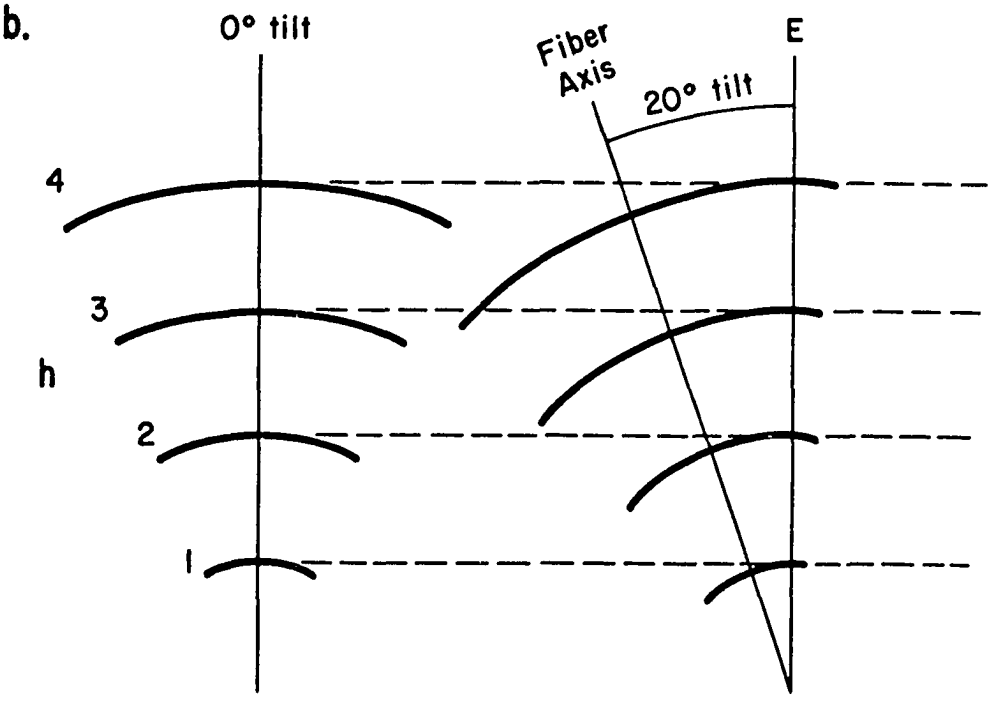

diffraction pattern was scanned in 2θ with the sample fixed at ω = 0° and then at ω = -20° (see Figures 6, 8 and 9). If the rods were completely parallel, the apparent repeat spacing at ω = -20° would be 295 Å · cos 20° = 277 Å. The repeat spacings at 0° tilt and 20° tilt were 295 ± 1 Å and 300 ± 5 Å. The constancy of the repeat spacing clearly indicates that the rods are not perfectly parallel. In fact, the disorientation of the rods must be comparable with the extent of tilting, 20°.

Slit-Height Reduction: To investigate the extent to which the detector Soller slits integrated the intensity distributed over the disorientation arcs of the reflections, the height of the Soller slits before the sample was reduced, and the diffraction pattern was scanned in 2θ with the sample kept fixed at ω=0°. If the slits are of infinite height compared to the height of the reflection arcs, then the relative intensities for each reflection should not change as the slit height is reduced. However, if the slits are of finite height compared with the height of the reflection arcs, then the relative intensities for each reflection will decrease with decreasing slit height. Such slit height reduction experiments (Yeager, 1975b) showed that a greater fraction of the total intensity was recorded for the lower order reflections compared with the higher order reflections. The Soller slits are therefore of finite height and partially integrate the disorientation arcs so that the disorientation correction varies with each reflection.

Rocking Curve Analysis: In order to calculate a disorientation correction for each reflection, the intensity distribution across the disorientation arcs was mapped by rocking curve analysis. The detector

Figure 22. Persistence-with-tilt experiment for neutron diffraction of intact retinas equilibrated in D_2O Ringer's solution. The dotted profiles are the polynomial fits to the background data, and the continuous curves through the observed data bars are the sums of the background fits and Gaussian peaks fitted to the background-subtracted reflections. The repeat spacings at 0° tilt and 20° tilt are 295 ± 1Å and 300 ± 5Å, respectively. The constancy of the repeat spacing indicates that there is substantial disorientation of the rods.

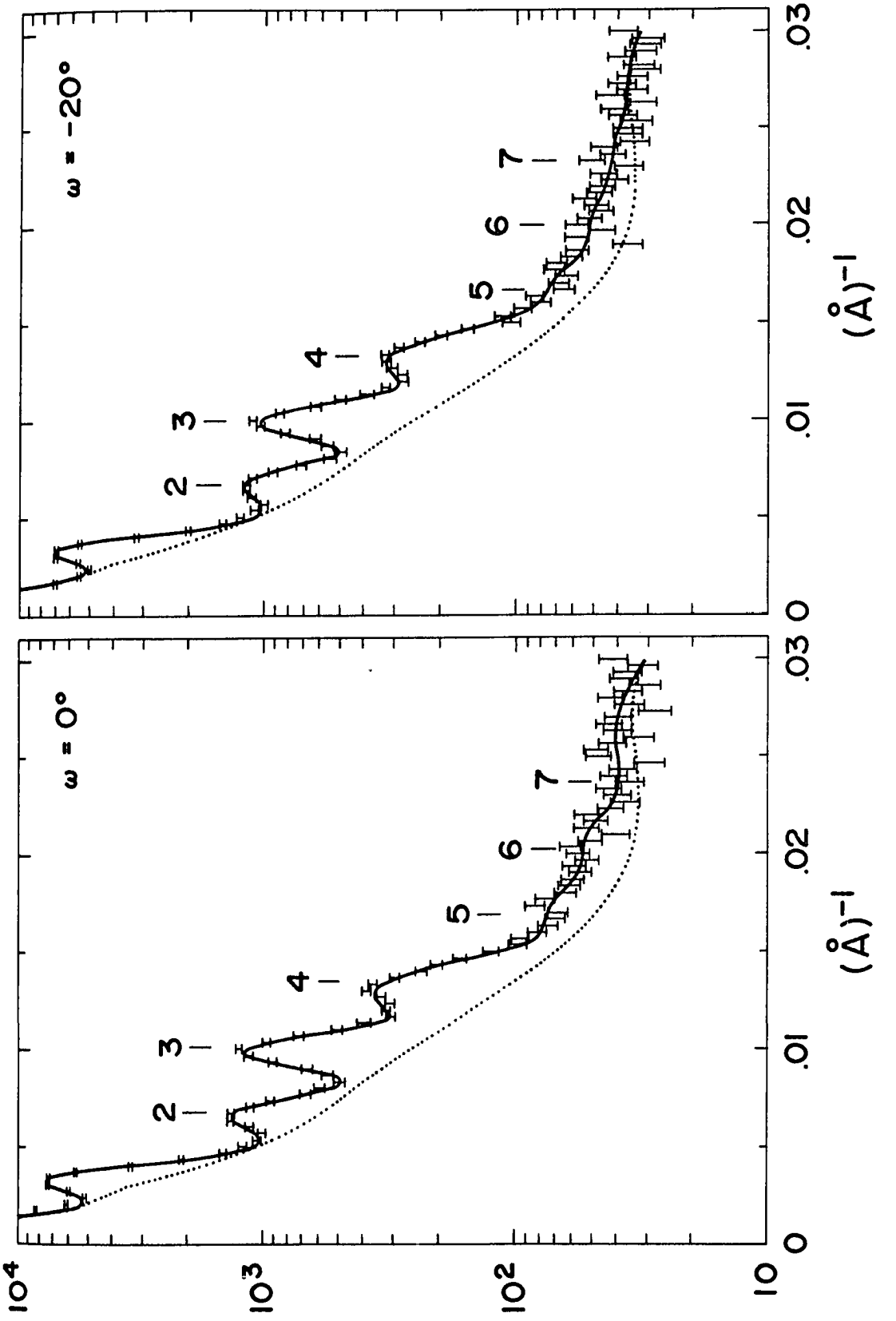

was fixed at a scattering angle 2θ corresponding to the peak maximum for a particular reflection, and the sample was rocked in angle ω. The rocking curves shown in Figure 23a were recorded with the sample oriented to observe both the meridional and equatorial diffraction (see Figures 6, 8 and 9). Since the equatorial scattering with the sample at $\chi = 90°$ would be expected to be spatially isotropic, the rocking curves should be horizontal lines. The equatorial rocking curves in Figure 23a are fitted quite well by lines and the profiles are almost horizontal. To correct for the decreased amount of material in the beam and the lower beam flux as ω increased, the scattering observed at each value of ω was normalized by using direct beam measurements through the sample with the detector at $2\theta = 0°$. The slight upward tailing of the equatorial profiles for reflections 1 and 2 in Figure 23a may indicate an incomplete correction for this effect. The equatorial rocking curves were considered as the background for the meridional rocking curves in Figure 23a. The background-subtracted rocking curves shown in Figure 23b are fitted quite well by Gaussian functions. The striking observations in these profiles are that the mosaic spreads for orders 1 to 4 are almost the same and are quite large. The mosaic spreads are defined by the full width at $e^{-\frac{1}{2}}$ height of the Gaussians ($\pm$ 1 standard deviation). These widths for orders 1 to 4 are $55.8\pm0.6°$, $55.0\pm1.8°$, $58.6\pm1.2°$ and $55.2\pm1.4°$ respectively.

The Gaussian rocking curves in Figure 23b certainly prove that the rods are disoriented in the plane which intersects the Ewald plane. The horizontal bright line in the photomicrograph of an edgefold preparation in Figure 11 shows that the rods have preferential alignment parallel to one another. The "patchy" birefringence in the plane of the

Figure 23. Rocking curves for the first four reflections from neutron diffraction of retinas in D_2O Ringer's solution with scattering angles of 0.8, 1.6, 2.4, and 3.2 degrees, and scale factors of 5.0×10^{-4}, 2.5×10^{-3}, 2.86×10^{-3}, and 8.33×10^{-3}, respectively. Lines were fitted to rocking curves with the sample aligned to observe the equatorial scattering at $\chi = 90°$. (a) The curves drawn through the data recorded with the sample aligned to observe the Bragg diffraction at $\chi = 0°$ are the sums of the linear equatorial rocking curves and Gaussian peaks fitted to the background-subtracted meridional rocking curves. (b) Background-subtracted rocking curves for the first four reflections from neutron diffraction of retinas in D_2O Ringer's solution with scale factors of 6.67×10^{-4}, 5.0×10^{-3}, 3.33×10^{-3}, and 1.25×10^{-3}, respectively. The data bars display the rocking curves after subtraction of the equatorial rocking curves in (a). The full width at $e^{-\frac{1}{2}}$ height of the Gaussian profiles fitted to the data defines the mosaic spread η. The mosaic spreads for reflections 1 to 4 are $55.8 \pm 0.6°$, $55.0 \pm 1.8°$, $58.6 \pm 1.2°$, and $55.2 \pm 1.4°$, respectively.

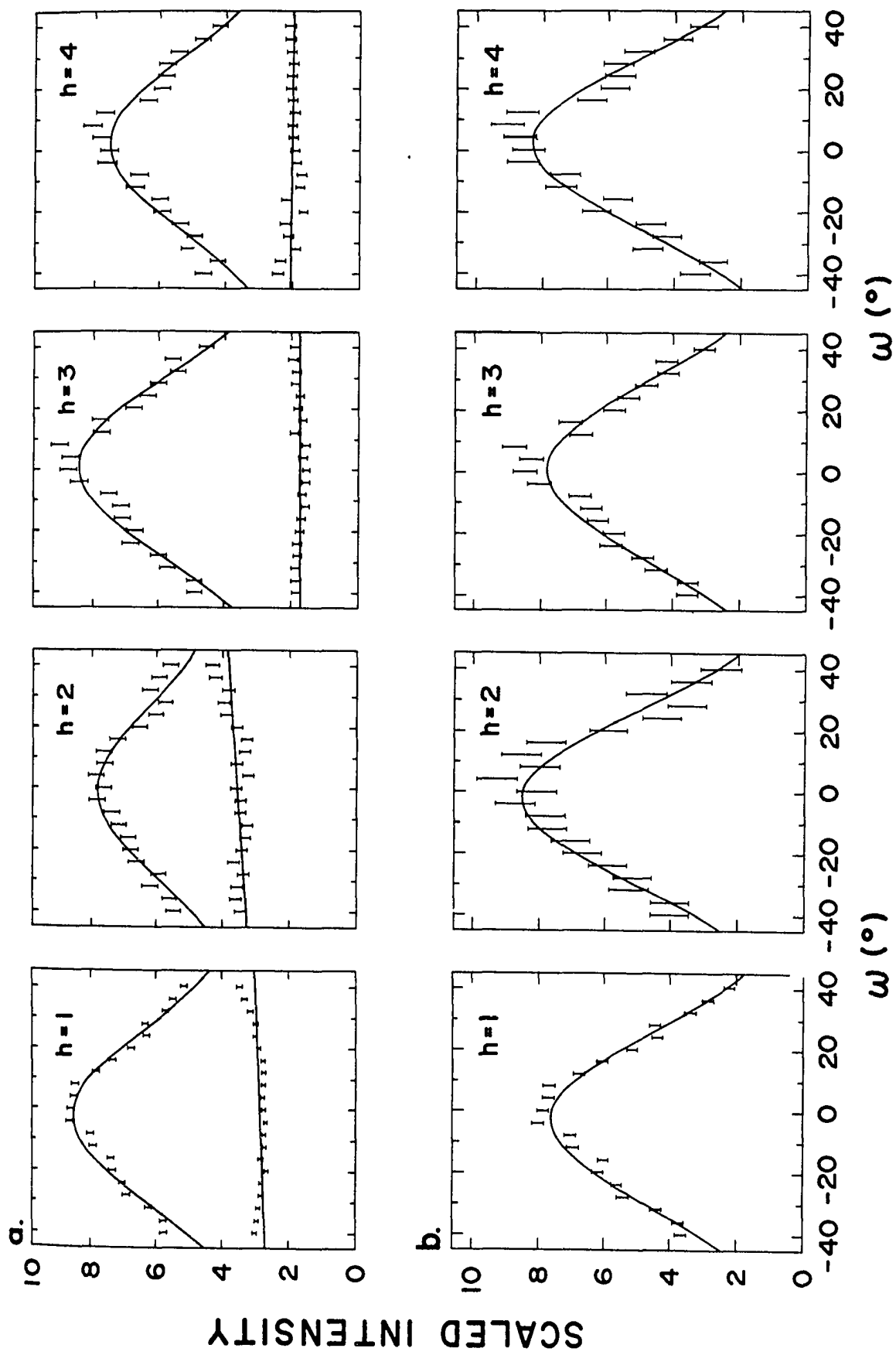

retina indicates that disorientation of the rods about their long axes is indeed present and that the disorientation does not occur along a particular axis of the plane of the retina. Thus, the rods are disoriented in a roughly rotationally symmetrical fashion so that the reflections in reciprocal space, as depicted in Figure 9, should be approximately circular in a cross section perpendicular to the Ewald plane.

Since the meridional reflections have been characterized, the disorientation correction D(h) for each reflection can now be calculated. D(h) is the reciprocal of the fraction of the intensity of reflection h accepted by the Soller slit aperture closest to the graphite monochromator. D(h) will increase with increasing h since a smaller fraction of the intensity of the higher orders will be recorded compared with the lower orders. To calculate D(h), the sample was considered to be made up of a one dimensional vertical array of mosaic blocks over the sample height. The diffracted rays from a single mosaic block are smeared vertically due to the mosaic spread η. (Since the vertical beam divergence was $\sim 1°$ and $\eta \sim 60°$, the additional smearing due to beam divergence is negligible.) For a single mosaic block the vertical height of the smeared reflection in the plane of the Soller slit aperture is $2\theta \cdot \eta \cdot L$ where L is the horizontal distance from the sample to the aperture. The total intensity in the vertical direction of reflection h was obtained by numerical integration over all mosaic blocks assuming the slit to be of infinite height. D(h) was then given by the ratio of this total intensity to the integrated intensity with finite limits given by the slit height. Using the values L = 36.8 cm., sample height = 19mm, slit height = 19mm, λ = 4.19 Å and d = 300 Å, the values of D(h) for orders 1 to 8 were 1.2, 1.5, 2.0, 2.7, 3.4, 4.1, and 5.4, respectively.

Thus, the percentage of the vertical intensity that was recorded for orders 1 to 8 was 83, 66, 49, 37, 30, 25, 21, and 18%, respectively.

A preliminary analysis of diffraction patterns recorded using the 2-dimensional position-sensitive detector (Figure 10d), in which the total vertical intensity of the reflections is recorded, confirmed the above treatment of the Soller slit diffraction patterns. The above treatment of the Lorentz and disorientation corrections was justified because the mosaic spread was the dominant influence on the recorded intensity; η was substantially larger than the beam divergence, the chromatic bandwidth of the neutron beam and the mosaic spread of the graphite monochromator. Saxena and Schoenborn (1977) have demonstrated the validity of using the above approach for obtaining the disorientation correction.

(f) Structure Factor Amplitudes and the Effect of Light

Table I lists the structure factor amplitudes for the experiments in different D_2O-H_2O mixtures shown in Figure 15, and Table II lists the structure factor amplitudes for the experiments in D_2O Ringer's solution of varying osmolarity shown in Figure 12.

Since the diffraction patterns were normalized to constant beam flux and monitor counts, the structure factors should be on an absolute scale. (However, the units of the absolute scale are arbitrary.) The range of amplitudes from different experiments at the same D_2O concentration deviated by more than the statistical error for an individual experiment (Figure 24); therefore the number of diffracting rods in the beam probably varied. However, since the variation of the amplitudes between experiments at the same D_2O concentration was less by about a factor of 5 than the changes observed as the D_2O concentration was changed, an absolute comparison of the amplitudes between experiments is justified. The plots

Table 1

STRUCTURE FACTOR AMPLITUDES

FROM NEUTRON DIFFRACTION OF INTACT RETINAS

IN DIFFERENT MIXTURES OF D_2O AND H_2O

	% D_2O				
h	100	80	60	40	30
1	185 ± 2	130 ± 2	84 ± 1	43 ± 2	21 ± 3
2	128 ± 3	86 ± 4	50 ± 3	24 ± 4	18 ± 4
3	234 ± 3	170 ± 3	114 ± 3	58 ± 3	47 ± 5
4	225 ± 3	152 ± 3	97 ± 4	58 ± 6	38 ± 6

The structure factors were calculated from equation (15). The errors are one standard deviation obtained by propagation of statistical errors through background-subtraction and fitting of Gaussian reflections to the Bragg peaks.

Table 2

STRUCTURE FACTOR AMPLITUDES

FROM NEUTRON DIFFRACTION OF INTACT RETINAS

IN D_2O RINGER'S SOLUTION OF VARYING OSMOLARITY

	RINGER's SOLUTION			
h	2% sucrose	isotonic	0.8 dilute	0.6 dilute
1	319 ± 2	333 ± 2	315 ± 2	221 ± 3
2	231 ± 2	254 ± 2	210 ± 3	165 ± 5
3	382 ± 4	441 ± 3	397 ± 4	284 ± 3
4	328 ± 3	378 ± 3	316 ± 3	237 ± 5
d(Å)	294	298	308	328

The structure factors were calculated as in Table 1.

Figure 24. Structure factor amplitudes F(h) for reflections 1, 2, 3, and 4 increase linearly as the D_2O concentration is increased.

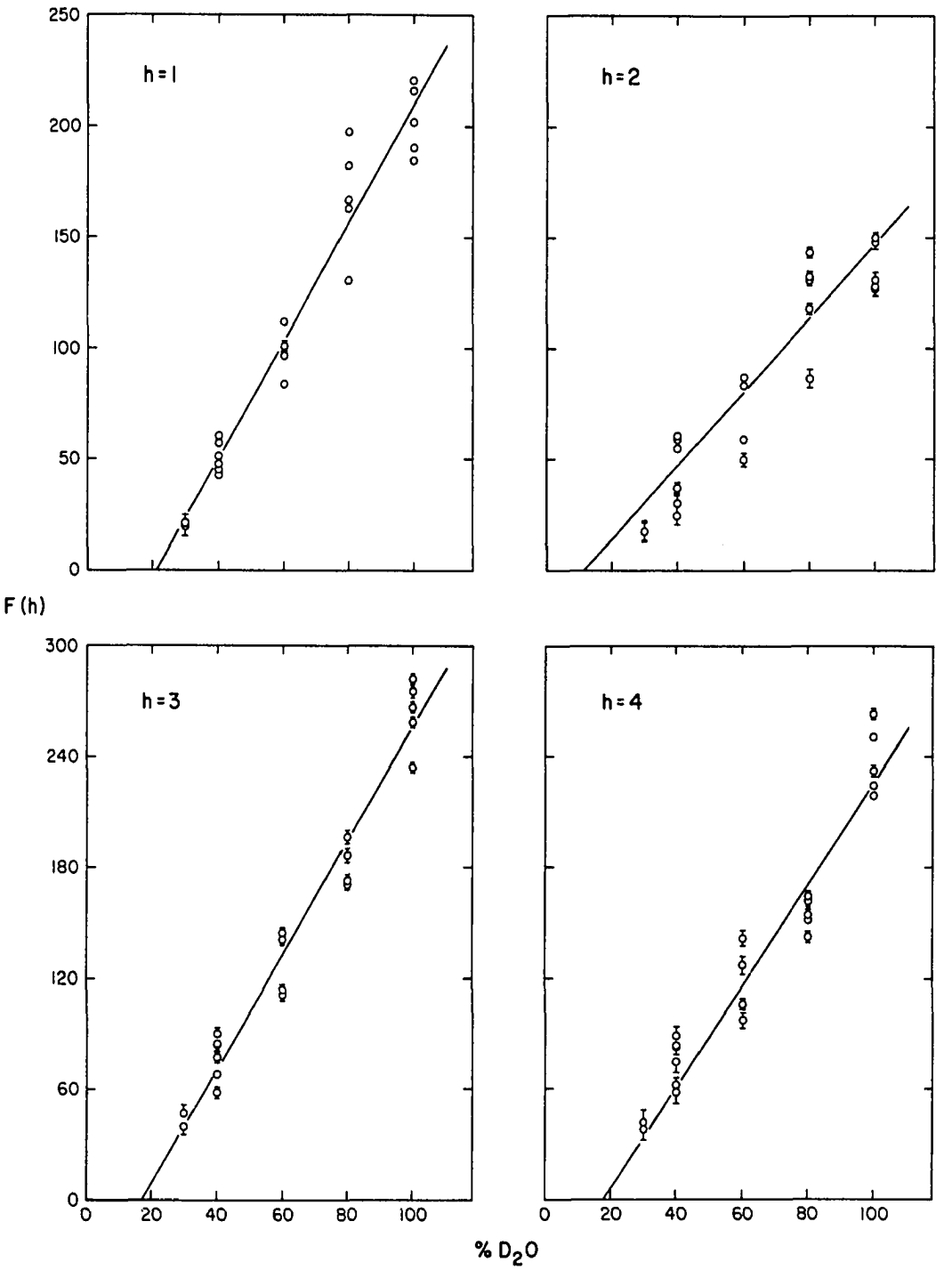

of F(h) versus percent D_2O in Figure 24 show that F(h) depends linearly on percent D_2O, as expected for a hydrated structure (Bragg and Perutz, 1952; Zaccai, Blasie, and Schoenborn, 1975; Worcester and Franks, 1976). The linear correlation coefficients for the variance-weighted least-squares fits in Figure 24 were 0.96, 0.92, 0.93, and 0.96 for orders one to four respectively.

Structure factors obtained from neutron diffraction of dark-adapted and bleached retinas are shown in Figure 25. To correct for the variation in the number of diffracting rods in different samples, data sets were scaled to one another by normalizing to the sum of the corrected intensities for the first 8 reflections, $\frac{1}{d} \sum_{h=1}^{8} F(h)^2$. Since the light-dependent changes are within the experimental reproducibility of 10%, only small structural changes in the disc membrane occur upon bleaching at 40 Å resolution.

Figure 25. Structure factor amplitudes F(h) from neutron diffraction of dark-adapted (O) and bleached (Δ) retinas equilibrated in D_2O Ringer's solution.

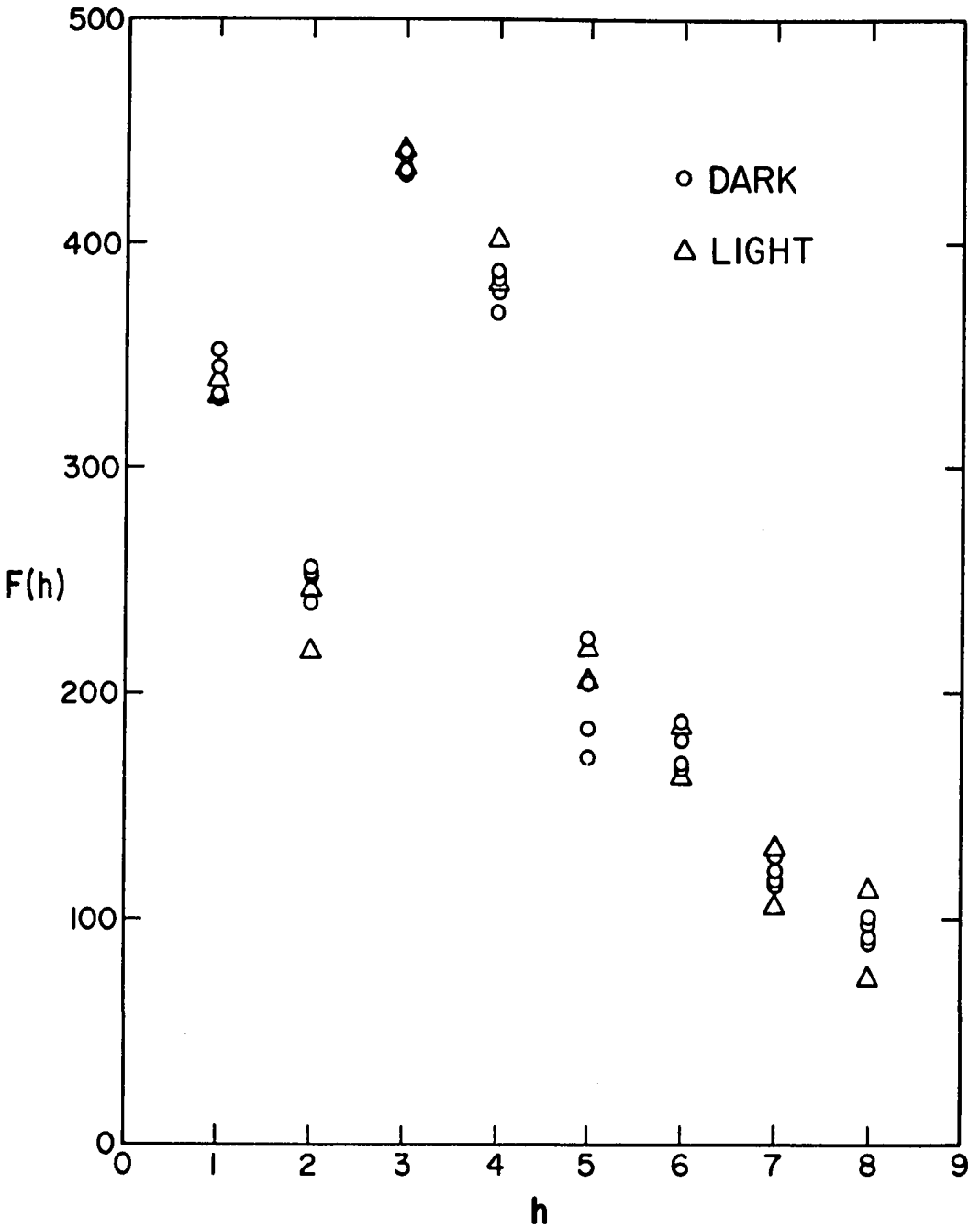

CHAPTER V

STRUCTURAL ANALYSIS

The intensities, phases, and disorientation corrections are considerably more reliable for the first four orders than for the higher orders. The structural analysis described below will therefore consider only the first four strong reflections.

(a) Patterson Maps

One dimensional Patterson maps were calculated by Fourier transformation of the corrected intensities

$$P(x) = \frac{2}{d} \sum_{h=1}^{n} h\, D(h)\, I(h) \cos\left(\frac{2\pi h x}{d}\right) \qquad (16)$$

where P(x) is the value of the Patterson function at a real space distance x and n=4.

Patterson maps calculated on an absolute scale with arbitrary units for experiments in different D_2O-H_2O mixtures (Figure 26) display broad peaks centered at about 84 Å with magnitudes of about 60% of the origin peaks. The movement of the 84 Å correlation to larger distances as the D_2O concentration decreases was not observed in all experiments and may not be significant. As the D_2O concentration of the Ringer's solution decreased, the reproducible characteristics of the Patterson maps were a reduction in the magnitude of the origin peak and the 84 Å correlation. This behavior is consistent with a reduction in the contrast within the unit cell as the D_2O concentration decreases and is also suggested by the reduced coherent intensity of the reflections as the H_2O content of

Figure 26. Patterson maps calculated on an absolute scale from the corrected intensities of the first four reflections for neutron diffraction experiments on intact retinas equilibrated in 100 (———), 80 (·····), 60 (------), and 40% (-·- ·- ·) D_2O Ringer's solution.

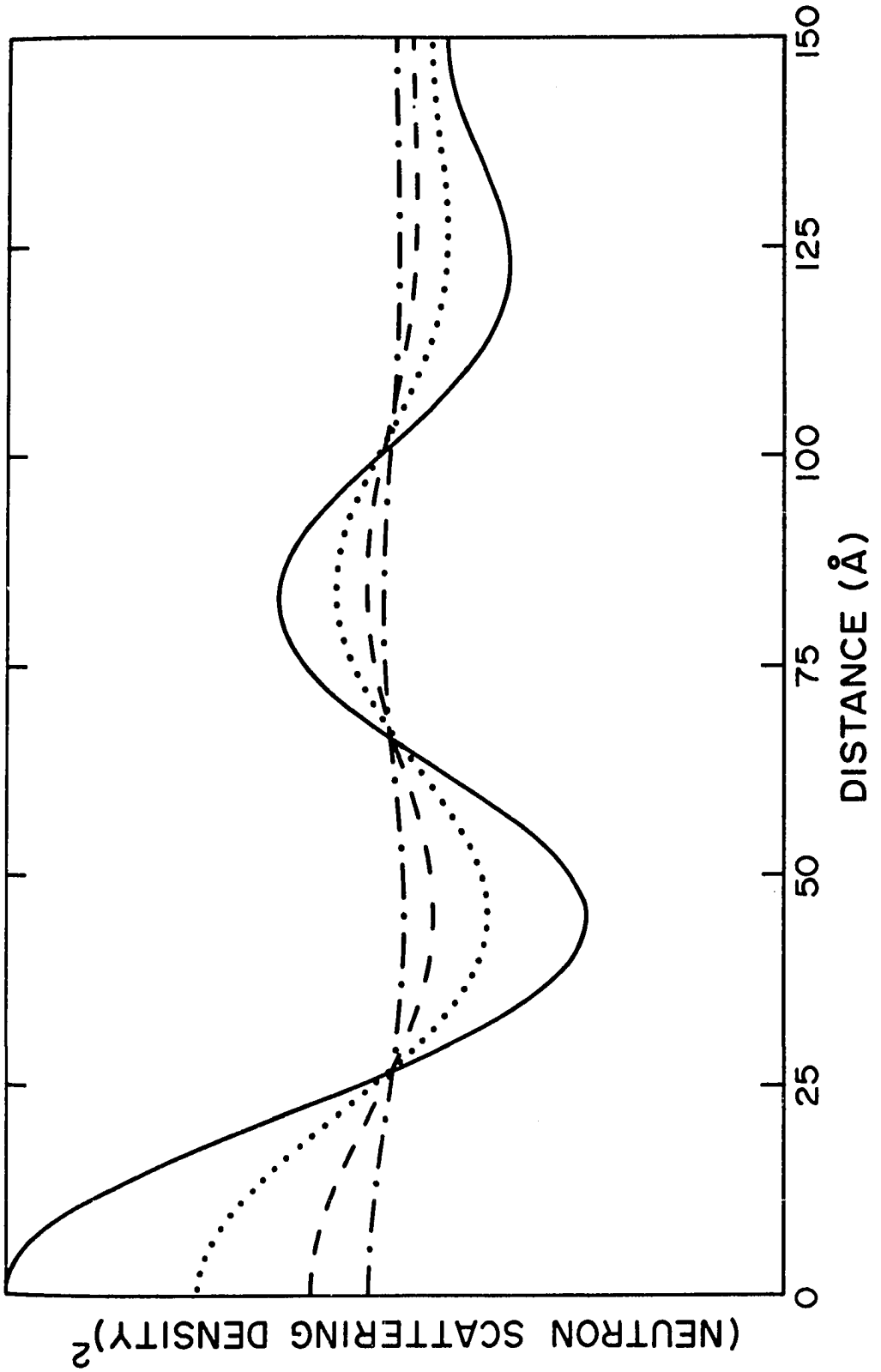

the Ringer's solution increased (Figure 16). The general modulations of the Patterson maps at all D_2O concentrations are qualitatively the same, which suggests that at 75 Å resolution the principal effect of changing the D_2O concentration from 100% to 30% is to alter the scattering density of the aqueous regions without changing the internal contrast of the disc membrane.

Patterson maps calculated from the intensities from experiments in D_2O Ringer's solution with varying osmolarity (Figure 27) also display a broad correlation which moves from 83 Å in 2% sucrose Ringer's solution to 93 Å in 0.6 diluted Ringer's solution. The vectors at distances < 30 Å should be dominated by intramembrane correlations (Caspar and Kirschner, 1971). The similarity of the Patterson maps at distances < 30 Å suggests that the structure of the membrane is not changed as the tonicity is varied.

(b) Phase Determination

Electron microscope images of disc membranes display mirror planes in the middle of the intradisc and extradisc regions (Figure 2). For a centrosymmetric crystal the structure factors are real, and the phase problem reduces to assigning a + or - sign to the square root of the corrected intensities. Kinetic experiments were conducted to determine whether phase changes occurred as the D_2O concentration was varied. Retinas were equilibrated in 40% D_2O, and then 100% D_2O Ringer's solution was kept flowing through the specimen cell while the first four reflections were repetitively scanned. The intensity of the reflections increased without passing through zero as the D_2O concentration changed from 40% to 100%. Therefore, the phases of the first four reflections remained the same over this range of D_2O

Figure 27. Patterson maps calculated from the first four reflections for neutron diffraction experiments on intact retinas equilibrated in D_2O Ringer's solution of varying osmolarity. The broad correlation at 83 Å shifts to longer distances as the osmolarity decreases. The profiles for all experiments have been normalized to the magnitude of their origin peaks.

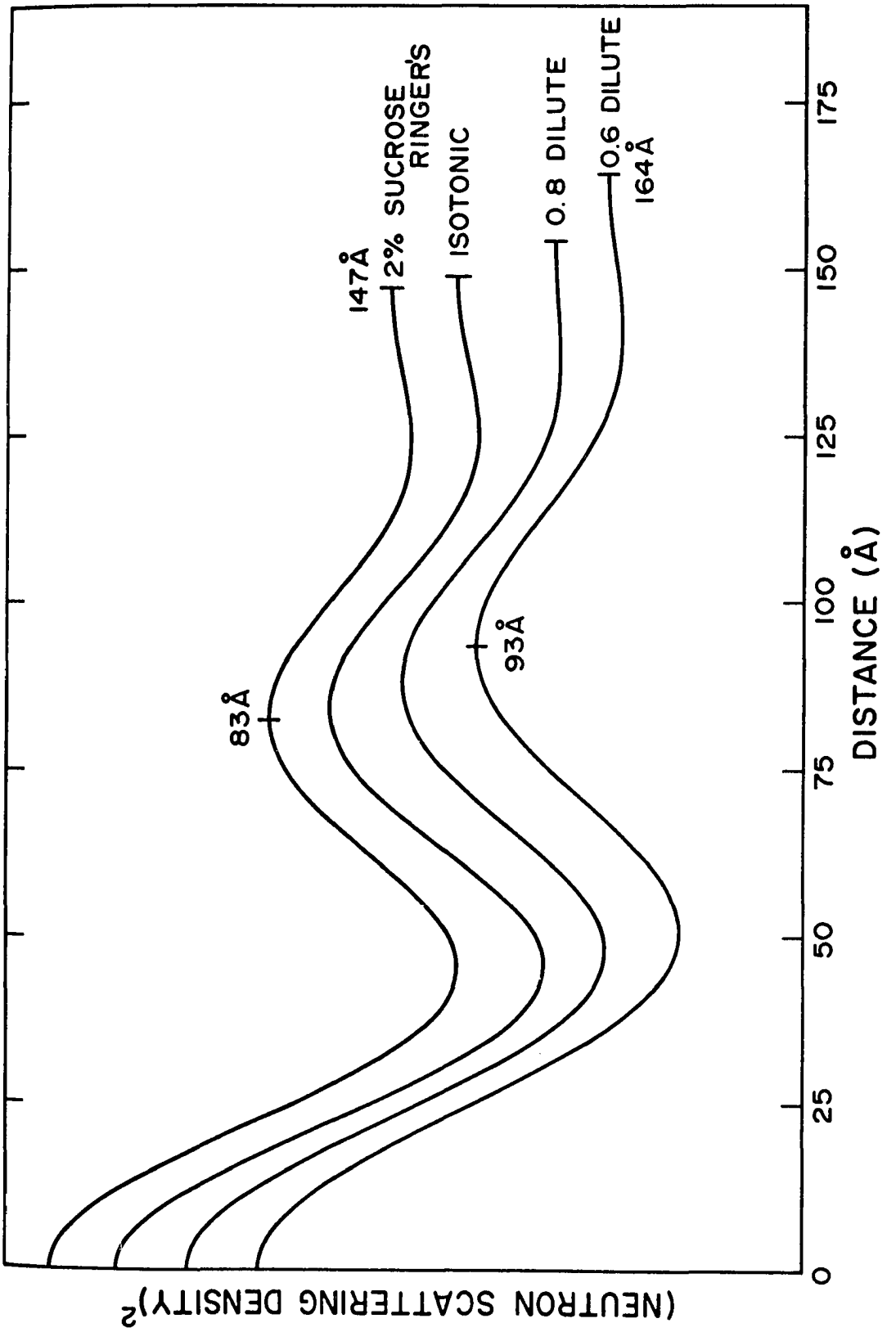

concentration. This conclusion is also supported by plots of the structure factor moduli versus percent D_2O (Figure 24). These plots are linear and phase changes for the first four orders do not occur until the D_2O concentration is < 30%.

The phases for the first four orders were determined by analyzing the models shown in Figure 28, which are interpretations of the Patterson maps in Figures 26 and 27. It should be stressed that Patterson maps do not uniquely define the structure and hence the phases. However, the D_2O-H_2O and osmotic Patterson maps do provide several pieces of independent evidence that favor model a in Figure 28.

The broad correlation at 84 Å in Figure 26 is interpreted as arising from correlations between two regions of density spaced 88 Å apart. This interpretation is compatible with electron microscope images of rod outer segment disc membranes which show two densely stained regions in the unit cell. The models in Figure 28 predict a Patterson map with a broad correlation at 84 Å in isotonic D_2O Ringer's solution at 75 Å resolution. The differences between the models are whether the regions of density 88 Å apart are nonaqueous troughs relative to the aqueous regions (model a); aqueous peaks relative to the nonaqueous regions (model b); nonaqueous peaks relative to the aqueous regions (model c); or aqueous troughs relative to the nonaqueous regions (model d).

The D_2O-H_2O Patterson maps in Figure 26 show that the contrast within the structure decreases as the D_2O concentration decreases. At 75 Å resolution, this decreased contrast is due to the decreased scattering density in the aqueous regions of the structure and not due to contrast fluctuations within the membrane interior. This conclusion is supported by two observations: (1) the Patterson maps for D_2O concentrations

Figure 28. Models for the interpretation of Patterson maps in Figures 26 and 27. Two 50 Å regions of density with a center-to-center separation of 88 Å are placed centrosymmetrically in a 300 Å unit cell. The bars at the top of the figure designate aqueous (stippled) and nonaqueous (solid) regions. The contrast between the aqueous and nonaqueous regions is designated by C. In models (a) and (b), the contrast decreases and in models (c) and (d), the contrast increases in proceeding from 100% D_2O (———) to 60% D_2O (----). The unit cell spacing and the distance between the troughs increase as the osmolarity of the Ringer's solution decreases (••••). The models are scaled so that the contrast is the same in 100% D_2O, and the neutron scattering density of the aqueous regions decreases in going from 100% to 60% D_2O.

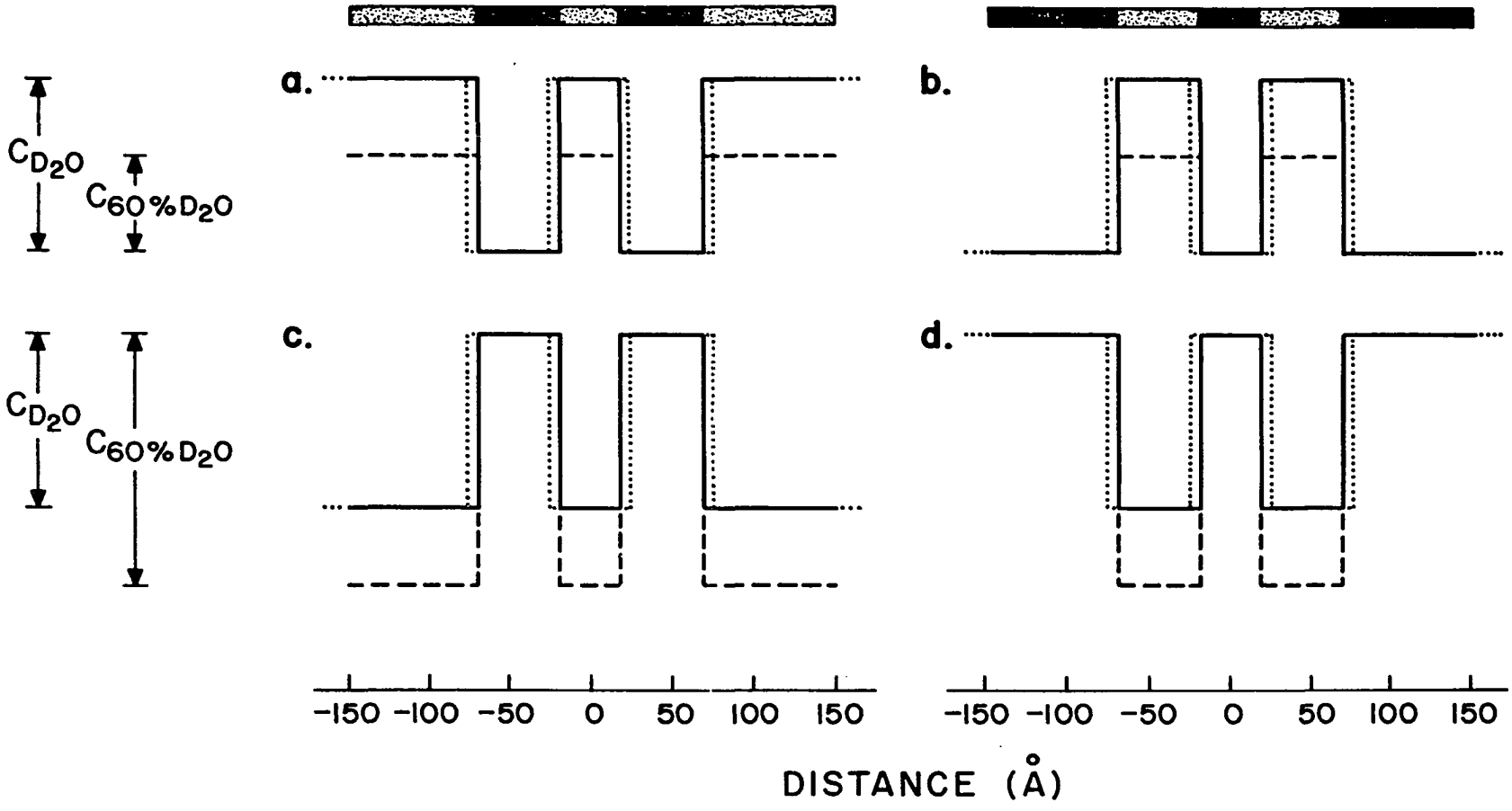

ranging from 100% to 30% have the same modulations and (2) difference Patterson maps using $(F_{D1}-F_{D2})^2$ as coefficients in equation (16), where D1 and D2 are different D_2O concentrations, are identical in shape to the Patterson maps in Figure 26. These difference maps display the correlations between aqueous regions within the structure (Zaccai, Blasie, and Schoenborn, 1975) and suggest that the distribution of water is the same in 100% and 30% D_2O since the difference maps are the same over this range of D_2O concentration. Models c and d in Figure 28 predict that the contrast within the structure increases as the D_2O concentration decreases from 100% (continuous line) to 60% D_2O (dashed line) and are therefore incompatible with the observed Patterson maps. Models c and d are also unlikely since the scattering density of D_2O is less than the density of the nonaqueous regions, in conflict with the calculated scattering densities of membrane molecules in Figure 4.

The shift of the 83 Å correlation to 93 Å and the increase in the unit cell repeat spacing (Figure 27) are interpreted in the models of Figure 28 as a separation of the regions 83 Å apart with decreasing osmolarity (dotted lines). Since the 83 Å peak shows little or no increase in width as it shifts to longer distances, the widths of the regions 83 Å apart remain constant as the regions separate. In models b and d the behavior of the osmotic Patterson maps is explained by the increases in the dimensions of the nonaqueous regions, whereas in models a and c the aqueous regions increase in size with decreasing osmolarity. Due to the low solubility of water in lipid hydrocarbon, the increased water content within the structure with decreasing osmolarity is unlikely to be due to infusion of water into the lipid hydrocarbon regions. The most chemically plausible explanation of the increased water content

within the unit cell is that the additional water is added to pre-existing water compartments. Such water addition in models b and d would cause an increased unit cell repeat spacing but would not cause the observed shift from 83 Å to 93 Å. Instead, the 83 Å peak would increase in width but would not shift position.

Model a is compatible with the observed D_2O-H_2O Patterson maps and also provides a chemically plausible explanation for the osmotic Patterson maps. The neutron scattering density of the aqueous regions and the contrast between the aqueous and nonaqueous regions decrease with decreasing D_2O concentration. The water content of the aqueous regions increases with decreasing osmolarity of the Ringer's solution, causing an increase in unit cell size. The aqueous region between the troughs increases in size with decreasing osmolarity, causing the observed shift from 83 Å to 93 Å in the osmotic Patterson maps. Since the solubility of water in hydrocarbon is low, the scattering density of the nonaqueous regions are independent of D_2O concentration. Note that model a is essentially equivalent to the neutron scattering density profile of the lipid bilayer model for the disc membrane shown in Figure 5. The broad Patterson peak at 84 Å would represent the separation of centers of the disc membrane pairs.

Fourier transformation of model a using equation (4) gives the phases -,+,+,+ for the first four orders for the osmotic experiments in D_2O Ringer's solution. Knowing that there are no phase changes between 100% and 30% D_2O, the phases for the reflections at each D_2O concentration are also -,+,+,+. It should be noted that of all the possible phase combinations, only the phases -,+,+,+ yield Fourier syntheses in D_2O which can be interpreted as having two membranes in the unit cell with

a higher neutron scattering density in the aqueous regions compared with the membranes.

(c) Neutron Scattering Density Profiles

One dimensional neutron scattering density profiles were calculated from

$$\rho(x) = \frac{2}{d} \sum_{h=1}^{n} s(h)\, F(h) \cos\left(\frac{2\pi h x}{d}\right) \qquad (17)$$

where $\rho(x)$ is the neutron scattering density at a real space distance x, and s(h) is the phase of reflection h. Centers of symmetry are located at $x = \frac{j}{2}$ where j is an integer.

Neutron scattering density profiles for experiments in different mixtures of D_2O and H_2O were calculated on an absolute scale to 75 Å resolution. The Fourier maps in Figure 29 show that as the D_2O concentration decreases the overall contrast between the low density troughs at ± 44 Å and the remainder of the structure diminishes. The highest density at all D_2O concentrations is at the origin. The profiles also display shoulders at ± 115 Å with a density intermediate between that at the origin and the troughs.

The structure factors in different D_2O-H_2O mixtures are on an absolute scale, but the units of the scale are arbitrary since the zero order was not measured and the number of discs comprising the coherent scattering unit is not known. However, the units of the absolute scale can be estimated by assuming that the highest point in the neutron scattering density profile in D_2O Ringer's solution (at 0Å) has the density of D_2O Ringer's solution (6.35×10^{-14} cm/Å^3). This assumption is reasonable since D_2O has a scattering density larger than membrane molecules (Figure 4). The scattering densities at the origin in the Fourier syntheses for the experiments in different mixtures of D_2O and

Figure 29. Neutron scattering density profiles calculated from the first four orders of diffraction from intact retinas equilibrated in isotonic Ringer's solution containing different mixtures of D_2O and H_2O. The Fourier syntheses from top to bottom are experiments in 100, 80, 60, 40, and 30% D_2O. The absolute neutron scattering density scale was assigned by assuming that (1) the highest scattering density in the Fourier synthesis in 100% D_2O Ringer's solution (at 0 Å) has the neutron scattering density of 100% D_2O Ringer's solution, (2) structures in different D_2O-H_2O mixtures are isomorphous, (3) series termination errors are small, and (4) the neutron scattering density at ± 44 Å, obtained by extrapolation of the contrast at ± 44 Å to zero in Figure 30, is independent of D_2O concentration.

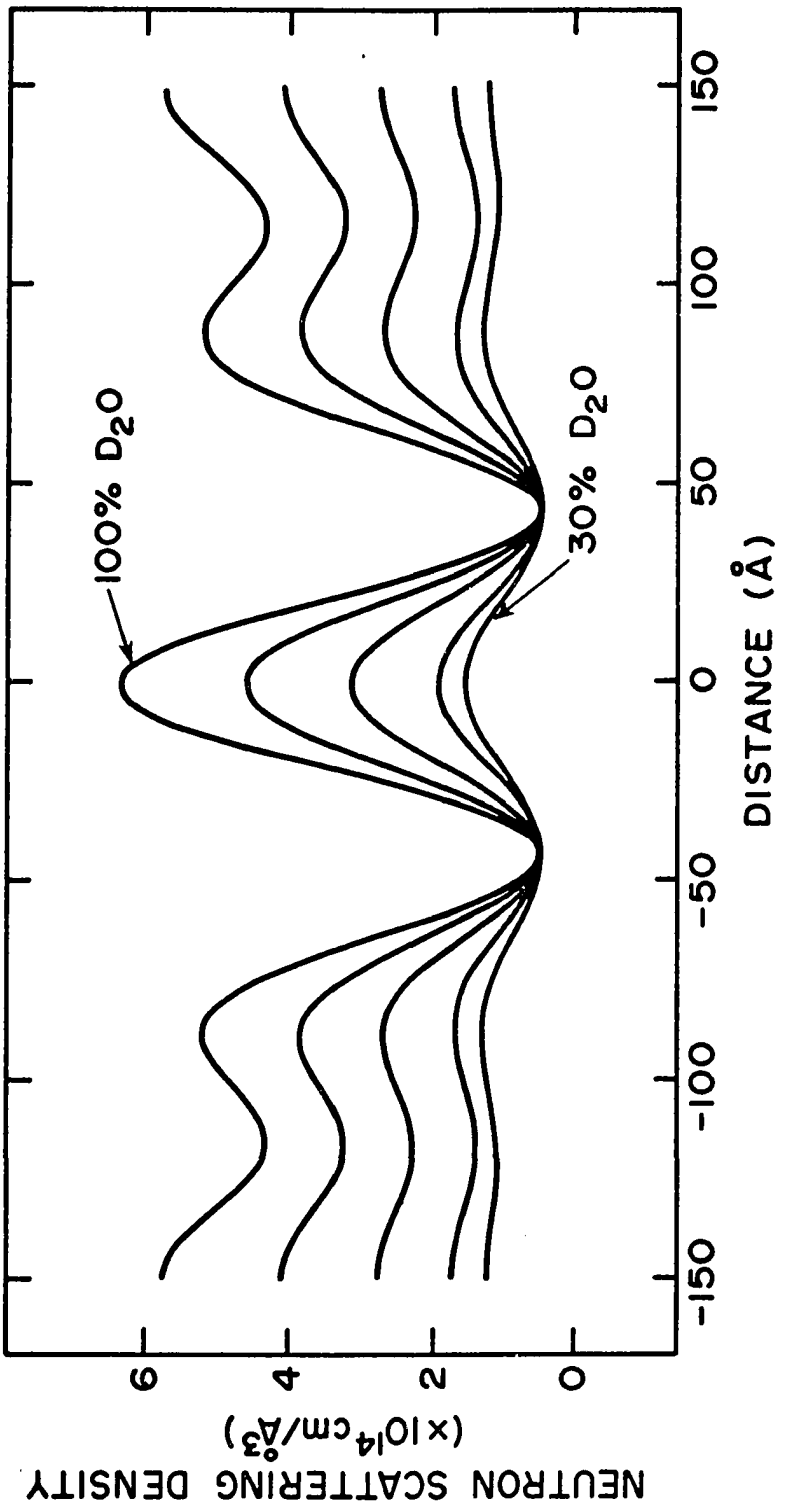

H_2O are also known since D_2O-H_2O exchange is isomorphous. By equation (2) the neutron scattering densities at 0 Å in 80%, 60%, 40%, and 30% D_2O are 4.97, 3.59, 2.20, and 1.51 x 10^{-14} cm/Å^3, respectively. The Fourier syntheses in Figure 29 have been translated to a common minimum since the scattering density of the water-excluding hydrocarbon regions should not vary with D_2O concentration. The resulting absolute scattering densities for the peaks at 0 Å match the predicted densities based on the D_2O concentration of the Ringer's solution, consistent with the hydrocarbon regions being water-excluding.

By examining the dependence of the contrast at distance x in the structure C(x), on the scattering density of the solvent ρ_w, the scattering density at the center of the low density troughs at ± 44 Å can be obtained. The scattering density at distance x, $\rho(x)$, in a one dimensional hydrated structure can be broken down into contributions from the aqueous (w) and nonaqueous (s) regions

$$\rho(x) = (1-X)\rho_s + X\rho_w \qquad (18)$$

where X is the volume fraction of water at x. C(x) is then given by

$$C(x) = \rho_w - \rho(x) \qquad (19)$$

Substitution of equation (18) into equation (19) yields

$$C(x) = \rho_w (1-X) - \rho_s (1-X) \qquad (20)$$

Since the contrast, C(x), depends linearly on the scattering density of the aqueous solvent, ρ_w, the scattering density, ρ_s, of the nonaqueous constituents in the unit cell at distance x can be obtained by extrapolating a plot of C(x) versus ρ_w to C(x) = 0. Note that this extrapolation is independent of the absolute density scale of the Fourier syntheses and only depends on the existence of an aqueous region

in the unit cell. If the contrast values, C(x), are on an absolute scattering density scale, the slope of the contrast plot, (1-X), yields the volume fraction of water at distance x (Harrison, 1969). By extrapolating a plot of C(± 44 Å) versus ρ_w shown in Figure 30 to C(± 44 Å)= 0, the neutron scattering density at the center of the low density troughs is 0.45 ± 0.20 x 10^{-14} cm/Å^3.

Neutron scattering density profiles for experiments in D_2O Ringer's solution of varying osmolarity are shown in Figure 31. The profile in 2% sucrose Ringer's solution (Figure 31a) displays two low density troughs at ±42.7 Å which move to ±47.6 Å in 0.6 diluted Ringer's solution (Figure 31d). The repeat spacing also increases from 294 Å to 328 Å in proceeding from 2% sucrose to 0.6 diluted Ringer's solution. The highest density in the profiles occurs between the troughs at the origin. The profiles also display density shoulders which move from ± 115 Å in 2% sucrose Ringer's solution to ± 130 Å in 0.6 diluted Ringer's solution.

Figure 30. The contrast at $\pm$ 44 Å in the 75 Å resolution neutron scattering density profiles of the disc membrane is linearly dependent on % D_2O. The contrast at $\pm$ 44 Å is the vertical distance between the peak at 0 Å and the troughs at $\pm$ 44 Å in the Fourier syntheses in Figure 29. The line is extrapolated to obtain a contrast-match value for the center of the disc membrane of 0.45 $\pm$ 0.20 x 10^{-14} cm/Å^3, corresponding to a D_2O concentration of 14.6$\pm$2.8%. Data points represent different specimens. In the least-squares fit, the data were weighted by their magnitudes, and the linear correlation coefficient was 0.98.

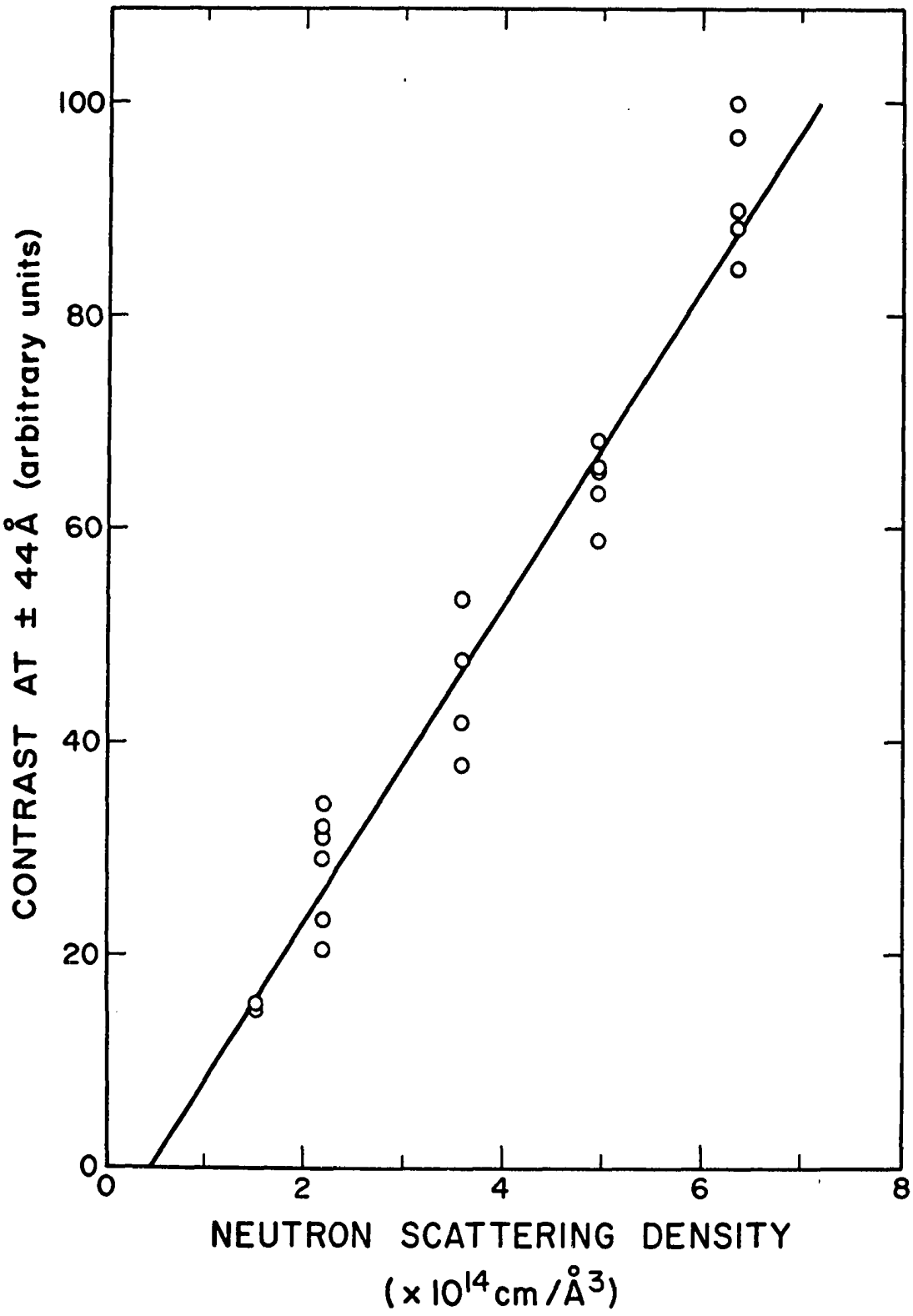

Figure 31. Neutron scattering density profiles calculated from the first four orders of diffraction from intact retinas equilibrated in D_2O Ringer's solution of varying osmolarity. (a) 2% sucrose Ringer's solution, d = 294 Å; (b) isotonic Ringer's solution, d = 298 Å; (c) 0.8 diluted Ringer's solution, d = 308 Å; (d) 0.6 diluted Ringer's solution, d = 328 Å. The separation between the low density troughs increases from 85 Å in 2% sucrose Ringer's solution to 95 Å in 0.6 diluted Ringer's solution. The Fourier syntheses have been scaled to the same vertical peak-to-trough distance.

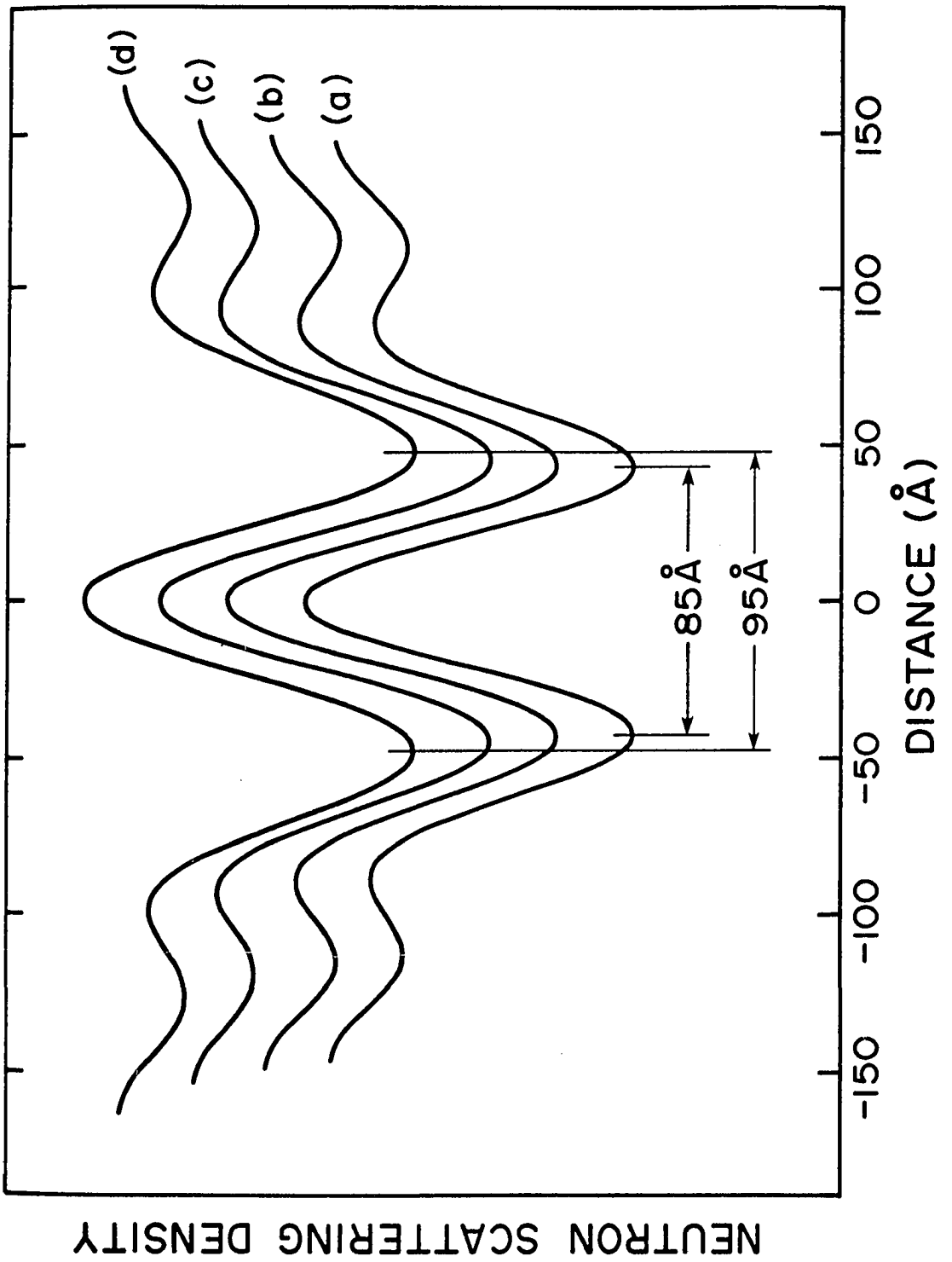

CHAPTER VI

DISCUSSION

(a) Summary of the Experimental Findings

Neutron diffraction patterns were recorded from intact frog retinas equilibrated in different D_2O-H_2O mixtures and in D_2O Ringer's solution of varying osmolarity. Reflection intensities were determined by semi-automated curve-fitting procedures. The diffuse equatorial scattering was taken to be the background for the meridional Bragg diffraction, and the background-subtracted reflections were fitted by Gaussian peaks. The sum of these Gaussians and the polynomials fitted to the diffuse equatorial scattering closely matched the observed meridional diffraction patterns. The reflection intensities were given by the product of the height and full width at $e^{-\frac{1}{2}}$ height of the Gaussian peaks. The repeat spacing was calculated from the positions of the Gaussian peaks. The structural analysis was limited to the first four reflections since their intensities, correction factors, and phases were more reliably determined than for the higher orders. The corrected intensities of the first four reflections account for about 85% of the intensity observed for the first eight orders of diffraction, so that the main structural features are represented even at low resolution.

The phases for the first four reflections were determined by interpretation of the D_2O-H_2O contrast variation effects and Patterson maps of osmotically manipulated retinas. The phases -,+,+,+ for orders

one to four obtained in this way are equivalent to the choice of a lipid bilayer model of the disc membrane. The broad Patterson peak at 84 Å would represent the separation of centers of the disc membrane pairs. Kinetic experiments and plots of the structure factor amplitudes versus $\%D_2O$ showed that the phases do not change sign over the 30% to 100% D_2O range.

Neutron scattering density profiles were calculated on an absolute scale at 75 Å resolution. These Fourier syntheses exhibit two low density troughs at ±44 Å. The contrast-match point for the low density troughs is $0.45 \pm 0.20 \times 10^{-14} cm/Å^3$, corresponding to 14.6±2.8 % D_2O.

(b) Bilayer Arrangement of Disc Membrane Lipids

The molecular interpretation of the observed neutron scattering density profiles (Figures 29 and 31) is shown in Figure 32. The continuous neutron scattering density profile is the Fourier synthesis at 75 Å resolution for an experiment in isotonic D_2O Ringer's solution. The high density regions between -18 and +18 Å and between 70 Å and 230 Å are interpreted as being predominantly aqueous since the scattering density in these regions decreases with decreasing D_2O concentration (Figure 29). The narrower 36 Å aqueous region between the low density troughs in Figure 32 is interpreted as the intradisc region, and the wider 160 Å aqueous region is interpreted as the extradisc region. The increases in the unit cell dimension and the size of the intradisc space as the osmolarity of the Ringer's solution decreases (Figure 31) indicate that the volume of water in the intradisc and extradisc compartments increases as the osmolarity of the Ringer's solution decreases.

Figure 32. Neutron scattering density profiles at 75 Å resolution of rod outer segment disc membranes in D_2O. Fourier synthesis calculated for the pure lipid bilayer model depicted at the top of the figure (••••). The experimental Fourier synthesis calculated from data recorded in D_2O Ringer's solution (——). The experimental Fourier synthesis was scaled to the calculated Fourier synthesis of the lipid bilayer model by assuming that the neutron scattering density in the center of the intradisc space (0 Å) is that of pure D_2O (6.35×10^{-14} cm/Å^3) and the scattering density at the center of the low density troughs is -0.02×10^{-14} cm/Å^3 (Figure 4) for the lipid bilayer profile and 0.45×10^{-14} cm/Å^3 (Figure 30) for the experimental profile.

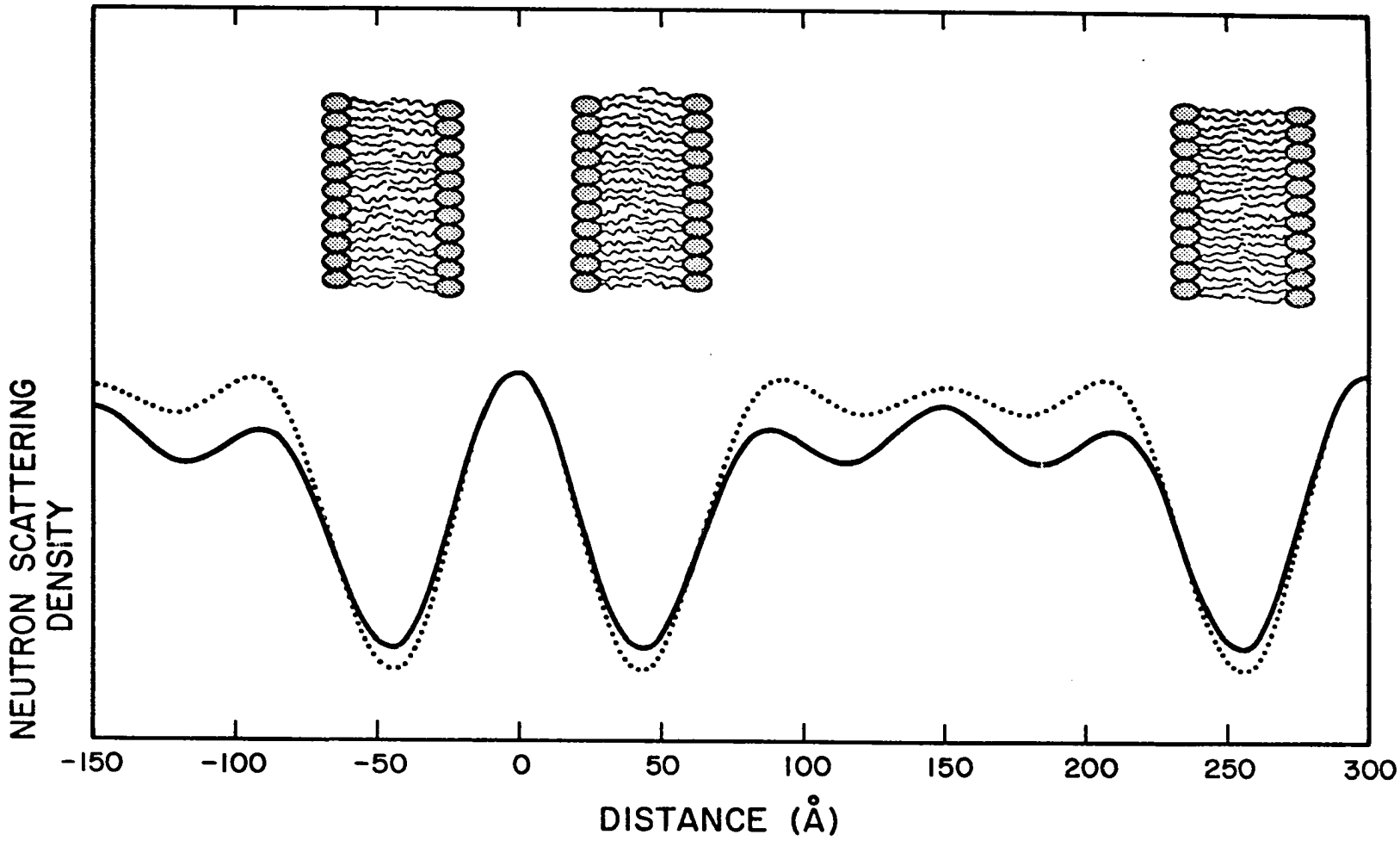

The contrast-match point for the troughs centered at ±44 Å (Figure 30) is 0.45 x 10^{-14}cm/Å^3. This low scattering density (Figure 4) and the ∿50 Å width of the troughs suggest that a major portion of the lipid molecules are arranged in a bilayer configuration. In isotonic Ringer's solution the bilayers are separated by 88 Å, and the separation between the bilayers increases as the Ringer's solution is made more hypotonic (Figure 31).

(c) Interpretation of the Contrast-Match Point at the Center of the Lipid Bilayers

The contrast-match point for the center of the disc membrane lipid bilayers at ±44 Å contains information about the chemical composition of the hydrocarbon region. To justify a quantitative interpretation of the contrast-match point, the effect of resolution had to be examined. Neutron scattering density profiles were calculated for disc membrane models with varying amounts of protein in the hydrocarbon region [Chapter VI (e)]. Model Fourier syntheses in different D_2O-H_2O mixtures were calculated at 75 Å resolution, and the contrast at ±44 Å, C(±44 Å), given by equation (20) was plotted versus D_2O concentration. The error due to the resolution was assessed by comparing the exact contrast-match point defined by the model, and the calculated contrast-match point at 75 Å resolution. These calculations revealed that the value of C(±44 Å) at 75 Å resolution differs by only ∿1% D_2O from the exact value defined by the models. Furthermore, the contrast at ±44 Å is fairly representative of the entire hydrocarbon region of the lipid bilayer because small changes in the neutron scattering density level through the hydrocarbon region are averaged due to the resolution of 75 Å.

Knowing that the contrast-match value at ±44 Å is quantitatively reliable, the chemical composition of the hydrocarbon region of the disc membrane can be estimated. The protein:lipid weight ratio of disc membranes is 50±10/50±10 (Daemen, 1973); the molecular weight of rhodopsin is 38,000 ±3,000 (Robinson, Gordon-Walker, and Bownds, 1972; Heitzmann, 1972; Daemen, DeGrip, and Jansen, 1972; Lewis, Krieg, and Kirk, 1974; Yeager, 1976a); rhodopsin comprises 80±10% of the disc membrane protein (Papermaster and Dreyer, 1974), and the molecular weight of the average rod outer segment lipid is 800 (Daemen, 1973). From these values we obtain a lipid:rhodopsin stoichiometry of 60±15. Assuming that the hydrocarbon region of the disc membrane lipid bilayer is occupied exclusively by anhydrous protein and hydrocarbon, the neutron scattering density of the hydrocarbon region, ρ_m, is given by

$$\rho_m = X_H\rho_H + X_p\rho_p \qquad (21)$$

where X_p is the volume fraction of protein in the hydrocarbon region, X_H is the volume fraction of hydrocarbon, and $X_p + X_H = 1$. From equation (3) and using a value of $\rho_H = -0.02 \times 10^{-14}$ cm/Å^3, equation (21) becomes

$$\rho_m = -0.02 \times 10^{-14} + X_p(1.92 \times 10^{-14} + 1.27 \times 10^{-14}\beta\gamma) \qquad (22)$$

and X_p is given by

$$X_p = \frac{\rho_m + 0.02 \times 10^{-14}}{1.92 \times 10^{-14} + 1.27 \times 10^{-14}\beta\gamma} \qquad (23)$$

For a lipid:rhodopsin stoichiometry of 60±15, the total volume of lipid hydrocarbon is (60±15)(982 Å^3/2 hydrocarbon chains) = 58,920 ± 14,730 Å^3. (The volume of 982 Å^3 for two average rod outer segment hydrocarbon chains was calculated from Traube volumes of the atomic

nuclei.) The calculated anhydrous volumes of rhodopsin and non-rhodopsin protein are 47,000 $\mathring{A}^3$ and 11,750 $\mathring{A}^3$.

By setting $\rho_m=\rho_w$ [given by equation(2)] and substituting the experimental value of $\beta=.146\pm.028$ into equation(23), the volume fraction of protein residing in the hydrocarbon region is .24 ±.10 if $\gamma=0$ or .22 ±.09 if $\gamma=1$. If all non-rhodopsin protein resides in the hydrocarbon region, then 35± 25% of the rhodopsin resides in the hydrocarbon region. If all non-rhodopsin protein resides outside the hydrocarbon region, then 54± 25% of the rhodopsin resides in the hydrocarbon region. If all disc membrane protein resides in the hydrocarbon region, the calculated contrast-match point would be 23±3% D_2O. Since this value is significantly larger than the experimental value of 14.6±2.8% D_2O not all of the disc membrane protein resides in the hydrocarbon region.

Note that the large uncertainties in the estimate of the fraction of rhodopsin in the hydrocarbon region are mainly based on (1) the large uncertainty in the chemical composition of the disc membrane, in particular the lipid:rhodopsin stoichiometry and (2) uncertainty in the location of the non-rhodopsin protein. It must also be stressed that the calculation of the contrast-match point relied on the assumption that the intradisc space is occupied by pure Ringer's solution. If the intradisc space contains non-aqueous material with a contrast-match value greater than 15% D_2O (for example protein or carbohydrate), then the contrast-match value at ±44 $\mathring{A}$ would be greater than 15% D_2O, and the estimate of the amount of protein in the hydrocarbon region would be correspondingly increased.

(d) Asymmetry of the Neutron Scattering Density Profiles

The dotted profile in Figure 32 is the calculated neutron scattering density profile in D_2O at 75 Å resolution for the lipid bilayer model shown at the top of the figure. The curvature in the troughs and the modulation in the extradisc space are due to series termination error in the calculated profile. As expected, the density levels of the intradisc and extradisc spaces in the calculated Fourier synthesis for a lipid bilayer model are almost the same except for a slight difference due to series termination error. In contrast, the experimental Fourier synthesis (continuous curve) is strikingly asymmetric: the neutron scattering density levels in the intradisc and extradisc spaces are markedly different. The calculated Fourier synthesis for the lipid bilayer demonstrates that this difference cannot be accounted for by series termination error. The lower density of the extradisc space compared to the intradisc space in the experimental Fourier synthesis indicates that there is a substantial amount of hydrogenated material in the extradisc region.

To investigate the effect of resolution on the neutron scattering density profiles, Fourier syntheses including 6 and 8 reflections (50 Å and 37.5 Å resolution, respectively) were calculated using the observed diffraction data in D_2O Ringer's solution. The phases for the first eight orders (-,+,+,+,+,-,+,+) were obtained by Fourier transformation of the lipid bilayer model shown in Figure 32. This method of phasing relies on the assumption that the lipid bilayer dominates the phases since the greatest contrast in the structure in D_2O is between the water and hydrocarbon regions. The reduced extradisc neutron

scattering density compared with the density in the intradisc space is preserved in the 50 Å and 37.5 Å resolution Fourier syntheses in D_2O Ringer's solution (Figure 33). It should be stressed that by using phases calculated from the lipid bilayer model in which the intradisc and extradisc neutron scattering densities are equal, the experimental Fourier syntheses are biased toward symmetric structures. Therefore, the retention of the asymmetry in these higher resolution Fouriers strongly supports the existence of asymmetry between the intradisc and extradisc neutron scattering density levels.

(e) A Model Building Approach to Interpret the Asymmetry of the Neutron Scattering Density Profiles

There are three possible explanations for the lower neutron scattering density level in the extradisc aqueous space compared with the intradisc space: (1) that the asymmetry is due to rhodopsin extending into the extradisc region; (2) that the asymmetry is not due to rhodopsin but other nonaqueous, hydrogenated material; and (3) that the asymmetry is due both to rhodopsin and other nonaqueous hydrogenated material. A model building approach was used to examine these three possible interpretations.

The following parameters defined the models: (1) the anhydrous molecular volume of rhodopsin is 47,000 $Å^3$ (see Figure 4); (2) the volume of two average rod outer segment hydrocarbon chains is 982 $Å^3$ [see Chapter VI (c)]; (3) the volume of the average lipid headgroup is 640 $Å^3$ with a 64 $Å^2$ cross sectional area (Luzzati, 1968; Johnson, Bangham, Hill and Korn, 1971; Engelman, 1971; Demel, Geurts Van Kessel and VanDeenen, 1972) and a 10 Å length (Engelman, 1971); (4) the lipid: rhodopsin stoichiometry is 60 [see Chapter VI (c)]; (5) the neutron

Figure 33. Neutron scattering density profiles of rod outer segment disc membranes in D_2O. Fourier synthesis calculated for a pure lipid bilayer model (····); the lipid bilayer structure factors for orders 1 to 8 are -323, 127, 351, 228, 16.1, -41.2, 16.2 and 27.4, respectively. Experimental Fourier syntheses (———) calculated using phases from the lipid bilayer model; the structure factor amplitudes given by equation (15) are 333, 254, 441, 378, 204, 179, 121 and 98. The Fourier syntheses were scaled as in Figure 32. (a) 6 orders of diffraction included in Fourier synthesis. (b) 8 orders of diffraction included in Fourier synthesis.

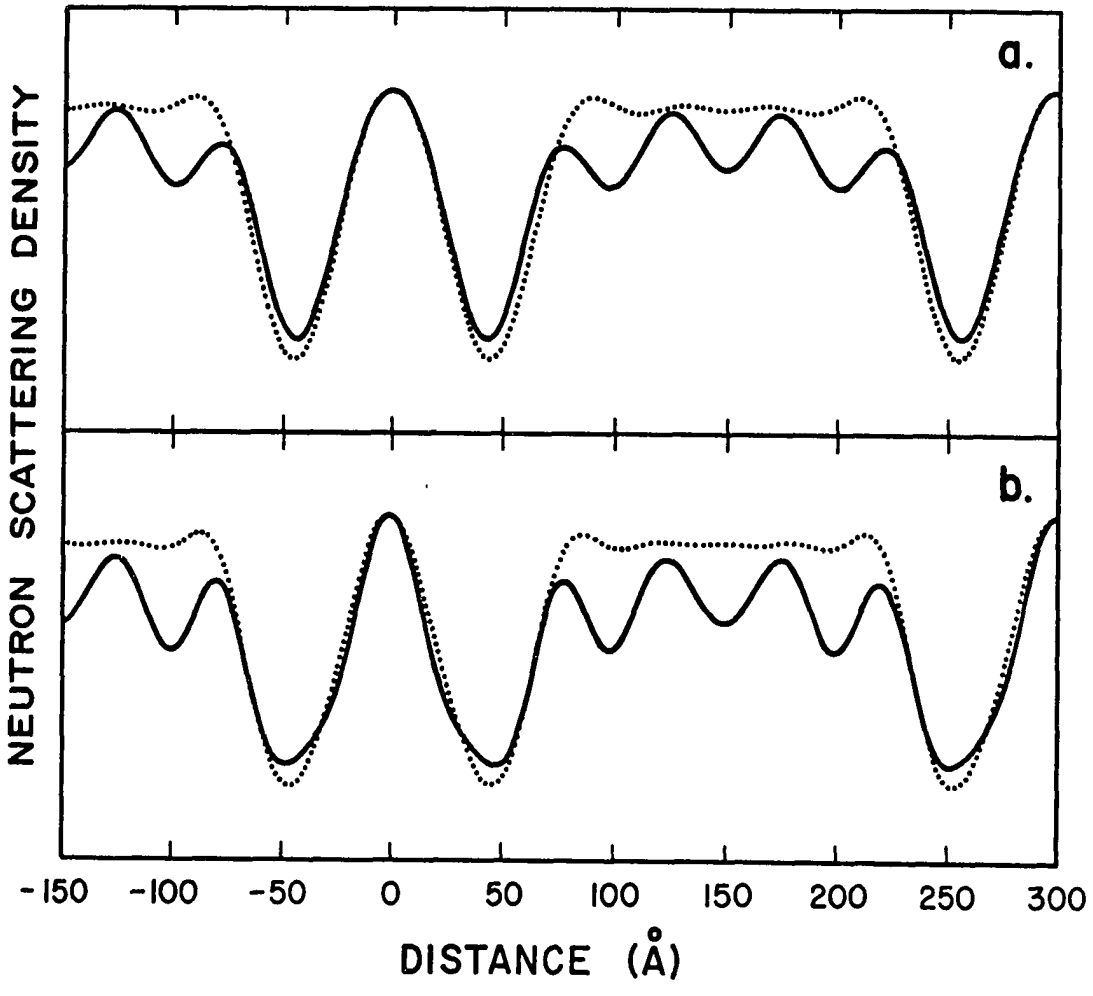

scattering densities of rhodopsin and water are given by equations 2 and 3, respectively, and the scattering densities for the lipid headgroup and hydrocarbon chains are shown in Figure 4; (6) the disc membrane lipids are packed in 50 Å thick lipid bilayers as shown in Figure 32 with intradisc and extradisc aqueous spaces of 36 Å and 160 Å, respectively; (7) the region of the lipid bilayers distorted by the presence of rhodopsin has the same neutron scattering density as the undistorted bilayer; (8) the rhodopsin molecule was assumed to be a cylinder with its axis perpendicular to the plane of the disc membrane. Three general shapes were considered: elongated with a length of 80 Å and a diameter of 27 Å (model a.), roughly symmetric with a length of 40 Å and a diameter of 38 Å (model b.) and flattened with a length of 20 Å and a diameter of 54 Å (model c.)

Rhodopsin molecules were placed centrosymmetrically at different positions in the 300 Å unit cell, and the one dimensional projection of the neutron scattering density was determined. The Fourier transform of the model scattering density profile was calculated by equation (4), and the Fourier synthesis by equation (5). A qualitative assessment of the model was made by visually comparing the calculated model Fourier synthesis to the experimental Fourier synthesis. The calculated structure factor amplitudes, $F_{calc}(h)$, were scaled to the observed structure factor amplitudes, $F_{obs}(h)$, by setting $\sum_{h=1}^{6} (F_{calc}(h))^2 = \sum_{h=1}^{6} (F_{obs}(h))^2$. The experimental Fourier synthesis could then be placed on an absolute neutron scattering density scale by including $F_{calc}(0)$ in equation (5) and using the phases calculated from the model. A quantitative assessment of the model which did not rely on the choice of phases was made by calculating the residual, R

$$R = \frac{\sum_{h=1}^{6} \left| k|F_{obs}(h)| - |F_{calc}(h)| \right|}{\sum_{h=1}^{6} k|F_{obs}(h)|} \qquad (24)$$

where $k^2 = \sum_{h=1}^{6} (F_{calc}(h))^2 / \sum_{h=1}^{6} (F_{obs}(h))^2$.

The results of these calculations are summarized in Table 3. The distance values in the horizontal direction indicate the position of the centroid of the rhodopsin molecule with respect to the center of the intradisc space. In the vertical direction the neutron scattering density of the cytoplasmic extradisc aqueous space is varied from 6.35×10^{-14} cm/Å^3, corresponding to pure D_2O Ringer's solution, to lower values, corresponding to increasing amounts of non-rhodopsin hydrogenated material in the extradisc region. The contours in Table 3 surround the regions with R values less than .20 and indicate the models in best agreement between the observed and calculated structure factor amplitudes.

Two conclusions can be drawn from Table 3. (1) The best models have neutron scattering density levels in the extradisc space less than pure D_2O Ringer's solution. Therefore, rhodopsin cannot entirely account for the asymmetry, suggesting that other hydrogenated material resides in the extradisc region. (2) The models in best agreement with the experimental structure factor amplitudes orient rhodopsin asymmetrically on the cytoplasmic face of the disc membrane. This result is consistent with the interpretation of freeze-fracture electron micrographs of rod outer segments (Corless, Cobbs, Costello, and Robertson,

Table 3

RESIDUAL VALUES COMPARING THE EXPERIMENTAL STRUCTURE FACTOR AMPLITUDES IN D_2O RINGER'S SOLUTION TO STRUCTURE FACTORS CALCULATED FROM DISC MEMBRANE MODELS

Cylindrical rhodopsin molecules are oriented with their axes perpendicular to the plane of the disc membrane. The distance values in the horizontal direction indicate the position of the centroid of the rhodopsin molecules with respect to the center of the intradisc space. In the vertical direction the neutron scattering density of the cytoplasmic extradisc space is varied. The contours surround the regions with residual values less than .20 and indicate the models in best agreement between the observed and calculated structure factor amplitudes. See text for details.

MODEL	RHODOPSIN DIMENSIONS length (Å)	diameter (Å)
a.	80	27
b.	40	38
c.	20	54

DISTANCE (Å)

CYTOPLASMIC NEUTRON SCATTERING DENSITY ($\times 10^{14}$ cm/Å^3)

	center of intradisc space ↓ 0	10	lipid bilayer 20	30	40	50	60	70	80	90	100	110	120	130	center of extradisc space ↓ 140	150
a. 6.35					.39	.34	.28	.24	.22	.23	.24	.23				
6.05					.37	.32	.26	.21	.19	.21	.22	.21				
5.75					.34	.29	.23	.19	.18	.20	.21	.20				
5.45					.31	.26	.21	.18	.16	.18	.20	.21				
5.15					.28	.23	.19	.17	.17	.19	.22	.22				
4.85					.24	.21	.22	.19	.19	.22	.24	.24				
4.55					.21	.23	.25	.23	.22	.24	.26	.26				
4.25					.22	.25	.28	.27	.24	.27	.29	.29				
3.95					.27	.29	.32	.30	.27	.29	.31	.32				
3.65					.31	.33	.35	.33	.31	.31	.34	.34				
3.35					.36	.36	.38	.36	.35	.35	.36	.37				
b. 6.35			.36	.38	.35	.35	.30	.26	.25	.24	.21	.30	.35	.44		
6.05			.35	.36	.32	.32	.27	.23	.23	.21	.19	.28	.36	.43		
5.75			.33	.33	.29	.29	.23	.20	.22	.19	.18	.27	.37	.43		
5.45			.31	.31	.26	.25	.20	.17	.20	.16	.18	.26	.39	.42		
5.15			.29	.27	.23	.27	.15	.14	.18	.16	.19	.26	.38	.41		
4.85			.27	.24	.24	.20	.13	.14	.19	.18	.20	.27	.37	.40		
4.55			.24	.27	.27	.22	.14	.16	.21	.21	.24	.29	.37	.39		
4.25			.21	.31	.31	.25	.19	.21	.24	.25	.27	.31	.36	.37		
3.95			.24	.35	.35	.29	.24	.26	.27	.29	.30	.34	.36	.36		
3.65			.28	.40	.38	.33	.29	.30	.31	.32	.33	.36	.37	.36		
3.35			.32	.44	.39	.37	.34	.35	.35	.36	.37	.37	.38	.38		
c. 6.35	.55	.37	.28	.38	.29	.30	.31	.33	.26	.20	.32	.27	.38	.45		
6.05	.54	.35	.26	.36	.25	.27	.29	.31	.23	.17	.32	.29	.39	.46		
5.75	.53	.32	.23	.34	.21	.24	.27	.30	.21	.16	.32	.31	.41	.47		
5.45	.52	.30	.22	.31	.16	.21	.25	.28	.18	.15	.33	.33	.41	.45		
5.15	.50	.27	.26	.30	.11	.18	.22	.25	.17	.15	.31	.35	.41	.43		
4.85	.48	.24	.30	.33	.12	.19	.21	.26	.17	.17	.29	.37	.40	.40		
4.55	.45	.20	.35	.37	.15	.23	.23	.27	.20	.19	.30	.39	.39	.38		
4.25	.43	.21	.40	.41	.18	.26	.24	.29	.23	.22	.32	.37	.37	.36		
3.95	.39	.24	.44	.44	.21	.29	.28	.30	.27	.27	.34	.37	.36	.33		
3.65	.35	.28	.48	.48	.27	.32	.31	.32	.31	.31	.36	.38	.36	.32		
3.35	.30	.33	.49	.44	.32	.35	.35	.36	.35	.36	.38	.38	.38	.36		

1976) and x-ray diffraction studies on pelleted disc membranes (Santillan and Blasie, 1976). For models a. and b. in which rhodopsin has a length of 80 Å and 40 Å, respectively, the best models are those in which rhodopsin extends into the extradisc aqueous space. These structures are consistent with the accessibility of rhodopsin to labelling and proteolysis by water-soluble macromolecular probes (Steinemann and Stryer, 1973; Yariv, Kalb, and Giberman, 1974; Trayhurn, Mandel, and Virmaux, 1974a, b; Saari, 1974; van Breugel, Daemen, and Bonting, 1975; Pober and Stryer, 1975; Pober, Iwanij, Reich, and Stryer, 1976). For model c. in which rhodopsin is a flattened cylinder with a length of 20 Å, there are two classes of structures in good agreement with the experimental data; however, the structures are rather implausible. In the first class, rhodopsin is buried in the lipid bilayer on the cytoplasmic face of the disc membrane. These structures are not consistent with the accessibility of rhodopsin to labelling and proteolysis. The second class of structures are highly implausible since they position rhodopsin in the extradisc space, completely detached from the disc membrane.

Figure 34 compares the experimental 50 Å resolution experimental Fourier synthesis to the Fourier syntheses calculated for the best models from Table 3. It can be seen that the neutron scattering density profiles of the best models closely match the experimental profiles and adequately account for the asymmetry between the density levels in the extradisc and intradisc aqueous spaces.

(f) Evaluation of Non-rhodopsin Extradisc Solids

The concentration of non-rhodopsin solids in the extradisc region can be estimated from the calculated neutron scattering density in the

Figure 34. Experimental neutron scattering density profiles in D_2O Ringer's solution (————) and calculated neutron scattering density profiles for the disc membrane models in Table 3 (••••••••) in best agreement with the experimental structure factor amplitudes. The experimental Fourier syntheses were calculated at 50 Å resolution using model phases and were placed on an abolute scale by including $F_{calc}(0)$ in the Fourier synthesis. The Fourier syntheses of the step function models were also calculated at 50 Å resolution.

a. Rhodopsin is 80 Å long and extends from 40 to 120 Å in the unit cell. Cytoplasmic neutron scattering density = 5.30×10^{-14} cm/Å^3. R=.161

b. Rhodopsin is 40 Å long and extends from 40 to 80 Å in the unit cell. Cytoplasmic neutron scattering density = 4.70×10^{-14} Å^3. R=.133

c. Rhodopsin is 20 Å long and extends from 40 to 60 Å in the unit cell. Cytoplasmic neutron scattering density = 5.00×10^{-14} cm/Å^3. R=.111

h	a. $k \cdot F_{obs}$	a. F_{calc}	b. $k \cdot F_{obs}$	b. F_{calc}	c. $k \cdot F_{obs}$	c. F_{calc}
0		1156		1124		1223
1	190	-194	169	-147	159	-156
2	132	135	118	114	111	81
3	234	248	208	241	196	214
4	206	217	183	183	173	178
5	100	72	89	83	84	89
6	95	-1.4	84	36	79	52
k	.538		.479		.451	

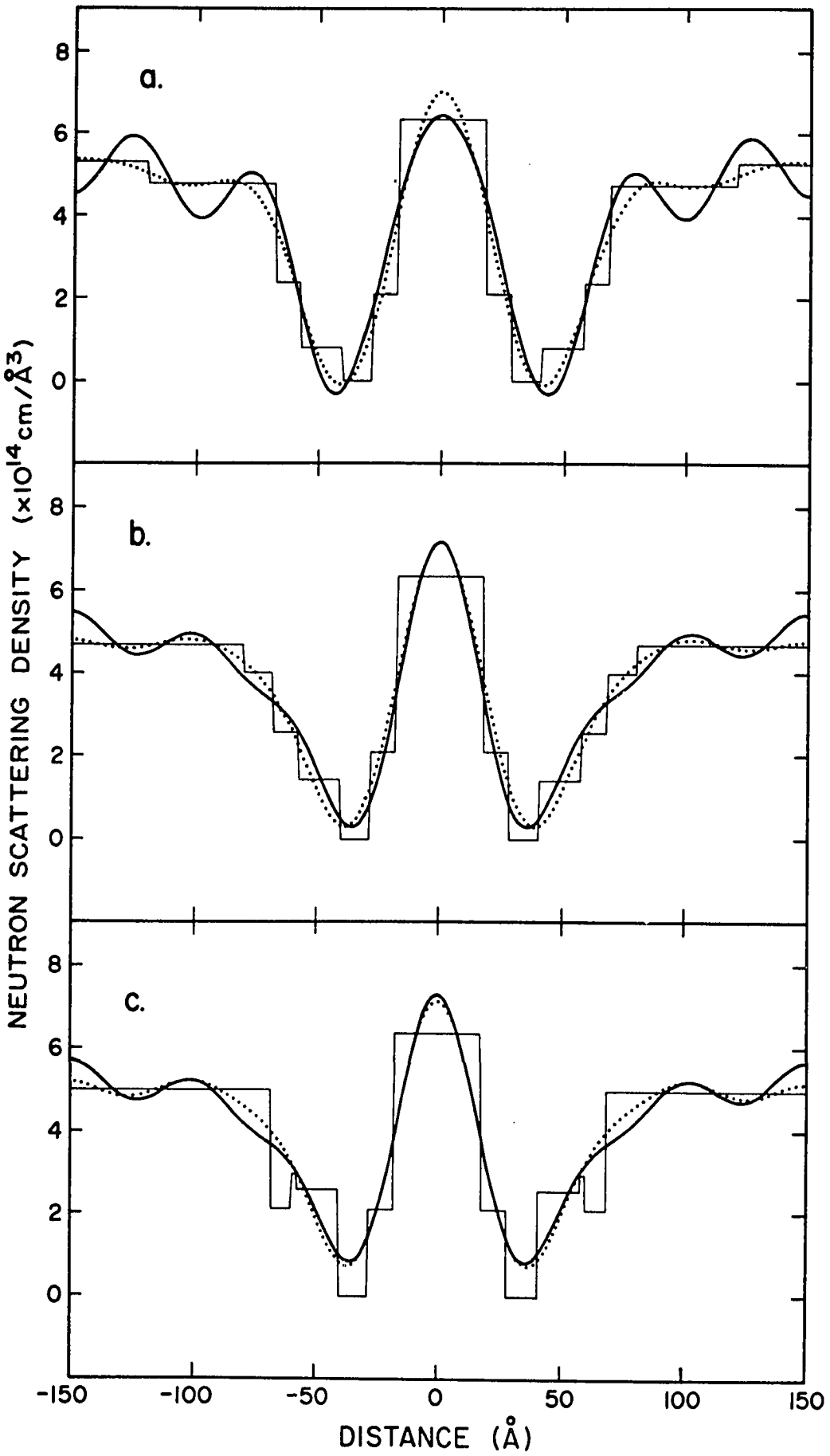

extradisc space of $\sim 5 \times 10^{-14}$ cm/Å^3 (Figure 34 and Table 3). The volume fraction of protein, 1-X, can be solved from equations (2),(3) and (18), knowing that $\rho_s = \rho_p$. In D_2O Ringer's solution $\rho_w = 6.35 \times 10^{-14}$ cm/Å^3, $\beta = 1$ and $\rho(x) = 5 \times 10^{-14}$ cm/Å^3. For a 6 μ diameter rod outer segment the unit cell volume is 8.34×10^{11} Å^3 and the extradisc volume is 4.5×10^{11} Å^3. The volume fraction of protein in the extradisc space is therefore .303 (γ=0) to .424 (γ=1) corresponding to a weight concentration of 41% (γ=0) to 58% (γ=1) for a protein with $\bar{v}$ = 0.74 cm^3/g. With a rhodopsin concentration in frog rod outer segments of 3.1 ± 0.1 mM (Liebman, 1975), there are 1.6×10^6 rhodopsin molecules/unit cell. The above concentrations of non-rhodopsin protein in the extradisc space therefore correspond to 7×10^4 daltons protein/38,000 daltons rhodopsin (γ=0) to 1×10^5 daltons protein/38,000 daltons rhodopsin (γ=1).

Based on the structure of sucrose with eight potentially exchangeable hydrogens out of 22, the neutron scattering density of carbohydrate, ρ_c, is given by

$$\rho_c = 1.7 \times 10^{-14} + 2.3 \times 10^{-14} \beta\gamma \qquad (25)$$

If the extradisc nonaqueous material is carbohydrate, then its volume fraction would be .29 (γ=0) to .57 (γ=1) with $\rho_s = \rho_c$. Using $\bar{v}$ = .63 cm^3/g the carbohydrate concentration in the extradisc space would be 46% (γ=0) to 91% (γ=1).

These estimates for the concentration of solids in the extradisc space are very high; it is unlikely that the true value is as high as predicted by these computations, which are based on low resolution data. Nevertheless, these computations do indicate that there is a striking amount of non-aqueous material in the extradisc space, and there are

data from other sources to support this point of view.

If there is so much material in the extradisc space, it should be detectable by x-ray diffraction. The model refined to fit the neutron diffraction data in Figure 34a predicts the following x-ray structure factors for orders 1 to 10, respectively: -50, -71, 29, 40, 10, -69, -122, -67, -5, and 25. The calculated amplitudes for orders 6 and 7 are large, in agreement with the observed amplitudes listed in Figure 3; however, the amplitudes for orders 2 and 3 are reversed, with order 2 having a calculated amplitude substantially larger than the experimental value. The phases calculated from the model are identical to the experimental phases of the strongest reflections except for the first reflection, which has a calculated phase of -1 instead of +1. The dotted curve in Figure 3a is the x-ray Fourier synthesis calculated using experimental structure factors and a phase of -1 for the first reflection. The Fourier synthesis is still dominated by the electron-dense phosphate headgroups, but the extradisc x-ray scattering density level is strikingly higher than the density level in the intradisc space. Since protein and carbohydrate have x-ray scattering densities larger than water (Figure 4), this increased density level in the extradisc space suggests that nonaqueous material resides in this region, consistent with the interpretation of the asymmetry of the neutron scattering density profiles. The argument used by x-ray workers to assign a phase of +1 to the first reflection is that the average electron density of the disc is greater than the electron density of cytoplasm in the extradisc region. However, if a substantial amount of nonaqueous material resides in the extradisc space, then the average electron density of this region may

exceed that of the disc, allowing the first reflection to have a phase of -1.

If the lower neutron scattering density on the extradisc sides of the disc membrane is due to rhodopsin and other protein or carbohydrate, then the extradisc and intradisc levels should be equal between 30 and 45% D_2O where these chemical components would be expected to be contrast-matched. Although the extradisc shoulders in the neutron Fourier syntheses in Figure 29 appear to be suppressed as the D_2O concentration changes from 100 to 30%, the extradisc neutron scattering density level is still less than the intradisc level in 30% D_2O. However, model calculations similar to those described in Chapter VI (e) showed that contrast-matching of extradisc material would not be detectable at 75 Å resolution, although it should be detectable at 30 Å resolution.

The concentration of solids in the rod outer segment obtained by refractometry is 44 ± 10 g/100 cm^3 (Sidman, 1957; Blaurock and Wilkins, 1969; Webb, 1972). Based on the rod outer segment composition and size stated above, this solids concentration predicts that the extradisc space contains a solids content of 30%. The solids content of the extradisc space based on birefringence studies (Liebman, et al., 1974) is 16%. In a personal communication Liebman has stated that the birefringence data are consistent with an extradisc solids concentration ranging from 10-30%. Furthermore, a source of uncertainty in the measurement of the index of refraction and the static birefringence is whether the isolated rod outer segments were osmotically intact. Although these measurements with visible light predict a solids concentration in the extradisc region lower than our estimates based on

neutron diffraction, the results are clearly in qualitative agreement; there indeed appears to be a large amount of solute material in the extradisc space.

(9) Comparison with Saibil, Chabre and Worcester (1976)

Table 4 compares my neutron diffraction experiments on intact retinas with similar experiments on isolated rod outer segments oriented in a magnetic field (Chabre, Saibil and Worcester, 1975; Saibil, Chabre and Worcester, 1976). The diffraction patterns in D_2O Ringer's solution are qualitatively very similar (Figure 35). The first four orders dominate the pattern with the intensity of reflection 1 strongest, followed by reflections 3, 2 and 4, respectively. The intensities of reflections 2, 3 and 4 are stronger in pattern b. compared with a. because the intensities in b. were obtained by integrating over the arcs of mosaic spread. The resolution of the peaks in a. is substantially better than in b. because the instrumental angular resolution, $\Delta 2\theta$, is about three-fold smaller in a. Gaussian peaks were fitted to the Bragg reflections as described in Chapter IV (d) (iii). The fit to the first four reflections in pattern b. is quite good; however, the fits to reflections 5, 6, and 7 are unreliable because the reflections are not resolved and there are only four points defining each reflection. Note that in pattern a. each reflection is defined by 9 points, and reflections 5 and 6 are well-resolved. Since the intensities in pattern b. were obtained by integrating over the arcs of mosaic spread, Chabre et al. (1976) applied a reciprocal Lorentz factor of h to the integrated intensities, so that their structure factor amplitudes are given by $F(h) = |(h \cdot I(h))^{\frac{1}{2}}|$. The structure factor amplitudes for the reflections in a. are given by equation 15.

Table 4

COMPARISON OF MY RESULTS

WITH THOSE OBTAINED BY SAIBIL, CHABRE, AND WORCESTER (1976)

	Yeager	Saibil et al.
Sample	intact frog retinas	isolated frog rod outer segments
Orientation of rods	natural	magnetic field
Detector	Soller slit step-scanning diffractometer ($\Delta\lambda/\lambda$=.025)	Area detector ($\Delta\lambda/\lambda$=.08)
Time of data collection for orders 1-4	∿35 min	∿10 min
Period	295 ± 5 Å	295 Å
Structure Factor Amplitudes in D_2O Ringer's Solution		
F(1)	* 353 ± 25	/ 353
F(2)	246 ± 19	229
F(3)	434 ± 13	383
F(4)	383 ± 19	235
F(5)	186 ± 21	126
F(6)	176 ± 8	136
F(7)	113 ± 18	85
F(8)	98 ± 8	---
Phases	-,+,+,+	-,+,+,+,±,-,-
Width of Intradisc Space	∿36 Å	∿36 Å
Width of Extradisc Space	∿160 Å	∿155 Å
Center-to-Center Separation of Lipid Bilayers	∿88 Å	∿90 Å

	Yeager	Saibil et al.
Neutron Scattering Density ($\times 10^{14}$ cm/Å^3) (origin at center of intradisc space)		
ρ(0Å)	6.35	** 6.01 - 7.06
ρ(44-45Å)	0.45 ± 0.20	0.48
ρ(115Å)	4.1	5.63 - 6.65
ρ(147-150Å)	5.5	5.99 - 7.06
% Rhodopsin in Hydrocarbon Region	35±25 → 54±25 % depending on location of non-rhodopsin protein; pure Ringer's in intradisc space; 60 ± 15 lipids/rhodopsin	50 → 100% lower limit: pure Ringer's in aqueous spaces upper limit: 20% carbohydrate in aqueous spaces; 90 lipids/rhodopsin
Estimated Concentration of Solids in Extradisc Space (daltons/38,000 daltons rhodopsin)	8×10^4 - 1.6×10^5 if carbohydrate; 7×10^4 - 1×10^5 if protein	---

* Errors are ± 1 standard deviation from the mean

/ Structure factors in D_2O Ringer's solution were obtained by extrapolation of F(h) versus $\%D_2O$ plots to 100% D_2O.

** Range of densities is due to different phase choices for reflection 5.

Figure 35. Comparison of neutron diffraction in isotonic D_2O Ringer's solution from intact retinas a. and isolated rod outer segments oriented in a magnetic field b. (Chabre, Saibil and Worcester, 1976). The background-subtracted pattern in a. is from the experiment shown in Figure 15. The diffraction patterns in a. and b. were scaled to the same peak maxima for reflection 1 (continous curve) and for reflection 5 in the expanded plots (dotted curves). The scale factors are (—0—0—x8.3 x 10^{-4}), (···Δ···Δ···x 5.00 x 10^{-2}) in a. and (—0—0—x 4.43 x 10^{-3}), (···Δ···Δ···· x 9.45 x 10^{-2}) in b. The curves drawn through the data points are Gaussian peaks fitted to the Bragg reflections. The instrumental resolution Δ 2θ given by equation (6) is shown for the low-angle diffractometer used at Brookhaven National Laboratory a. and the D11 instrument at the Institut Laue-Langevin in Grenoble b.

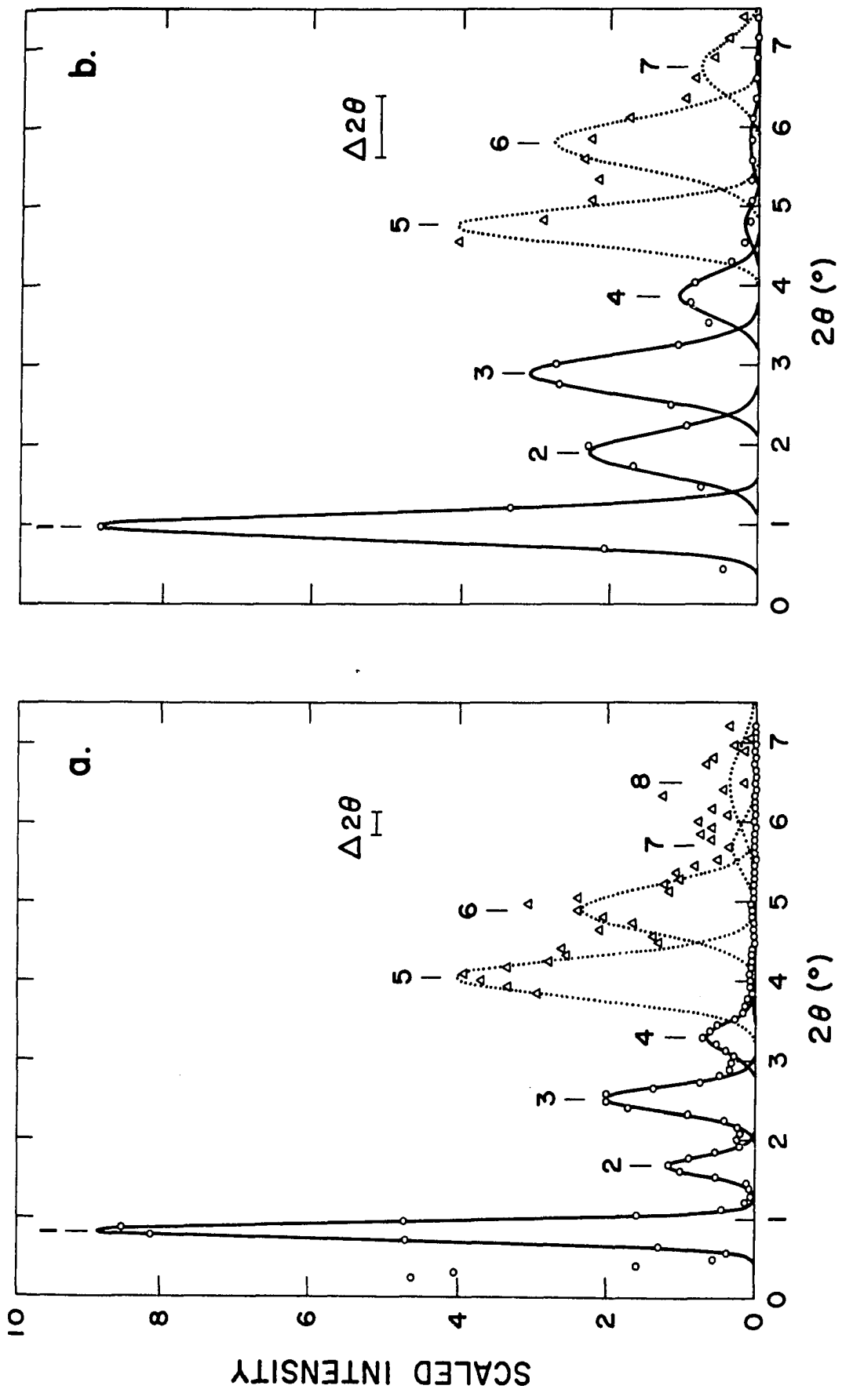

The Fourier syntheses at 75 Å resolution (Figure 36) are also very similar in that they both display low density troughs corresponding to the lipid bilayers and high density regions in the aqueous intradisc and extradisc spaces. The notable difference between the Fourier syntheses is that the neutron scattering density level in the extradisc region is lower in my Fourier, thereby predicting a greater amount of nonaqueous material in the extradisc space. Since the Fouriers were calculated using the same phases, these density differences in the extradisc region must be due to differences in the structure factor amplitudes. Table 4 shows that the amplitudes for orders 2, 3 and 4 are larger in our experiment, causing the lower density level in the extradisc space in my Fourier synthesis. It is not clear at this time whether these structure factor differences represent differences in the rod outer segments in the two preparations or whether they arise from methodological differences. It is noteworthy that the large bandwidth of the neutron beam (8%) in the experiments of Saibil et al. (1976) caused substantial smearing of adjacent reflections, hindering the quantitative determination of the reflection intensities. The reflection smearing caused by the bandwidth of 2.5% and the large mosaic spread of the samples in my experiments was quantitatively treated by curve-fitting procedures described in Chapter IV (d).

Saibil et al. (1976) observed changes of 10-15% in the structure factors for orders one to four upon bleaching the rods. These changes were within the experimental reproducibility of my bleaching experiments. The same contrast-match point for the center of the lipid bilayers was obtained in both experiments (15% D_2O). The difference in the estimate of the amount of rhodopsin residing within the hydrocarbon

Figure 36. 75Å resolution neutron scattering density profiles of rod outer segment disc membranes in D_2O Ringer's solution. (-----) Fourier synthesis calculated using the integrated intensities obtained from the areas of Gaussian peaks fitted to the neutron diffraction from isolated rod outer segments oriented in a magnetic field shown in Figure 35b. The structure factor amplitudes given by $F(h) = |(h \cdot I(h))^{1/2}|$ are 353, 229, 383 and 235 for orders 1 to 4 respectively. (———) Fourier synthesis calculated using mean structure factor amplitudes from 13 independent experiments on intact retinas. The mean structure factor amplitudes, $\overline{F(h)}$, given by equation 15 are 353±25, 246±15, 434±13 and 383±19 for orders 1 to 4, respectively. The errors are ± 1 standard deviation from the mean (±1σ). (•••••) Error syntheses calculated using Fourier coefficients $\overline{F(h)} \pm 2\sigma(h)$ in equation (17). The continuous and dashed profiles have been scaled to the same vertical peak-to-trough distance. The Fourier syntheses were calculated using phases -,+,+,+ for orders 1 to 4, respectively.

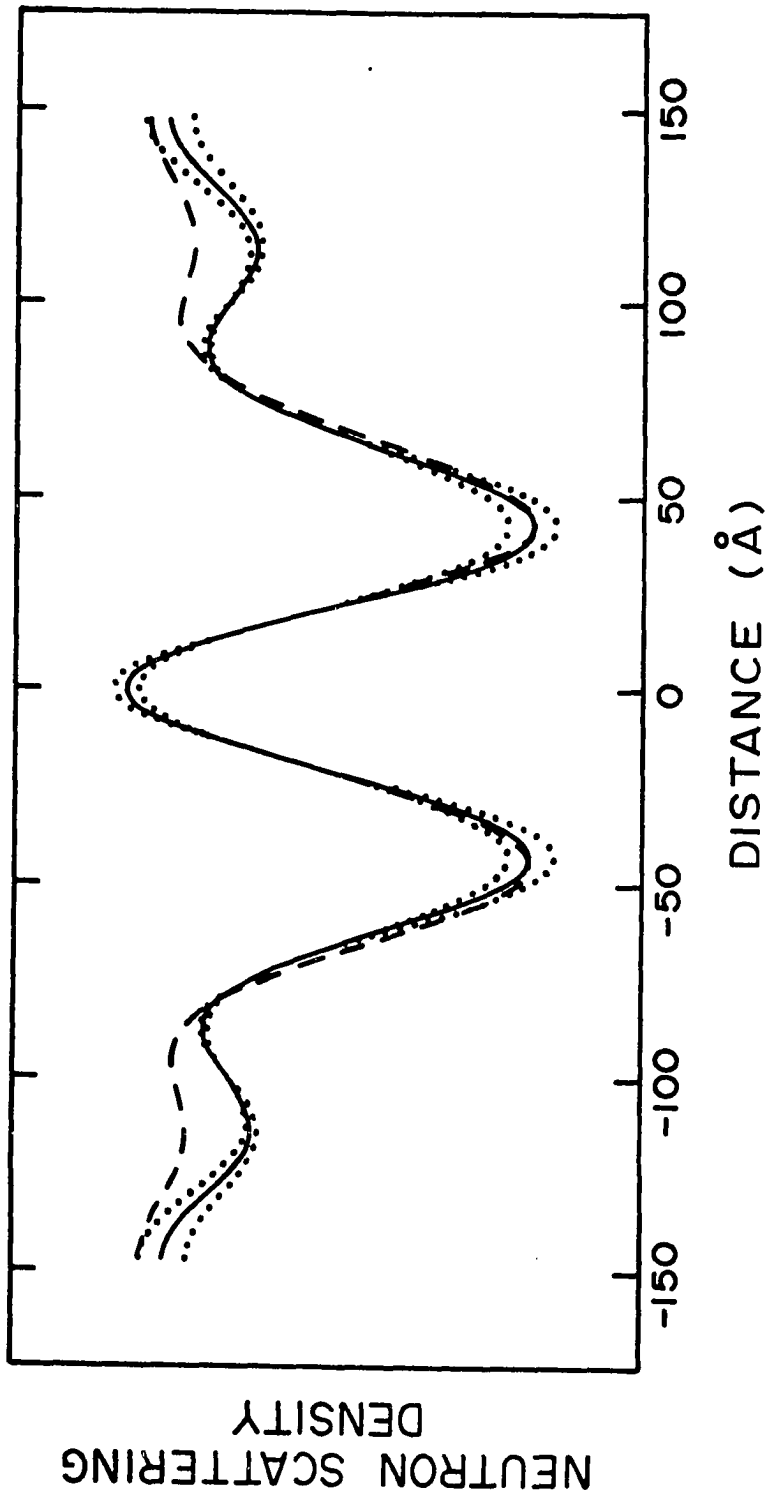

region calculated from the contrast-match point is based on different assumptions for the chemical composition of the disc membrane.

CHAPTER VII

CONCLUSIONS

Neutron diffraction experiments on intact retinas confirm by an independent approach the x-ray diffraction studies which suggest that the lipid bilayer is a major structural motif of the rod outer segment disc membrane. Neutron Fourier syntheses in different mixtures of D_2O and H_2O indicate that the intradisc and extradisc spaces are predominantly aqueous, consistent with the increase in the intradisc and extradisc volumes as the Ringer's solution is made more hypotonic. In isotonic Ringer's solution the thicknesses of the intradisc and extradisc spaces are about 36 Å and 160 Å, respectively, and the center-to-center separation between the 50 Å thick lipid bilayers is 88 Å.

Assuming that the intradisc space is occupied by pure Ringer's solution, the contrast-match point for the hydrocarbon region of the disc membrane is $0.45 \pm 0.20 \times 10^{-14}$ cm/Å^3, corresponding to $14.6 \pm 2.8\%$ D_2O. If the hydrocarbon region is occupied exclusively by anhydrous protein and hydrocarbon, then the volume fraction of protein in the hydrocarbon region is 0.23 ± 0.10. If all non-rhodopsin protein resides in the hydrocarbon region, then the proportion of rhodopsin residing in the hydrocarbon region is $35 \pm 25\%$. If all non-rhodopsin resides outside the hydrocarbon region, then the proportion of rhodopsin residing in the hydrocarbon region is $54 \pm 25\%$.

Neutron scattering density profiles in D_2O Ringer's solution are strikingly asymmetric with a lower scattering density on the extradisc side of the disc membrane compared with the intradisc space. Models that orient rhodopsin asymmetrically on the cytoplasmic face of the disc membrane extending into the extradisc aqueous space are in close agreement with the observed asymmetry. However, rhodopsin cannot entirely account for the observed asymmetry, suggesting that other hydrogenated material resides in the extradisc region. From the neutron scattering density level of 5×10^{-14} cm/Å^3 for the extradisc region, the concentration of extradisc solids is estimated to be between 7×10^4 and 1.6×10^5 daltons per 38,000 daltons rhodopsin, depending on the chemical components residing in the extradisc space. The existence of such material may account for the stabilization of the regular, parallel arrangements of discs in the rod outer segment.

CHAPTER VIII

PROSPECTS

Experiments on intact retinas have demonstrated the power of the neutron diffraction method to obtain structural information about biological membranes. Considering the technical difficulties, it is pleasing that neutron Fourier syntheses at 75 Å resolution have provided at least as much information about the architecture of the disc membrane as x-ray Fourier syntheses at 30 Å resolution. This is a result of the enhanced contrast in the structure with neutron radiation and of the ability to obtain different images of the structure by varying the D_2O/H_2O ratio.

Future efforts will be directed at obtaining higher resolution data over the entire range of D_2O concentration. Neutron diffraction experiments using the two-dimensional position sensitive detector (Alberi, et al., 1975) are quite promising. In D_2O Ringer's solution, the diffraction pattern extends to 33 Å resolution (Figure 10d), and the first 6 orders of diffraction can be obtained in only 5 minutes (Figure 37). Thus, it should be possible to obtain diffraction from a single specimen in H_2O and D_2O. At least four structural issues are amenable to investigation by neutron diffraction of retinal photoreceptor membranes. (1) The structural changes that occur upon bleaching can be assessed by comparing diffraction from a specimen in

Figure 37. Neutron diffraction pattern of two bleached retinas obtained with a two-dimensional position-sensitive detector, showing 6 reflections (50Å resolution) after only 5 min of data collection. The spectrum displays the intensity distribution across the horizontal axis of the counter after integration of the intensities around the vertical position of the incident beam.

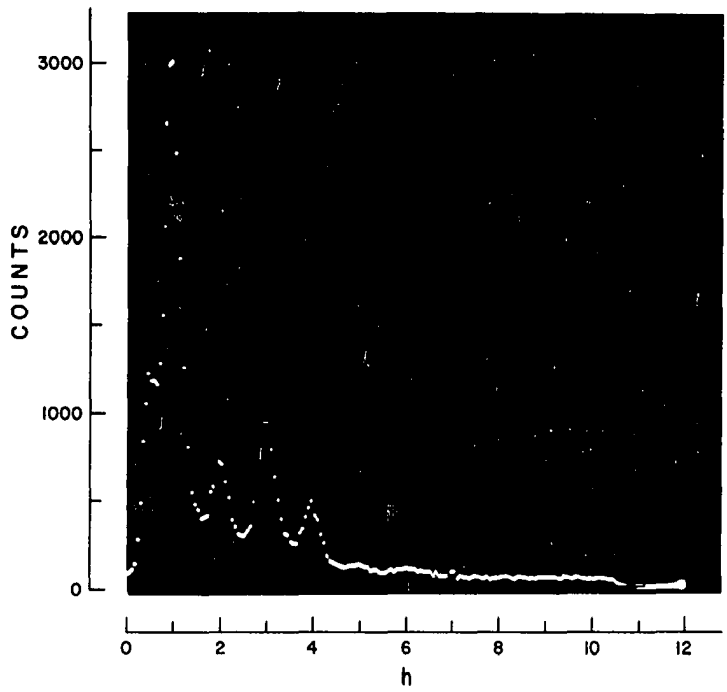

the dark and light. It may also be possible to examine the structures of spectrally-identified intermediates in the photolysis of rhodopsin. (2) Higher resolution neutron Fourier syntheses may reveal whether rhodopsin is a transmembrane protein. (3) The 11-cis retinal chromophore can be located in the unit cell by difference Patterson analysis of diffraction from retinas with and without a deuterated chromophore. (4) It may be possible to locate sites of Ca^{++} accumulation in the unit cell since the scattering length of Ca^{44} (0.13×10^{-12}cm) is much less than the scattering length of Ca^{40} (0.49×10^{-12}cm).

Such studies should provide further insight into the molecular basis of visual excitation and the molecular structure of biological membranes and membrane proteins.

REFERENCES

Alberi, J., Fischer, J., Radeka, V., Rogers, L. C., and Schoenborn, B., A Two-Dimensional Position-Sensitive Detector for Thermal Neutrons, Nucl. Instrum. Methods, 127: 507 (1975).

Arndt, U. W. and Willis, B. T. M., Single Crystal Diffractometry, Cambridge: Cambridge Univ. Press (1966).

Arnott, S., The Geometry of Diffraction of Crystalline Fibers, Polymer 6: 478 (1965).

Bacon, G. E., Neutron Diffraction, London: Oxford Univ. Press (1962).

Barrett, A. N., Barrington Leigh, J., Holmes, K. C., Leberman, R., Mandelkow, E., von Sengbusch, P., and Klug, A., An Electron-Density Map of Tobacco Mosaic Virus at 10Å Resolution, Cold Spring Harbor Symp. Quant. Biol., 36: 433 (1971).

Bear, R. S. and Bolduan, O. E. A., Diffraction by Cylindrical Bodies with Periodic Axial Structure, Acta Cryst., 3: 236 (1950).

Bevington, P. R., Data Reduction and Error Analysis for the Physical Sciences, New York: McGraw-Hill Book Co. (1969).

Blasie, J. K., The Location of Photopigment Molecules in the Cross-Section of Frog Retinal Receptor Disk Membranes, Biophys. J., 12: 191 (1972).

Blasie, J. K., Dewey, M. M., Blaurock, A. E. and Worthington, C. R., Electron Microscope and Low-angle X-ray Diffraction Studies on Outer Segment Membranes from the Retina of the Frog,

J. Mol. Biol., 14: 143 (1965).

Blasie, J. K. and Worthington, C. R., Planar Liquid-like Arrangement of Photopigment Molecules in Frog Retinal Receptor Disk Membranes, J. Mol. Biol., 39: 417 (1969).

Blasie, J. K., Worthington, C. R., and Dewey, M. M., Molecular Localization of Frog Retinal Receptor Photopigment by Electron Microscopy and Low-angle X-ray Diffraction, J. Mol. Biol., 39: 407 (1969).

Blaurock, A. E., Structure of the Retinal Membrane Containing the Visual Pigments, Adv. Exp. Med. Biol., 24: 53 (1972).

Blaurock, A. E. and Wilkins, M. H. F., Structure of Frog Photoreceptor Membranes, Nature, 223: 906 (1969).

Blaurock, A. E. and Wilkins, M. H. F., Structure of Retinal Photoreceptor Membranes, Nature, 236: 313 (1972).

Blessing, R. H., Coppens, P., and Becker, P., Computer Analysis of Step-Scanned X-ray Data, J. Appl. Cryst., 7: 488 (1972).

Bolduan, O. E. A. and Bear, R. S., Unidirectional Nature of the Large Periodic Structure of Collagen Fibrils, J. Polymer Sci., 5: 159 (1950).

Bolduan, O. E. A. and Bear, R. S., General Nature of the Extension of Structure Transverse to Collagen Fibril Axes, J. Polymer Sci., 6: 271 (1951).

Bownds, D. and Brodie, A. E., Light-Sensitive Swelling of Isolated Frog Rod Outer Segments as an In Vitro Assay for Visual Transduction and Dark Adaptation, J. Gen. Physiol., 66: 407 (1975).

Bragg, W. L. and Perutz, M. F., The External Form of the Haemoglobin Molecule. I, Acta Cryst., 5: 277 (1952).

Brierley, G. P., Fleischman, D., Hughes, S. D., Hunter, G. R., and McConnell, D. G., On the permeability of isolated bovine retinal outer segment fragments, Biochim. Biophys. Acta, 163: 117 (1968).

Buerger, M. J., Crystal-structure Analysis, New York: John Wiley and Sons, Inc. (1960).

Cain, J. E., Lattice Disorder and Substitution Disorder in Oriented Membrane Systems: The Structure of the Chromatophore Membrane Determined by X-ray Diffraction, Thesis: U. of Pennsylvania, Philadelphia (1974).

Caspar, D. L. D. and Kirschner, D. A., Myelin Membrane Structure at 10Å Resolution, Nature New Biol., 231: 46 (1971).

Caspar, D. L. D. and Phillips, W. C., Dynamical Effects in Small-Angle Neutron Diffraction from Membranes, 1975 Brook. Symp. Biol., 27: VII-107 (1976).

Cella, R. J., Lee, B., and Hughes, R. E., Lorentz and Orientation Factors in Fiber X-ray Diffraction Analysis, Acta Cryst., A26: 118 (1970).

Chabre, M., X-ray Diffraction Studies of Retinal Rods I. Structure of the Disc Membrane, Effect of Illumination, Biochim. Biophys. Acta, 382: 322 (1975).

Chabre, M. and Cavaggioni, A., Light Induced Changes of Ionic Flux in the Retinal Rod, Nature New Biol., 244: 118 (1973).

Chabre, M. and Cavaggioni, A., X-ray Diffraction Studies of Retinal Rods II. Light Effect on the Osmotic Properties, Biochim. Biophys. Acta, 382: 336 (1975).

Chabre, M., Saibil, H., and Worcester, D. L., Neutron Diffraction Studies of Oriented Retinal Rods, 1975 Brook. Symp. Biol., 27: III-77(1976).

Clark, A. W. and Branton, D., Fracture Faces in Frozen Outer Segments from the Guinea Pig Retina, Z. Zelloforsch., 91: 586 (1968).

Cohen, A. I., Electron Microscope Observations on Form Changes in Photoreceptor Outer Segments and their Saccules in Response to Osmotic Stress, J. Cell Biol., 48: 547 (1971).

Cohn, E. J. and Edsall, J. T., Apparent Molal Volume, Heat Capacity, Compressibility and Surface Tension of Dipolar Ions in Solutions, Proteins, Amino Acids And Peptides As Ions And Dipolar Ions, New York: Reinhold Publishing Corp., Chapter 7: 155 (1943).

Corless, J. M., Lamellar Structure of Bleached and Unbleached Rod Photoreceptor Membranes, Nature, 237: 229 (1972).

Corless, J. M., Cobbs, W. H., Costello, M. J., and Robertson, J. D., On the Asymmetry of Frog Retinal Rod Outer Segment Disk Membranes, Exp. Eye Res., 23: 295 (1976).

Daemen, F. J. M., Vertebrate Rod Outer Segment Membranes, Biochim. Biophys. Acta, 300: 255 (1973).

Daemen, F. J. M., DeGrip, W. J., and Jansen, P. A. A., Biochemical Aspects of the Visual Process XX. The Molecular Weight of Rhodopsin, Biochim. Biophys. Acta, 271: 419 (1972).

Deas, H. D., The Diffraction of X-rays by a Random Assemblage of Molecules Having Partial Alignment, Acta Cryst., 5: 542 (1952).

Demel, R. A., Geurts Van Kessel, W. S. M., and Van Deenen, L. L. M., The Properties of Polyunsaturated Lecithins in Monolayers and Liposomes and the Interactions of These Lecithins with

Cholesterol, Biochim. Biophys. Acta, 266: 26 (1972).

Denton, E. J., A method of easily observing the dichroism of the visual rods, J. Physiol., 124: 16P (1954).

DeRobertis, E. and Lasansky, A., Ultrastructure and Chemical Organization of Photoreceptors, The Structure of the Eye (ed. by Smelser, G. K.), New York: Academic Press, 29 (1961).

Diamond, R., Profile Analysis in Single Crystal Diffractometry, Acta Cryst., A25: 43 (1969).

Dowling, J. E., The Organization of Vertebrate Visual Receptors, Molecular Organization and Biological Function (ed. by Allen, J. M.) New York: Harper and Row, Chapter 7: 186 (1967).

Downer, N. W. and Englander, S. W., Molecular structure of membrane-bound rhodopsin, Nature, 254: 625 (1975).

Engelman, D. M., Lipid Bilayer Structure in the Membrane of Mycoplasma laidlawii, J. Mol. Biol., 58: 153 (1971).

Ford, G. C., Intensity Determination by Profile Fitting Applied to Precession Photographs, J. Appl. Cryst., 7: 555 (1974).

Franklin, R. E. and Gosling, R. G., The Structure of Sodium Thymonucleate Fibres. II. The Cylindrically Symmetrical Patterson Function, Acta Cryst., 6: 678 (1953).

Gibbs, E. L., An Effective Treatment for Red-Leg Disease in Rana Pipiens, Lab. Animal Care, 13: 781 (1963).

Gras, W. J. and Worthington, C. R., X-ray Analysis of Retinal Photoreceptors, Proc. Nat. Acad. Sci. USA, 63: 233 (1969).

Hagins, W. A., The Visual Process: Excitatory Mechanisms in the Primary Receptor Cells, Ann. Rev. Biophys. Bioeng., 1: 131 (1972).

Harrison, S. C., Structure of Tomato Bushy Stunt Virus I. The Spherically Averaged Electron Density, J. Mol. Biol., 42: 457 (1969).

Hecht, S., Shlaer, S., Pirenne, M. H., Energy, Quanta, and Vision, J. Gen. Physiol., 25: 819 (1942).

Heitzmann, H., Rhodopsin is the Predominant Protein of Rod Outer Segment Membranes, Nature New Biol., 235: 114 (1972).

Heller, J., Ostwald, T. J., and Bok, D., The Osmotic Behavior of Rod Photoreceptor Outer Segment Discs, J. Cell Biol., 48: 633 (1971).

Holmes, K. C. and Barrington Leigh, J., The Effect of Disorientation on the Intensity Distribution of Non-crystalline Fibres. I. Theory, Acta Cryst., A30: 635 (1974).

Holmes, K. C., Stubbs, G. J., Mandelkow, E., and Gallwitz, U., Structure of tobacco mosaic virus at 6.7Å resolution, Nature, 254: 192 (1975).

Hosemann, R. and Bagchi, S. N., Direct Analysis of Diffraction by Matter, Amsterdam: North Holland Publishing Co. (1962).

Huxley, H. E. and Brown, W., The Low-angle X-ray Diagram of Vertebrate Striated Muscle and its Behavior during Contraction and Rigor, J. Mol. Biol., 30: 383 (1967).

James, R. W., The Optical Principles of the Diffraction of X-rays, Ithaca: Cornell Univ. Press (1965).

Johnson, S. M., Bangham, A. D., Hill, M. W., and Korn, E. D., Single bilayer liposomes, Biochim. Biophys. Acta, 233: 820 (1971).

Kirschner, D. A., The Structure of the Nerve Myelin Membrane at 10Å Resolution, Thesis: Harvard Univ., Cambridge (1971).

Kirschner, D. A., Comparative X-ray and Neutron Diffraction from Nerve Myelin Membranes, Spectroscopy in Biology and Chemistry

Neutron, X-ray, Laser, New York: Academic Press, Inc., Chapter 6: 203 (1974).

Kirschner, D. A. and Caspar, D. L. D., Comparative Diffraction Studies on Myelin Membranes, Ann. N. Y. Acad. Sci., 195: 309 (1972).

Kirschner, D. A., Caspar, D. L. D., Schoenborn, B. P., and Nunes, A. C., Neutron Diffraction Studies of Nerve Myelin, 1975 Brook. Symp. Biol., 27: III-68 (1976).

Korenbrot, J. I., Brown, D. T., and Cone, R. A., Membrane Characteristics and Osmotic Behavior of Isolated Rod Outer Segments, J. Cell Biol., 56: 389 (1973).

Krieger, M., Chambers, J. L., Christoph, G. G., Stroud, R. M., and Trus, B. L., Data Collection in Protein Crystallography: Capillary Effects and Background Corrections, Acta Cryst., A30: 740 (1974).

Langridge, R., Wilson, H. R., Hooper, C. W., Wilkins, M. H. F., and Hamilton, L. D., The Molecular Configuration of Deoxyribonucleic Acid I. X-ray Diffraction Study of a Crystalline Form of the Lithium Salt, J. Mol. Biol., 2: 19 (1960).

Lehmann, M. S., The Estimated Standard Deviation of a Step-Scan-Measured Bragg Reflexion Intensity, J. Appl. Cryst., 8: 619 (1975).

Lehmann, M. S. and Larsen, F. K., A Method for Location of the Peaks in Step-Scan-Measured Bragg Reflexions, Acta Cryst., A30: 580 (1974).

Levine, Y. K., X-ray Diffraction Studies of Membranes, Prog. Surf. Sci., 3: 279 (1973).

Lewis, M. S., Krieg, L. C., and Kirk, W. D., The Molecular Weight

and Detergent Binding of Bovine Rhodopsin, Exp. Eye Res., 18: 29 (1974).

Liebman, P. A., Birefringence, Dichroism and Rod Outer Segment Structure, Photoreceptor Optics (ed. by A. W. Snyder and R. Menzel), Section B: 199 (1975).

Liebman, P. A., Jagger, W. S., Kaplan, M. W., and Bargoot, F. G., Membrane structure changes in rod outer segments associated with rhodopsin bleaching, Nature, 251: 31 (1974).

Luzzati, V., X-ray Diffraction Studies of Lipid-Water Systems, Biological Membranes (ed. by D. Chapman), New York: Academic Press, Chapter 3: 71 (1968).

Moore, P. B., A Short Introduction to Resolution Errors in Solution Scattering Data, 1975 Brook. Symp. Biol., 27: VII-67 (1976).

Moore, P. B., Engelman, D. M., and Schoenborn, B. P., Asymmetry in the 50S Ribosomal Subunit of Escherichia coli, Proc. Nat. Acad. Sci. USA, 71: 172 (1974).

Nace, G. W., Culley, D. D., Emmons, M. B., Gibbs, E. L., Hutchison, V. H. and McKinney, R. G., Guidelines for the Breeding, Care, and Management of Laboratory Animals; Amphibians, Washington: National Academy of Sciences - National Research Council (1974).

Nilsson, S. E. G., The Ultrastructure of the Receptor Outer Segments in the Retina of the Leopard Frog (Rana pipiens), J. Ultrastruc. Res., 12: 207 (1965).

Nunes, A. C., A Simple Neutron Diffractometer for Low Angle Biological Studies, Nucl. Instrum. Methods, 108: 189 (1973).

Papermaster, D. S. and Dreyer, W. J., Rhodopsin Content in the Outer Segment Membranes of Bovine and Frog Retinal Rods, Biochem., 13:

2438 (1974).

Pober, J. S., Iwanij, V., Reich, E., and Stryer, L., Enzyme-Catalyzed Insertion of a Fluorescent Probe into the Proteolytically-Sensitive Region of Rhodopsin, Biophys. J., 21: 36a (1976).

Pober, J. S. and Stryer, L., Light Dissociates Enzymatically-cleaved Rhodopsin into Two Different Fragments, J. Mol. Biol., 95: 477 (1975).

Robinson, W. E., Gordon-Walker, A., and Bownds, D., Molecular Weight of Frog Rhodopsin, Nature New Biol., 235: 112 (1972).

Saari, J. C., The Accessibility of Bovine Rhodopsin in Photoreceptor Membranes, J. Cell Biol., 63: 480 (1974).

Saibil, H., Chabre, M., and Worcester, D., Neutron diffraction studies of retinal rod outer segment membranes, Nature, 262: 266 (1976).

Santillan, G. and Blasie, J. K., Comparison of the Electron Density Profile for Isolated, Water-Washed Photoreceptor Disk Membranes with the Profile for Disk Membranes in the Intact Retina, Biophys. J., 16: 35a (1976).

Saxena, A. M. and Schoenborn, B. P., Correction Factors for Neutron Diffraction from Lamellar Structures, Acta Cryst., in press.

Schoenborn, B. P., Neutron Diffraction Analysis of Myoglobin, Nature. 224: 143 (1969).

Schmatz, W., Springer, T., Schelten, J. and Ibel, K., Neutron Small-Angle Scattering: Experimental Tecnhiques and Applications, J. Appl. Cryst., 7: 96 (1974).

Schoenborn, B. P., Neutron Scattering for the Analysis of Membranes, Biochim. Biophys. Acta, 457: 41 (1976).

Schoenborn, B. P. and Nunes, A. C., Neutron Scattering, Ann. Rev. Biophys. Bioeng., 1: 529 (1972).

Schwartz, S., Cain, J. E., Dratz, E. A., and Blasie, J. K., An Analysis of Lamellar X-ray Diffraction from Disordered Membrane Multilayers with Application to Data from Retinal Rod Outer Segments, Biophys. J., 15: 1201 (1975).

Sidman, R. L., The Structure and Concentration of Solids in Photoreceptor Cells Studied by Refractometry and Interference Microscopy, J. Biophys. Biochem. Cyt., 3: 15 (1957).

Soller, W., A New Precision X-ray Spectrometer, Phys. Rev., 24: 158 (1924).

Steinemann, A. and Stryer, L., Accessibility of the Carbohydrate Moiety of Rhodopsin, Biochemistry, 12: 1499 (1973).

Stubbs, G. J., The Effect of Disorientation on the Intensity Distribution of Non-crystalline Fibres. II. Applications, Acta Cryst., A30: 639 (1974).

Tomita, T., Electrical Activity of Vertebrate Photoreceptors, Quart. Rev. Biophys., 3: 179 (1970).

Trayhurn, P., Mandel, P. and Virmaux, N., Composition of the Rhodopsin-core Obtained by Proteolysis of Retinal Rod Outer Segments with Papain, and its Regenerability after Photobleaching, Exp. Eye Res., 19: 259 (1974a).

Trayhurn, P., Mandel, P., and Virmaux, N., Removal of a Large Fragment of Rhodopsin without Changes in its Spectral Properties by Proteolysis of Retinal Rod Outer Segments, FEBS Lett., 38: 351 (1974b).

Traube, J., Ueber den Raum der Atome, Samml. Chem. u. Chem. Tech. Vort., 4: 255 (1899).

Vainshtein, B. K., Diffraction of X-rays by Chain Molecules, Amsterdam: Elsevier Publishing Co. (1966).

Van Breugel, P. J. G. M., Daemen, F. J. M., and Bonting, S. L., Biochemical Aspects of the Visual Process, XXIX. Effect of Pronase on Rod Outer Segment Membranes and Rhodopsin, Exp. Eye Res., 21: 315 (1975).

Vanderkooi, G. and Sundaralingam, M., Biological Membrane Structure, II. A Detailed Model for the Retinal Rod Outer Segment Membrane, Proc. Nat. Acad. Sci. USA, 67: 233 (1970).

Wald, G., Molecular Basis of Visual Excitation, Science, 162: 230 (1968).

Warren, B. E., X-ray Diffraction, Reading: Addison-Wesley Publishing Co. (1969).

Webb, N. G., X-ray Diffraction Studies of Retinal Rod Outer Segments and Related Membranes, Thesis: King's College, London (1972).

Wilkins, M. H. F., X-ray Studies of Membranes and Model Systems, Ann. N. Y. Acad. Sci., 195: 291 (1972).

Woolfson, M. M., An Introduction to X-ray Crystallography, Cambridge: Cambridge Univ. Press (1970).

Worcester, D. L., Neutron Diffraction Studies of Biological Membranes and Membrane Components, 1975 Brook. Symp. Biol., 27: III-37 (1976).

Worcester, D. L. and Franks, N. P., Structural Analysis of Hydrated Egg Lecithin and Cholesterol Bilayers II. Neutron Diffraction, J. Mol. Biol., 100: 359 (1976).

Worthington, C. R., X-ray Analysis of Retinal Photoreceptor Structure, Exp. Eye Res., 17: 487 (1973).

Worthington, C. R., Structure of Photoreceptor Membranes, Ann. Rev. Biophys. Bioeng., 3: 53 (1974).

Worthington, C. R. and McIntosh, T. J., Direct Determination of the Lamellar Structure of Peripheral Nerve Myelin at Moderate Resolution (7Å), Biophys. J., 14: 703 (1974).

Yariv, J., Kalb, A. J., and Giberman, E., A Saccharide Ligand on the Outer Surface of Retinal Rod Disc Membranes, J. Mol. Biol., 85: 183 (1974).

Yeager, M. J., Neutron Diffraction Analysis of the Structure of Retinal Photoreceptor Membranes and Rhodopsin, 1975 Brook. Symp. Biol., 27: III-3 (1976a).

Yeager, M. J., Data Analysis of Low-Angle Diffraction by One-Dimensional Crystals, 1975 Brook. Symp. Biol., 27: VII-77 (1976b).

Yeager, M., Schoenborn, B., Engelman, D., Moore, P., and Stryer, L., Neutron Diffraction of Retinal Photoreceptor Membranes, Fed. Proc., 33: 1575 (1974).

Zaccai, G., Blasie, J. K., and Schoenborn, B. P., Neutron Diffraction Studies on the Location of Water in Lecithin Bilayer Model Membranes, Proc. Nat. Acad. Sci. USA, 72: 376 (1975).